Electron dynamics induced by single and multiphoton processes in atoms and molecules

Felipe Zapata Abellán

To cite this version:

Felipe Zapata Abellán. Electron dynamics induced by single and multiphoton processes in atoms and molecules. Atomic Physics [physics.atom-ph]. Sorbonne Université, 2019. English. NNT : 2019SORUS431 . tel-03001291v2

HAL Id: tel-03001291
https://theses.hal.science/tel-03001291v2

Submitted on 12 Nov 2020

THÈSE DE DOCTORAT DE SORBONNE UNIVERSITÉ

Spécialité :

Chimie théorique

présentée par

M. Felipe ZAPATA ABELLÁN

pour obtenir le grade de

DOCTEUR DE SORBONNE UNIVERSITÉ

Sujet de la thèse :

Electron dynamics induced by single and multiphoton processes in atoms and molecules

Soutenue le 26 septembre 2019 devant le jury composé de :

Prof.	**Katarzyna PERNAL**	Politechnika Łódzka	Rapporteure
Prof.	**Mauro STENER**	Università di Trieste	Rapporteur
Dr.	**Emanuele COCCIA**	Università di Trieste	Examinateur
Prof.	**Phuong Mai DINH**	Université Paul Sabatier	Examinatrice
Prof.	**Fernando MARTÍN**	Universidad Autónoma de Madrid	Examinateur
Prof.	**Rodolphe VUILLEUMIER**	École Normale Supérieure	Présidente du Jury
Dr.	**Eleonora LUPPI**	Sorbonne Université	Directrice de thèse
Dr.	**Julien TOULOUSE**	Sorbonne Université	Co-encadrant

“L’approximation c’est l’objectivation inachevée,
mais c’est l’objectivation prudente, féconde, vraiment rationnelle
puisqu’elle est à la fois consciente de son insuffisance et de son progrès.”

Essais sur la connaissance approchée.
Gaston BACHELARD (1884-1964)

Abstract

The present PhD thesis contributes to the development of numerical methods used to reproduce the electron dynamics induced by single and multiphoton processes in atoms and molecules. In the perturbative regime, photoexcitation and photoionization have been studied in atoms with range-separated density-functional theory, in order to take into account the electron-electron interaction effects. Moreover, in the non-perturbative regime, above-threshold ionization and high-harmonic generation spectra have been simulated using different representations for the time-dependent wave function for the purpose of describing the continuum states of the irradiated system. Our studies open the possibility of exploring matter-radiation processes in more complex systems.

Résumé

Cette thèse contribue aux développements de méthodes numériques utilisées pour reproduire la dynamique électronique induite par des processus à un et plusieurs photons dans les atomes et molécules. Dans le domaine perturbatif, la photoexcitation et la photoionisation ont été étudiées à l'aide de la théorie de la fonctionnelle de la densité à séparation de portée, dans le but de prendre en compte les effets d'interaction électron-électron. De plus, dans le domaine non-perturbatif, les spectres au-delà du seuil d'ionisation et les spectres de génération d'harmoniques d'ordres élevés ont été simulés en utilisant différentes représentations de la fonction d'onde dépendante du temps du système étudié. Cette étude ouvre la possibilité d'explorer des processus matière-rayonnement dans des systèmes plus complexes.

Contents

ABSTRACT/RÉSUMÉ i

1 INTRODUCTION 1

2 ELECTRON DYNAMICS INDUCED BY A LASER FIELD 3

2.1 Matter-radiation interaction . . . 3

2.1.1 Classical description of an electromagnetic field . . . 3

2.1.2 Time-dependent Schrödinger equation . . . 5

2.1.2.1 TDSE in the velocity gauge . . . 6

2.1.2.2 TDSE in the length gauge . . . 7

2.2 First-order time-dependent perturbation theory . . . 8

2.2.1 Single-photon transition rate . . . 10

2.2.2 Cross sections and oscillator strengths . . . 11

2.3 Multiphoton ionization processes . . . 12

2.3.1 Photoelectron spectrum . . . 12

2.3.2 Photoemission spectrum . . . 14

3 METHODS FOR ELECTRONIC-STRUCTURE CALCULATIONS 15

3.1 The B-spline representation . . . 16

3.1.1 Piecewise polynomial functions and the subspace $\mathbb{P}_{k,\xi,\nu}$ . . . 17

3.1.2 Definition of the B-splines . . . 18

3.1.3 The basis set of B-splines as a basis of $\mathbb{P}_{k,\xi,\nu}$ . . . 21

3.2 One-electron atoms . . . 23

3.2.1 Solving the Schrödinger equation in the subspace $\mathbb{P}_{k,\xi,\nu}$ . . . 26

3.2.2 Eigenvalues and eigenfunctions . . . 30

3.2.3 B-spline parameters and numerical accuracy . . . 34

3.2.4 Continuum states . . . 34

3.2.4.1 Energy spectrum . . . 37

3.2.4.2 Density of states 38
3.2.4.3 Normalization of the continuum wave functions 39
3.3 Solving the time-dependent Schrödinger equation 41
3.3.1 Time discretization 42
3.3.2 Computation of the B-spline matrix elements 43
3.4 N-electron atoms 45
3.4.1 Two-electron integrals for the Coulomb interaction 47
3.4.1.1 Qiu and Froese Fischer Integration-Cell Algorithm . . . 49
3.4.1.2 Some $F^k[p,q]$ and $G^k[p,q]$ integrals 51
3.4.2 Long-range and short-range two-electron integrals 52
3.4.2.1 Exact expression for the short-range interaction 54
3.4.2.2 Power series expansion of the short-range interaction . . 56
3.5 Molecules 59
3.5.1 Gaussian-type orbitals 61
3.5.2 Time-dependent configuration interaction singles theory 62
3.5.3 Exploring the accuracy of the GTO basis 64
3.5.3.1 Potential energy curves 65
3.5.3.2 Energy spectrum 66
3.5.3.3 Ghost atoms effects on high-harmonic generation . . . 68

4 RANGE-SEPARATED DFT FOR ATOMIC SPECTRA 71
4.1 Introduction 71
4.2 Range-separated density-functional theory 74
4.2.1 Range-separated hybrid scheme 74
4.2.2 Linear-response time-dependent range-separated hybrid 76
4.3 Implementation in a B-spline basis set 78
4.3.1 Coulomb two-electron integrals 79
4.3.2 Long-range and short-range two-electron integrals 80
4.4 Results and discussion 82
4.4.1 Density of continuum states 82
4.4.2 Range-separated orbital energies 83
4.4.3 Photoexcitation/photoionization in the hydrogen atom 86
4.4.4 Photoexcitation/photoionization in the helium atom 90
4.5 Conclusions 92

5 OPTIMAL BASIS SET FOR STRONG LASER FIELDS 93
- 5.1 Introduction . . . 93
- 5.2 1D theoretical model of H_2^+ . . . 96
  - 5.2.1 HHG and ATI spectra . . . 97
  - 5.2.2 Representation of the time-dependent wave function . . . 98
    - 5.2.2.1 Real-space grid . . . 98
    - 5.2.2.2 B-spline basis set . . . 99
    - 5.2.2.3 Gaussian basis set . . . 99
- 5.3 1D results and discussion . . . 101
  - 5.3.1 Spectrum of the field-free Hamiltonian . . . 101
  - 5.3.2 HHG . . . 104
  - 5.3.3 ATI . . . 110
- 5.4 3D theoretical model of H_2^+ . . . 112
  - 5.4.1 Representation of the time-dependent wave function . . . 114
    - 5.4.1.1 Real-space grid . . . 114
    - 5.4.1.2 Gaussian basis set . . . 114
- 5.5 3D results and discussion . . . 114
  - 5.5.1 HHG . . . 115
- 5.6 Conclusions . . . 115

6 CONCLUSION 119

APPENDICES 121

A THE WIGNER 3-J SYMBOL 121

B SPHERICAL HARMONICS 123
- B.1 Legendre polynomials $P_l(x)$ . . . 123
- B.2 Associated Legendre polynomials $P_l^m(x)$ . . . 124
- B.3 Spherical harmonics $Y_l^m(\Omega)$ . . . 125

C GAUSS-LEGENDRE QUADRATURE 129

REFERENCES 131

CHAPTER 1

Introduction

Spectroscopy is an ancient branch of physical chemistry. It collects a large variety of techniques to explore the nature of substances throughout the study of matter-radiation interactions. In this context, the electromagnetic spectrum of light is a fundamental support which encodes, for example, important information from the chemical composition of distant galaxies or from the electronic structure of tiny atoms. The present PhD thesis is about the computation of single and multiphoton processes in atoms and molecules induced by a laser field. Concretely, our attention has been focused on the development of different methods that enable us to reproduce the electron dynamics induced by photons.

From a theoretical point of view, the study of the interaction between an atom (or a molecule) and an electromagnetic field requires two essential ingredients: (1) the calculation of the electronic structure of the irradiated system and (2) the description of the electromagnetic interaction. The electronic structure can be predicted using numerical techniques based on the representation of the N-electron wave function in a Hilbert space. On the other side, the electromagnetic interaction is described with the laser field parameters, i.e. the intensity, the energy of the photons, etc.

Having these two ingredients in mind, during the last three years, we have developed, implemented, and used different computational methods in order to compute atomic and molecular spectra generated by single and multiphoton processes.

Nowadays, a clear understanding of these processes is still a challenge. For this reason, new theoretical approximations and new computational methods shall be developed. The present PhD thesis shows our contributions to this theoretical and computational development. This manuscript is organized as follows. Chapter 2 is focused on the calculation of the target observables that characterize single and multiphoton processes. Chapter 3 shows in details the numerical methods we used in our work to calculate electronic structures in atoms and molecules. In Section 3.1, we present the B-splines. In Section 3.2, we comment the calculation of one-electron atoms with B-splines. Section 3.3 is about the solution of the time-dependent Schrödinger equation for one-electron atoms using the technique of B-splines, and Section 3.4 is dedicated to the calculation of the two-electron integrals (also with

B-splines) required to explore N-electron atoms. Finally, in Section 3.5 attention is focused on the computation of molecular electronic structures using Gaussian-type orbitals. Moreover, the time-dependent configuration interaction singles method is briefly presented.

In Chapter 4, we present our investigation on photoexcitation and photoionization in atoms, where we implemented a linear-response range-separated density-functional theory method, and in Chapter 5 attention is focused on our study of the optimal representation of the time-dependent wave function for strong laser fields. At the end of the manuscript, general conclusions and perspectives are given.

CHAPTER 2

Electron dynamics induced by a laser field

This chapter contains a brief overview on matter-radiation interaction. First, we present first-order perturbation theory, used in the calculation of single-photon spectra. Second, multiphoton ionization processes are commented. The computation of above-threshold ionization (ATI) and high-harmonic generation (HHG) spectra is introduced. We note that in this chapter attention has been focused on interactions produced by a linearly polarized laser[1] field.

2.1 MATTER-RADIATION INTERACTION

This section has been realized following the book of G. C. Schatz and M. A. Ratner *"Quantum Mechanics in Chemistry"* [Schatz 03]. Additionally, our presentation of first-order perturbation theory has been completed using as a reference the book *"Mécanique Quantique II"*, written by C. Cohen-Tannoudji, B. Diu and F. Laloë [Cohen-Tannoudji 97].

2.1.1 Classical description of an electromagnetic field

Maxwell's equations design the classical framework in which an electromagnetic field is described. Both electric $\mathcal{E}(\mathbf{r},t)$ and magnetic $\mathcal{B}(\mathbf{r},t)$ fields are generated by the scalar potential $\Phi(\mathbf{r},t)$ and the vector potential $\mathbf{A}(\mathbf{r},t)$ as follows (in IS units)

$$\mathcal{E}(\mathbf{r},t) = -\nabla\Phi(\mathbf{r},t) - \frac{\partial \mathbf{A}(\mathbf{r},t)}{\partial t}, \tag{2.1}$$

$$\mathcal{B}(\mathbf{r},t) = \nabla \times \mathbf{A}(\mathbf{r},t), \tag{2.2}$$

The potentials $\Phi(\mathbf{r},t)$ and $\mathbf{A}(\mathbf{r},t)$ are not uniquely defined and depend on the choice of the gauge. However, the fields $\mathcal{E}(\mathbf{r},t)$ and $\mathcal{B}(\mathbf{r},t)$ are invariant under the following gauge transformation

$$\Phi(\mathbf{r},t) \rightarrow \Phi'(\mathbf{r},t) = \Phi(\mathbf{r},t) - \frac{\partial f(\mathbf{r},t)}{\partial t}, \tag{2.3}$$

$$\mathbf{A}(\mathbf{r},t) \rightarrow \mathbf{A}'(\mathbf{r},t) = \mathbf{A}(\mathbf{r},t) + \nabla f(\mathbf{r},t), \tag{2.4}$$

---

[1] From *"light amplification by stimulated emission of radiation"*.

where $f(\mathbf{r},t)$ is a scalar function. In the Coulomb gauge, also called the radiation gauge, is defined by imposing

$$\nabla \cdot \mathbf{A}(\mathbf{r},t) \quad = \quad 0. \tag{2.5}$$

As a consequence, one has

$$\nabla^2 \Phi(\mathbf{r},t) \quad = \quad 4\pi\varrho, \tag{2.6}$$

where ϱ is the charge density. In the case of no sources of charge, the scalar potential vanishes in the Coulomb gauge. Within these conditions, it can be shown that a monochromatic linearly polarized electromagnetic plane wave is generated by the potential vector

$$\mathbf{A}(\mathbf{r},t) = A_0\ \hat{\mathbf{e}}\ \cos(\mathbf{k}\cdot\mathbf{r} - \omega t), \tag{2.7}$$

and described by the corresponding fields

$$\begin{aligned} \mathcal{E}(\mathbf{r},t) &= -\frac{\partial \mathbf{A}(\mathbf{r},t)}{\partial t} = \mathcal{E}_0\ \hat{\mathbf{e}}\ \sin(\mathbf{k}\cdot\mathbf{r} - \omega t), & (2.8) \\ \mathcal{B}(\mathbf{r},t) &= \nabla \times \mathbf{A}(\mathbf{r},t) = \mathcal{B}_0\ (\hat{\mathbf{e}} \times \hat{\mathbf{k}})\ \sin(\mathbf{k}\cdot\mathbf{r} - \omega t), & (2.9) \end{aligned}$$

where the electric field strength is given by $\mathcal{E}_0 = -\omega A_0$ and the magnetic strength by $\mathcal{B}_0 = -A_0\ |\mathbf{k}|$, where A_0 is the amplitude of the vector potential and $\omega = |\mathbf{k}|c$ is the angular frequency of the plane wave, with c is the speed of light. Moreover, ω corresponds to a frequency $\nu = \omega/2\pi$ and to a wavelength $\lambda = c/\nu$. Finally, $\mathbf{k}$ is the propagation vector orthogonal to the polarization unitary vector $\hat{\mathbf{e}}$, i.e. $\mathbf{k}\cdot\hat{\mathbf{e}} = 0$. In addition, the intensity $I(\omega)$ of the radiation can be calculated using the Poynting vector, which represents the instantaneous energy flux, as follows

$$\mathcal{S}(\mathbf{r},t) = \mathcal{E}(\mathbf{r},t) \times \mathcal{B}(\mathbf{r},t) = A_0^2\ |\mathbf{k}|^2\ c\ \hat{\mathbf{k}} \sin(\mathbf{k}\cdot\mathbf{r} - \omega_\lambda t)^2. \tag{2.10}$$

Over a whole wave period, $T = 2\pi/\omega$, the intensity can be expressed as

$$I(\omega) = \frac{1}{T}\int_0^T |\mathcal{S}(\mathbf{r},t)| \mathrm{d}t = \frac{A_0^2\ |\mathbf{k}|^2\ c}{2} = \frac{A_0^2\ \omega^2}{2\ c} = \frac{\mathcal{E}_0^2}{2\ c}. \tag{2.11}$$

The total number of photons $\mathcal{N}(\omega)$ of angular frequency ω, within a volume V, can be obtained from the following relation

$$\mathcal{N}(\omega) = \frac{I(\omega)}{\hbar\omega}\frac{V}{c}. \tag{2.12}$$

In typical working conditions, i.e. $I(\omega) \simeq 10^{14}$ W cm^{-2}, when using a monochromatic linearly polarized radiation, generated by a Ti:Sapphire laser with photon energy $\hbar\omega = 1.55$ eV, the total number of photons in the volume $V = \lambda^3$, with $\lambda = 2\pi c/\omega = 800$ nm, is $\mathcal{N}(\omega) \simeq 1 \times 10^8$, which is a very large quantity. Therefore, a classical description of the electromagnetic field can be justified, see for instance [Mandel 95].

2.1.2 Time-dependent Schrödinger equation

The semi-classical non-relativistic Hamiltonian for a N-electron atom in an electromagnetic field is described by

$$\hat{H}(t) = \sum_{i=1}^{N} \frac{1}{2m_e}\left[\hat{\mathbf{p}}_i + e\mathbf{A}(\mathbf{r}_i, t)\right]^2 + V(\mathbf{r}_1 ... \mathbf{r}_N) - \sum_{i=1}^{N} e\Phi(\mathbf{r}_i, t), \tag{2.13}$$

where the spin-dependent terms have been neglected. The electron momentum operator is defined as $\hat{\mathbf{p}}_i = -i\hbar\nabla_{\mathbf{r}_i}$ and the potential $V(\mathbf{r}_1 ... \mathbf{r}_N)$ takes into account the electron interactions of the system, i.e. electron-nucleus and electron-electron interactions. In the Coulomb gauge, Eq. (2.13) is rewritten as

$$\hat{H}(t) = \hat{H}_0 + \hat{H}_{\text{int}}(t), \tag{2.14}$$

where the field-free Hamiltonian $\hat{H}_0$ is given by

$$\hat{H}_0 = \sum_{i=1}^{N} \frac{\hat{\mathbf{p}}_i^2}{2m_e} + V(\mathbf{r}_1 ... \mathbf{r}_N), \tag{2.15}$$

and the time-dependent interaction Hamiltonian $\hat{H}_{\text{int}}(t)$ by

$$\hat{H}_{\text{int}}(t) = \sum_{i=1}^{N} \frac{e}{m_e}\mathbf{A}(\mathbf{r}_i, t) \cdot \hat{\mathbf{p}}_i + \sum_{i=1}^{N} \frac{e^2}{2m_e}\mathbf{A}(\mathbf{r}_i, t)^2. \tag{2.16}$$

At this point, it is very interesting to see that, if the wavelength λ of the radiation is larger than the size of the atomic system, and the intensity is not very high, the spatial variations of the field across the atomic system can be neglected. As a consequence, the vector potential becomes spatially homogeneous, i.e. $\mathbf{A}(\mathbf{r}_i, t) \approx \mathbf{A}(t)$. This important approximation is called the *dipole approximation* and translates Eq. (2.16) into

$$\hat{H}_{\text{int}}(t) = \frac{e}{m_e}\mathbf{A}(t) \cdot \mathbf{P} + \frac{e^2 N}{2m_e}\mathbf{A}^2(t), \tag{2.17}$$

where $\mathbf{P} = \sum_{i=1}^{N} \hat{\mathbf{p}}_i$ is the total electron momentum operator. Finally, within the former conditions and approximations, one can write the non-relativistic spin-free time-dependent Schrödinger equation (TDSE) for a N-electron atom in an electromagnetic field as

$$i\hbar\frac{\partial}{\partial t}\Psi(t) = \left[\hat{H}_0 + \frac{e}{m_e}\mathbf{A}(t) \cdot \mathbf{P} + \frac{e^2 N}{2m_e}\mathbf{A}^2(t)\right]\Psi(t), \tag{2.18}$$

where $\Psi(t)$ is the time-dependent N-electron wave function. In general, it can be shown that Eq. (2.18) is invariant under certain gauge transformations

$$\Psi(t) \quad \rightarrow \quad \Psi'(t) = \Psi(t) \times \exp\left\{-\frac{ie}{\hbar}f(t)\right\}, \tag{2.19}$$

together with Eq. (2.4) and Eq. (2.3), where now the scalar function f only depends on time. Consequently, it is very interesting to see that simple forms of Eq. (2.18) can be obtained by choosing the appropriate gauge. Let us now briefly introduce the *velocity* and the *length gauges* of the TDSE.

2.1.2.1 TDSE in the velocity gauge

Within the dipole approximation, the diamagnetic quadratic interaction term, appearing in Eq. (2.18), can be eliminated by choosing the velocity gauge. Basically, this gauge translates Eq. (2.18) into the following form

$$i\hbar\frac{\partial}{\partial t}\Psi^V(t) = \left[\hat{H}_0 + \frac{e}{m_e}\mathbf{A}(t) \cdot \mathbf{P}\right]\Psi^V(t), \tag{2.20}$$

where one has used the scalar function

$$f^V(t) = -\frac{eN}{2m_e}\int_{-\infty}^{t} \mathbf{A}^2(t')\mathrm{d}t', \tag{2.21}$$

together with the potentials

$$\mathbf{A}^V(t) = \mathbf{A}(t), \tag{2.22}$$

$$\Phi^V(t) = \frac{eN}{2m_e}\mathbf{A}^2(t). \tag{2.23}$$

In the velocity gauge, the time-dependent interaction Hamiltonian is defined by

$$\hat{H}^V_{\text{int}}(t) = \frac{e}{m_e}\mathbf{A}(t)\cdot\mathbf{P}. \tag{2.24}$$

If a monochromatic plane wave is used, the potential vector may be express as

$$\mathbf{A}(t) = A_0\,\hat{\mathbf{e}}\,\cos(\omega_\lambda t). \tag{2.25}$$

Moreover, with this kind of radiation, Eq. (2.24) can be rewritten as

$$\hat{H}^V_{\text{int}}(t) = \hat{H}^V_{\text{int}}\,e^{-i\omega_\lambda t} + \left(\hat{H}^V_{\text{int}}\right)^*\,e^{i\omega_\lambda t}, \tag{2.26}$$

with $\hat{H}^V_{\text{int}} = (eA_0/2m_e)\hat{\mathbf{e}}\cdot\mathbf{P}$.

2.1.2.2 TDSE in the length gauge

Another common form of Eq. (2.18) is presented by the length gauge, which can be expressed as

$$i\hbar\frac{\partial}{\partial t}\Psi^L(t) = \left[\hat{H}_0 + e\,\mathcal{E}(t)\cdot\mathbf{R}\right]\Psi^L(t), \tag{2.27}$$

where $\mathbf{R} = \sum_{i=1}^{N}\mathbf{r}_i$ is the total position operator, and $\mathcal{E}(t)$ the electric field in the dipole approximation. In order to obtain Eq. (2.27), one uses the following scalar function

$$f^L(t) = -\mathbf{A}(t)\cdot\mathbf{R}, \tag{2.28}$$

together with the potentials

$$\mathbf{A}^L(t) = 0, \tag{2.29}$$

$$\Phi^L(t) = -\mathcal{E}(t)\cdot\mathbf{R}. \tag{2.30}$$

The time-dependent interaction Hamiltonian in the length gauge is then given by

$$\hat{H}^L_{\text{int}}(t) = e\,\mathcal{E}(t)\cdot\mathbf{R}. \tag{2.31}$$

If a monochromatic radiation is used, the electric field in the dipole approximation can be defined as

$$\mathcal{E}(t) = \mathcal{E}_0\,\hat{\mathbf{e}}\,\cos(\omega_\lambda t). \tag{2.32}$$

Then, Eq. (2.31) is rewritten as

$$\hat{H}^L_{\text{int}}(t) = \hat{H}^L_{\text{int}}\,e^{-i\omega_\lambda t} + \left(\hat{H}^L_{\text{int}}\right)^*\,e^{i\omega_\lambda t}, \tag{2.33}$$

with $\hat{H}^L_{\text{int}} = (e\mathcal{E}_0/2)\hat{\mathbf{e}}\cdot\mathbf{R}$.

2.2 FIRST-ORDER TIME-DEPENDENT PERTURBATION THEORY

Once the TDSE has be rewritten in a simple form, using the velocity or the length gauges, one can start to think about its resolution. However, in most of the cases, this is not an easy task. In fact, the TDSE encodes the *"quantum many-body problem"* which cannot be solved exactly in systems with more that two particles. As a consequence, under different assumptions, diverse approximations can be performed.

In our case, it has been described that, as long as the intensity of the radiation is small, solutions of the TDSE can be expanded in a *perturbation series* [Cohen-Tannoudji 97]. For this reason, if one works with low laser intensities, single-photon processes can be accurately described within time-dependent perturbation theory (TDPT). In this framework, the time-dependent Hamiltonian of the investigated electronic system is given by

$$\hat{H}(t) = \hat{H}_0 + \lambda_{\text{int}}\hat{V}(t), \tag{2.34}$$

where $\hat{H}_0$ is the field-free Hamiltonian of the system, $\hat{V}(t)$ is the time-dependent perturbation and λ_{int} is a parameter that controls the strength of the perturbation. As well as this, TDPT assumes that the time-dependent wave function $\Psi(t)$ can be decomposed onto the eigenstates of $\hat{H}_0$ as

$$\Psi(t) = \sum_{m=1}^{\infty} c_m(t)\,\psi_m\,e^{-i\frac{\varepsilon_m}{\hbar}t}, \tag{2.35}$$

where the expansion coefficients $\{c_m(t)\}$ take into account the temporal dependence and the couples $\{\varepsilon_m, \psi_m\}$ are solutions of the following eigenvalue problem

$$\hat{H}_0\psi_m = \varepsilon_m\psi_m. \tag{2.36}$$

If Eq. (2.35) is now substituted into the TDSE, an ensemble of coupled differential equations can be obtained,

$$i\hbar\frac{\mathrm{d}}{\mathrm{d}t}c_m(t) = \lambda_{\text{int}}\sum_{k=1}^{\infty} V_{m,k}(t)\; c_k(t)\; e^{i\omega_{m,k}t}, \tag{2.37}$$

where the time-dependent perturbation matrix elements are defined as

$$V_{m,k}(t) = \langle\psi_m|\hat{V}(t)|\psi_k\rangle, \tag{2.38}$$

and $\omega_{m,k} = (\varepsilon_m - \varepsilon_k)/\hbar$. In order to solve Eq. (2.37), TDPT proposes to approximate the time-dependent coefficients to a perturbative series as

$$c_m(t) = \sum_{n=0}^{\infty}\lambda_{\text{int}}^n\; c_m^{(n)}(t). \tag{2.39}$$

Then, Eq. (2.37) can be solved for a given specific order n, starting form the definition of the 0th-order (unperturbed) solution, which is

$$c_m^{(0)}(t) = \langle\psi_m|\psi_i\rangle = \delta_{m,i}. \tag{2.40}$$

In fact, this definition indicates that the system is initially found at ψ_i, i.e. $\Psi(t = 0) \equiv \psi_i$, being ψ_i an eigenstate of $\hat{H}_0$. Also, one can see that the 0th-order coefficient is a time-independent coefficient, i.e $c_m^{(0)}(t) \equiv c_m^{(0)}$. Subsequently, it can be shown that the first-order solution of Eq. (2.37) is given by the integral

$$c_m^{(1)}(t) = \frac{1}{i\hbar}\int_0^t V_{m,i}(t')\; e^{i\omega_{m,i}t'}\; \mathrm{d}t'. \tag{2.41}$$

2.2.1 Single-photon transition rate

Assuming that the time-dependent wave function Eq. (2.35) is normalized,

$$\langle \Psi(t)|\Psi(t)\rangle = \sum_{m=1}^{\infty} |c_m(t)|^2 = 1, \tag{2.42}$$

the time-dependent coefficient $|c_m(t)|^2$ can be interpreted as the probability that the system has to be in the state ψ_m at time t. As a matter of fact, the first-order transition probability $\mathcal{P}^{(1)}_{i,f}(t)$ is given by the square root of the final state time-dependent coefficient $|c_f(t)|^2$, expressed as

$$\mathcal{P}^{(1)}_{i,f}(t) = |c^{(0)}_f + \lambda_{\text{int}} c^{(1)}_f(t)|^2, \tag{2.43}$$

where $c^{(0)}_f$ is given by $\delta_{i,f} = 0$, and then, the transition probability is completely described by the first-order coefficient of the final state as

$$\mathcal{P}^{(1)}_{i,f}(t) = \lambda^2_{\text{int}} |c^{(1)}_f(t)|^2 = \frac{\lambda^2_{\text{int}}}{\hbar^2} \left| \int_0^t V_{f,i}(t')\, e^{i\omega_{f,i}t'}\, \mathrm{d}t' \right|^2 . \tag{2.44}$$

If now a monochromatic linearly polarized radiation is used, in order to produce the single-photon transition $|\psi_i\rangle \rightarrow |\psi_f\rangle$, one can show that Eq. (2.44) can be rewritten as

$$\mathcal{P}^{(1)}_{i,f}(t) = \frac{\mathcal{E}_0^2 e^2}{4\hbar^2}\, |\langle \psi_i\, |\hat{\mathbf{e}} \cdot \mathbf{R}|\, \psi_f\rangle|^2 \times \left| \int_0^t \left[e^{i(\omega_{if}-\omega)t'} + e^{i(w_{if}+\omega)t'} \right] \mathrm{d}t' \right|^2 , \tag{2.45}$$

where the length-gauge description of the time-dependent perturbation has been used, see for instance Eq. (2.33). Moreover, for large times t, one observes that, if only absorption is taking into account, Eq. (2.45) approximates the following expression

$$\mathcal{P}^{(1)}_{i,f}(t) \approx \frac{\pi \mathcal{E}_0^2 e^2}{2\hbar^2}\, |\langle \psi_i\, |\hat{\mathbf{e}} \cdot \mathbf{R}|\, \psi_f\rangle|^2\, t\, \delta(\omega - \omega_{if}), \tag{2.46}$$

where $\delta(\omega - \omega_{if})$ is the Dirac delta function, which preserves the energy conservation principle in the long time limit. Additionally, the first-order transition rate per unit of time $\Gamma^{(1)}_{i,f}(\omega)$ can be defined as

$$\Gamma^{(1)}_{i,f}(\omega) = \frac{\mathcal{P}^{(1)}_{i,f}(t)}{t} = \frac{\pi \mathcal{E}_0^2 e^2}{2\hbar^2}\, |\langle \psi_i\, |\hat{\mathbf{e}} \cdot \mathbf{R}|\, \psi_f\rangle|^2\, \delta(\omega - \omega_{if}). \tag{2.47}$$

On the other hand, if the final state $|\psi_f\rangle$ is found to be in the continuous region of the spectrum, the initial state $|\psi_i\rangle$ is coupled with an ensemble of continuum states located over an infinitesimal range of energy around the final state energy ε_f. As a consequence, the transition rate per unit of time, between a bound state and a continuum state, is given by *Fermi's golden rule*, such as

$$\tilde{\Gamma}^{(1)}_{i,f}(\omega) = \frac{\tilde{\mathcal{P}}^{(1)}_{i,f}(t)}{t} = \frac{\pi \mathcal{E}_0^2 e^2}{2\hbar^2} \left|\langle \psi_i \left| \hat{\mathbf{e}} \cdot \mathbf{R} \right| \psi_f \rangle\right|^2 \tilde{\rho}(\varepsilon_f) \delta(\omega - \omega_{if}). \tag{2.48}$$

where $\tilde{\rho}(\varepsilon_f)$ is the density of final states. As we are going to show later, the definition of $\tilde{\rho}(\varepsilon_f)$ depends on the chosen continuum state normalization criteria. For this reason, the normalization and the density of continuum states shall be chosen and defined consistently [Friedrich 98].

2.2.2 Cross sections and oscillator strengths

The energy transfer per unit of time, from a monochromatic linearly polarized plane wave radiation to a N-electron atom, is given by the absorption cross section $\sigma_{if}(\omega)$, which is defined as

$$\sigma_{i,f}(\omega) = \frac{\Gamma_{i,f}(\omega)}{I(\omega)} \hbar\omega, \tag{2.49}$$

where the radiation intensity $I(\omega)$ is given by Eq. (2.11), and the transition rate by Eq. (2.47) or Eq. (2.48).

In addition to the cross section, single-photon transitions can be characterized using the dimensionless oscillator strengths $f_{i,f}$, which are expressed as

$$f_{i,f} = \frac{m_e\, c}{2\, \pi\, \hbar\, e^2}\, \sigma_{i,f}. \tag{2.50}$$

In fact, Eq. (4.21) represents the renormalized cross section with respect to the classical harmonic oscillator model [Cohen-Tannoudji 97]. We note that, in atomic units, the oscillator strengths can be expressed within the length or the velocity gauges as

$$f_{i,f} = 2\, \omega_{if} \left|\langle \psi_i \left| \hat{\mathbf{e}} \cdot \mathbf{R} \right| \psi_f \rangle\right|^2 = \frac{2}{\omega_{if}} \left|\langle \psi_i \left| \hat{\mathbf{e}} \cdot \mathbf{P} \right| \psi_f \rangle\right|^2. \tag{2.51}$$

Finally, it can be shown that Eq. (2.51) satisfies the Thomas-Reiche-Kuhn summation $\sum_f f_{i,f} = N$, where N is the number of electrons and the sum runs over all final states.

2.3 MULTIPHOTON IONIZATION PROCESSES

Multiphoton ionization processes were first observed by E. K. Damon and R. G. Tomlinson in 1963 [Damon 63], but Albert Einstein was the first who mentioned the possibility of such processes in 1905 [Einstein 05].

The basic idea, behind these processes, is that several photons can be implicated in absorption or emission at the same time. Multiphoton ionization occurs when an ensemble of photons are absorbed by the system to ionize electrons from bound states to the continuum. These processes can be written as $A + n\, \hbar\omega \rightarrow A^{+} + \ e^{-}$, where n is the number of photons. In 1979, Agostini *et al.* [Agostini 79] showed that, at sufficiently high laser intensities, typically over 10^{13} W/cm^2, the ejected electron e^{-} can absorb photons in excess from the minimum number required for producing the ionization. This phenomenon was called *"above-threshold ionization"* (ATI), and was detected by analyzing photoelectron spectra [Joachain 11].

In the last decades, multiphoton ionization processes have been studied using a classical or a semi-classical picture [Plaja 13]. Within this point of view, electrons can be extracted from the vicinity of the perturbed atom or molecule and taken into the free space, accelerated by the electromagnetic field. However, due to the field oscillations in time, some electrons can go back and re-collide to their core. In these collisions, there is a possibility of recombination and relaxation to one of the bound states. This relaxation of the system is translated into the emission of radiation of different frequencies. This process is named as *"high-harmonic generation"*, and was first modeled by the semi-classical *"three-step model"* [Lewenstein 94].

As one observes, the required intensities for producing these processes are far from the perturbative regime. As a consequence, the TDSE must be solved explicitly with the help of numerical methods. After solving the TDSE, one has access to the time-dependent wave function $\Psi(t)$, which encodes the electron dynamics of the system. In this section, attention is focused on the computation of ATI and HHG spectra once $\Psi(t)$ is known.

2.3.1 Photoelectron spectrum

Photoelectron spectra contain the electron energy (and also angular) distribution after the interaction with the laser pulse. There are different techniques that allow us to compute a photoelectron spectrum [Bachau 01, Mosert 16], but in our work we have implemented the window operator method [Schafer 91], which is based on the spectral analysis of the final state wave function Ψ_f, that is, after the interaction with the laser field. The window operator is defined as

$$\hat{W}(\varepsilon, n, \gamma) = \frac{\gamma^{2^n}}{\left(\hat{H}_0 - \varepsilon\right)^{2^n} + \gamma^{2^n}} \tag{2.52}$$

where n is an integer. This operator acts like a window centered at the energy ε with a width of 2γ. Then, the probability of finding an electron in the energy interval $[\varepsilon - \gamma,\ \varepsilon + \gamma]$ is given by

$$P(\varepsilon, n, \gamma) = \left\langle \Psi_f \middle| \hat{W} \middle| \Psi_f \right\rangle . \tag{2.53}$$

The numerical evaluation of Eq. (2.53) can be performed as follows

$$P(\varepsilon, n, \gamma) = \gamma^{2^n} \left\langle \chi^{(n)} | \chi^{(n)} \right\rangle \tag{2.54}$$

where the vector $\left|\chi^{(n)}\right\rangle$ is defined as

$$\left|\chi^{(n)}\right\rangle = \frac{1}{\left(\hat{H}_0 - \varepsilon\right)^{2^{n-1}} + i\,\gamma^{2^{n-1}}} \left|\Psi_f\right\rangle . \tag{2.55}$$

In order to obtain $\left|\chi^{(n)}\right\rangle$, one shall solve the following equation

$$\left[\left(\hat{H}_0 - \varepsilon\right)^{2^{n-1}} + i\,\gamma^{2^{n-1}}\right] \left|\chi^{(n)}\right\rangle = \left|\Psi_f\right\rangle . \tag{2.56}$$

In practice, the choice of $n = 2$ gives good results, as shown in Ref. [Schafer 91]. Then, for $n = 2$, Eq. (2.56) can be factorized easily and one obtains

$$\left[\left(\hat{H}_0 - \varepsilon\right) + \sqrt{i}\,\gamma\right] \left[\left(\hat{H}_0 - \varepsilon\right) - \sqrt{i}\,\gamma\right] \left|\chi^{(2)}\right\rangle = \left|\Psi_f\right\rangle, \tag{2.57}$$

and $\left|\chi^{(2)}\right\rangle$ is computed by solving the following system

$$\left[\left(\hat{H}_0 - \varepsilon\right) + \sqrt{i}\,\gamma\right] \quad \left|\xi\right\rangle = \left|\Psi_f\right\rangle, \tag{2.58}$$

$$\left[\left(\hat{H}_0 - \varepsilon\right) - \sqrt{i}\,\gamma\right] \quad \left|\chi^{(2)}\right\rangle = \left|\xi\right\rangle. \tag{2.59}$$

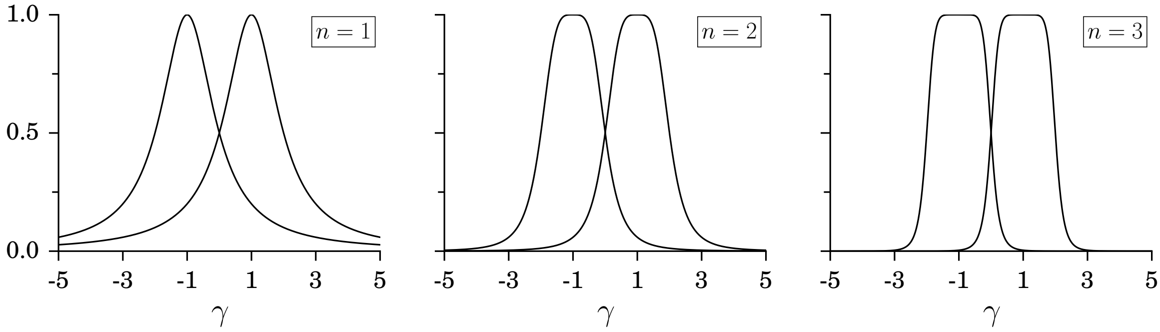

Figure 2.1: Two window functions separated by 2γ for $n=1$, $n=2$ and $n=3$. As we see, for $n=1$ windows correspond to Lorentzians, having a large overlap and a sharp peak.

The two parameters, that a user of the window method must indicate, are γ and n. A small value of γ gives us the possibility of having fine energy resolutions, while a large value of n allows for accurate results. Figure 2.1 presents two successive window functions for different values of n. When n increases, the overlap between functions decreases and the energy bins became rectangular. A simple and useful illustration of the amount of overlap can be obtained by the examination of the sum of all the probabilities $P(\varepsilon, n, \gamma)$ over the whole range of energy. Since the final state wave function is normalized to unity, this quantity must be equal to one. Note that the spacing between successive values of ε is always 2γ.

2.3.2 Photoemission spectrum

Informations on ionization processes can be extracted from the light spectrum generated by the radiating dipole moment. This is computed as the Fourier transform of the time-dependent dipole $d(t) = \langle\Psi(t)|\hat{\xi}|\Psi(t)\rangle$, such as

$$P_{\xi}(\omega) = \left| \frac{1}{t_f - t_i} \int_{t_i}^{t_f} \langle\Psi(t)|\hat{\xi}|\Psi(t)\rangle e^{-i\omega t} \mathrm{d}t \right|^2 , \tag{2.60}$$

where $\hat{\xi}$ can be given by the position operator (denoted here as $\hat{z}$) or by the velocity operator $\hat{v}_z = -i[\hat{z}, \hat{H}(t)]$, or by the acceleration operator $\hat{a}_z = -i[\hat{v}_z, \hat{H}(t)]$, where $\hat{H}(t)$ is the time-dependent Hamiltonian, and t_i and t_f are the initial and final propagation times. The three forms of the power spectrum Eq. (2.60) are then the dipole $P_z(\omega)$, the velocity $P_{v_z}(\omega)$ and the acceleration $P_{a_z}(\omega)$ forms. Those are related to each other as follows,

$$\omega^2 P_z(\omega) \approx P_{v_z}(\omega) \approx \frac{1}{\omega^2} P_{a_z}(\omega), \tag{2.61}$$

see for instance the appendix section in [Coccia 16b].

CHAPTER 3

Methods for electronic-structure calculations

For the purposes of calculating time-independent and time-dependent electronic wave functions, required for the computation of single and multiphoton processes, this chapter is dedicated to the electronic-structure methods that I used during my PhD. First of all, attention is focused on B-splines. During my PhD, I developed from scratch a series of Fortran codes based on such functions. These codes were designed for investigating atomic systems (in spherical polar coordinates) and molecular systems in reduced dimensions (one dimension), see Chapter 4 and Chapter 5. Therefore, in Section 3.1 B-splines are presented. This section has been strongly inspired by the PhD thesis of E. Cormier, entitled *"Étude théorique de l'interaction entre un système à 1 ou 2 électrons actifs et un champ laser intense"* [Cormier 94]. As well as this, I followed the book of C. de Boor *"A Practical Guide to Splines"* [de Boor 78]. From this book I translated the basic Fortran subroutines to evaluate B-splines to build up my own codes. In order to validate the implementation of B-splines, in Section 3.2 we introduce the use of B-splines in one-electron atoms. After that, I carry out different calculations on the hydrogen atom. With these calculations I reproduce the results presented by E. Cormier in his PhD thesis and also some of the results given by Bachau *et al.* in the review *"Applications of B-splines in atomic and molecular physics"* [Bachau 01]. In Section 3.3 we present the numerical resolution of the TDSE in one-electron atoms using B-splines. In Section 3.4, the electronic structure of N-electron atoms is briefly commented. Attention is focused on the computation of the two-electron integrals with B-splines. In our work, only a direct integration method has been developed. To compute these integrals I followed the work of Qiu *et al.* [Qiu 99]. In addition, in this section we present the integration of the long-range and short-range two-electron integrals, implemented in our work presented in Chapter 4. In Section 3.5, some fundamental aspects of molecular electronic-structure calculations are introduced. We briefly present the Gaussian-type orbital functions, implemented in commercial quantum chemistry packages, such as *Molpro* [Werner 15] or *Qchem* [Shao 15]. In particular, these two codes were used during my PhD for the study of molecules.

Finally, in Section 3.5 we comment the time-dependent configuration interaction singles (TDCIS) method, implemented in the code *Light* [Luppi 13] and used in our work presented in Chapter 5.

3.1 THE B-SPLINE REPRESENTATION

In the last decades, thanks to computer power, polynomial interpolation has become a fundamental tool in signal and image processing, numerical analysis or, for example, in disciplines such as social sciences. Polynomials are a common choice used to approximate analytical functions. The reason is, basically, because polynomials can be evaluated, differentiated and integrated easily using the basic arithmetic operations of addition, subtraction, and multiplication. From a computational point of view, these aspects make polynomials great mathematical objects. In addition, experience has shown that, in some specific cases, when the target function oscillates strongly, piecewise polynomial functions of high order are much more efficient than simple polynomials. B-splines are piecewise polynomial functions (L^2-integrable functions defined in a restricted sampled space) which have smooth connections between the pieces, presenting a high level of flexibility that allow us to fit any kind of continuous curve. In fact, the term “spline” makes reference to industrial designers and shipbuilders who, in the past, used to draw continuous and smooth curves over a sequence of “knot points” using a flexible piece of wooden or rubber named spline. Formally, B-spline functions were introduced by I. J. Schoenberg after the Second World War [Schoenberg 46, Schoenberg 64, Schoenberg 73], and thanks to C. de Boor’s monograph [de Boor 78], they were popularized in different branches of applied mathematics, see for example [Unser 99] and references therein.

The early use of B-splines in atomic physics demonstrated their ability to solve scattering and bound-state problems [Shore 73, Fischer 89, Fischer 90, Sapirstein 96, Fischer 08], and today they are recognized as a powerful tool when continuum states are required. The success of such functions is directly related to their effective completeness, that is, the capability to approach L^2 completeness without numerical spoiling [Argenti 09]. Nowadays, atomic program packages based on B-splines are available [Nikolopoulos 03, Nepstad 10, Fischer 11]. However, new algorithms have to be developed in order to increase the computational efficiency of complex calculations, concretely when one works with molecules. For this reason, new hybrid basis sets, which combine B-splines and Gaussian-type orbitals, have been recently developed, see for example [Marante 14, Marante 17].

Let us now introduce the fundamental aspects of the spline interpolation, required in our electronic-structure calculations.

3.1.1 Piecewise polynomial functions and the subspace $\mathbb{P}_{k,\xi,\nu}$

Definition 1 *Let* $\xi := \{\xi_i \in [0, x_{max}]\}_{i=1}^{l+1}$ *be a sequence of breakpoints and* k *a positive integer. If* $P_1(x), ..., P_l(x)$ *is a sequence of* l *polynomials, each of them of order* k *(i.e. degree* $k-1$*), then we define the corresponding piecewise polynomial function* $f(x)$ *of order* k *by the prescription*

$$f(x) := P_i(x) \ \text{ if } \ \xi_i < x < \xi_{i+1} \ \ ; i = 1, ..., l.$$

The set of all such piecewise polynomial functions of order k *with a given sequence* ξ *is denoted by the space* $\mathbb{P}_{k,\xi}$.

The space $\mathbb{P}_{k,\xi}$ is a linear space of dimension kl. A function $f(x)$ in $\mathbb{P}_{k,\xi}$ is composed by l polynomials, one for each interval defined by two breakpoints, and each polynomial presents k components (k coefficients for a polynomial of degree $k-1$). The choice of such space is not restrictive enough because no continuity conditions are imposed at the breakpoints. As we are going to work with atomic wave functions, which must be continuous, one has to add supplementary restrictions to the set of $f(x)$. What we are going to do is to define a subspace of $\mathbb{P}_{k,\xi}$ in which the functions $f(x)$ and its derivatives will be continuous at the breakpoints. This problem is solved in the subspace $\mathbb{P}_{k,\xi,\nu} \subset \mathbb{P}_{k,\xi}$ thanks to the following definition:

Definition 2 *Let* $f(x) \in \mathbb{P}_{k,\xi,\nu}$ *be a piecewise polynomial function of order* k *(i.e. degree* $k-1$*) with the following continuity conditions* $\nu := \{\nu_i\}_1^{l+1}$ *at the breakpoints* $\xi := \{\xi_i\}_1^{l+1}$

$$f(x) \in \mathbb{P}_{k,\xi}$$

$$\frac{\partial^{(j-1)} f}{\partial x^{j-1}} \ \text{ is continuous at } \xi_i \text{ for } j = 1, ..., \nu_i.$$

Some examples:

For $\nu_i = 0$, there is no continuity condition at ξ_i.

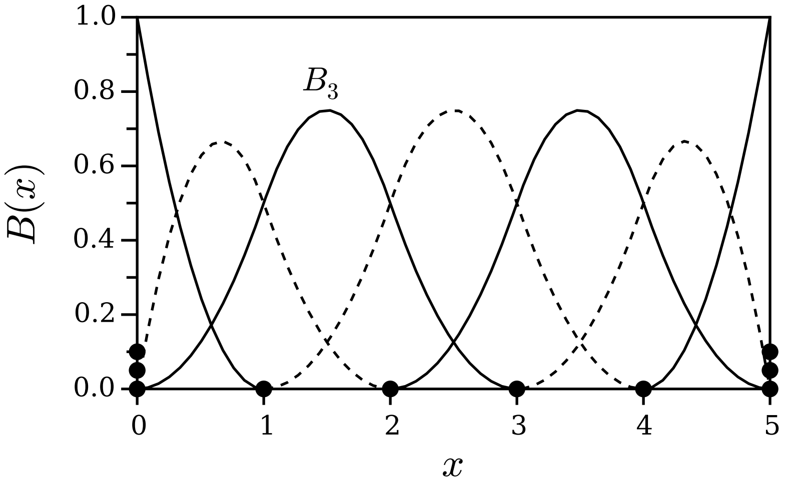

Figure 3.1: A full set of B-splines of order $k = 3$ (i.e. degree 2) associated to the knot sequence $t = \{0, 0, 0, 1, 2, 3, 4, 5, 5, 5\}$. Knots are represented by full circles. Figure inspired from [Bachau 01].

For $\nu_i = 1$, f is continuous at ξ_i.

For $\nu_i = 3$, f, $\partial f/\partial x$ and $\partial^2 f/\partial x^2$ are continuous at ξ_i.

Moreover, the k-th derivative of f is continuous everywhere except at the breakpoints. That is because f is a polynomial function of order k in each interval. The sequence $\nu = \{\nu_i\}_1^{l+1}$ only fixes the continuity conditions at the limits of intervals, that is, at the breakpoints. Usually, one manipulates many functions of $\mathbb{P}_{k,\xi,\nu}$ at the same time. Therefore, it is very useful to properly define a basis from such space. Our goal is to expand any function of $\mathbb{P}_{k,\xi,\nu}$ in terms of a linear combination of functions $g_1, g_2, ... \in \mathbb{P}_{k,\xi,\nu}$ to operate with the decomposition coefficients. We are going to see that each space $\mathbb{P}_{k,\xi,\nu}$ posses its own basis consisting on splines. These *basis splines* are named B-splines.

3.1.2 Definition of the B-splines

Definition 3 *Let $t := \{t_i\}$ be a nondecreasing sequence. The i-th B-spline of order k for the knot sequence t is denoted by $B^k_{i,t}$ and is defined iteratively by the Cox-de Boor recursion relation as*

$$B^1_{i,t}(x) = \begin{cases} 1 & \textit{if } x \in [t_i, t_{i+1}), \\ 0 & \textit{elsewhere}, \end{cases} \tag{3.1}$$

$$B^k_{i,t}(x) = \frac{x - t_i}{t_{i+k-1} - t_i} B^{k-1}_{i,t}(x) + \frac{t_{i+k} - x}{t_{i+k} - t_{i+1}} B^{k-1}_{i+1,t}(x). \tag{3.2}$$

Eq. (3.1) defines the B-spline of order $k = 1$ over the interval $[t_i, t_{i+1})$, while the recurrence relation (Eq. (3.2)) allows us to compute any B-spline as a combination of two B-splines of order $k - 1$, starting with the information given by Eq. (3.1).

Usually, one writes $B_i(x)$ instead of $B^k_{i,t}(x)$ as long as k and t can be inferred from the context. The definition of the knot sequence doesn't exclude the superposition of two or more consecutive knots. As we are going to see, the distribution of knots will control the continuity conditions of B-splines between intervals. Figure 3.1 reports all the B-splines of order 3 associated with the knot sequence $t = \{0, 0, 0, 1, 2, 3, 4, 5, 5, 5\}$. We notice that a single B-spline, for example $B_3(x)$, is defined by its order k over an interval $[t_3, t_{3+k}]$, which contains $k+1$ consecutive knots. From this discrete behavior, some general properties can be deduced:

- **Compact support:** A B-spline has a small support, i.e., $B_i(x) = 0 \quad \forall x \notin [t_i, t_{i+k}]$. It follows that only k B-splines $B_{i-k+1}, B_{i-k+2}, ..., B_\mu$ might be nonzero on the interval $[t_i, t_{i+1}]$. Then, we deduce that for a given x only k B-splines are nonzero:

  $$\left.\begin{array}{ll} B_{j-k+1} & \neq 0 \\ \vdots & \\ B_\mu & \neq 0 \end{array}\right\} \forall x \in [t_i, t_{i+1}].$$

  Finally, it is easy to show that

  $$\langle B_i | B_j \rangle = \int_a^b B_i(x) B_j(x) \mathrm{d}x = 0 \ \text{ for } \ |i - j| \geq k.$$

- **Positive defined:** Any B-spline $B_i(x)$ is positive on its support, i.e., $B_i(x) > 0$ for $x \in [t_i, t_{i+k}]$.

- **Partition of unity:** With the adopted definition, the B-spline sequence consists of nonnegative functions which sum up to unity, i.e.

  $$\sum_i B_i(x) = 1 \ \ \forall x.$$

- **Connection at the knots:** The sequence of knots has an impact on the continuity of B-splines. There is a direct relation between the multiplicity of the knots and the connection class between the intervals. If m_i is the multiplicity

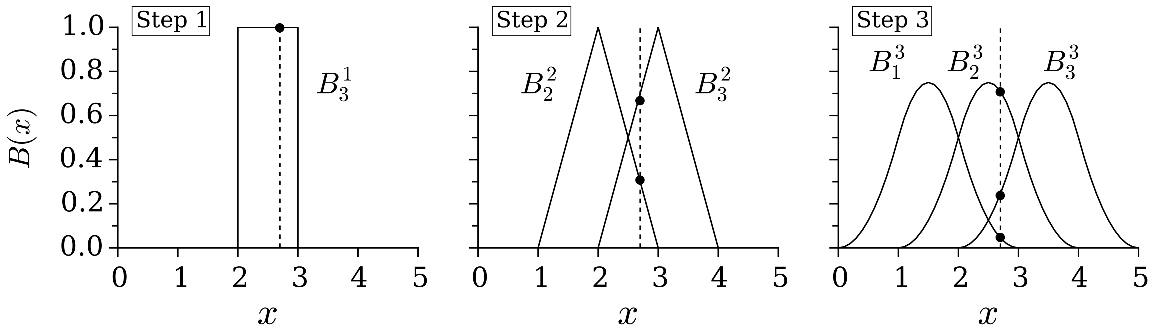

Figure 3.2: Schematic representation of the recursive algorithm used to evaluate the k nonzero B-splines at a given position x, up to order $k = 3$, relative to the knot sequence $t = \{0, 1, 2, 3, 4, 5\}$. Each step is achieved from the previous one by applying the definition formula Eq. (3.2) and starting with the information of the B-spline of order $k = 1$, i.e. Eq. (3.1). Note that at each position x one will obtain k nonzero B-spline values which sum up to unity (black circles). Figure inspired from [Bachau 01].

of a knot $\{t_i = t_{i+1} = ... = t_{i+m_i-1}\}$, then, the connection at the knot is characterized by:

(i) The order of the B-spline k.

(ii) The multiplicity of the knot m_i $(1 \leq m_i \leq k)$.

Moreover, the continuity class[1] is given by C^{k-1-m_i}. Each B-spline is a function composed by different polynomial pieces joined by a certain degree of continuity at each knot. As the knot multiplicity only can takes values from 1 to k, one may find two continuity limits:

- Optimal or maximum continuity limit: $m_i = 1 \Rightarrow C^{k-2}$, the ($k$-2)th derivative is continuous.
- Minimal continuity limit: $m_i = k \Rightarrow C^{-1}$, the B-spline is discontinuous.

- **Numerical evaluation:** Within the given definitions, a direct algorithm can be designed to simultaneously generate the values of the k nonzero B-splines of order k at a given position x. Figure 3.2 presents a scheme of this recursive algorithm introduced by C. de Boor in [de Boor 78]. On the other side, concerning the evaluation of derivatives, one may use Eq. (3.3). This equation is obtained easily from Eq. (3.2), and can be applied successively to compute

---

[1] A function f which is continuous together with its derivatives up to order n, i.e. $f, Df, ..., D^n f$ is labeled by the class C^n. Then, C^0 means that f is continuous and C^{-1} that f is discontinuous.

B-spline derivatives of high order.

$$\frac{\mathrm{d}}{\mathrm{d}x}B^k_{i,t}(x) = (k-1)\left[\frac{B^{k-1}_{i,t}(x)}{t_{i+k-1}-t_i} - \frac{B^{k-1}_{i+1,t}(x)}{t_{i+k}-t_{t_{i+1}}}\right]. \tag{3.3}$$

From a practical point of view, a stable numerical evaluation can be performed using a set of Fortran subroutines designed by C. de Boor. In our work, we have implemented the routine BSPLVP (p. 134 in [de Boor 78]), which requires as input values the order k, the sequence of knots t and the position x. This subroutine evaluates the k nonzero B-splines at x using the algorithm represented in Figure 3.2. In addition, if derivatives are needed, they can be performed using the routine BSPLVD (p. 288 in [de Boor 78]), which is based on Eq. (3.3). Finally, integrals involving B-splines, and its derivatives, can be computed up to machine accuracy employing Gauss-Legendre quadrature, see for instance Appendix C. We recall here that Gauss-Legendre quadrature is exact for a polynomial of order $k = 2M + 1$, where M is the number of Gauss-Legendre points that must be used. Then, for each subinterval in the knot sequence, M evaluation points must be used to compute the polynomial piece integral. After this, one sums up all the M weighted values to obtain the resulting integral in the given subinterval.

3.1.3 The basis set of B-splines as a basis of $\mathbb{P}_{k,\xi,\nu}$

Once B-splines have been defined, we are able to establish the relation between the space $\mathbb{P}_{k,\xi,\nu}$ and the basis of B-splines. To do this, let us formally introduce the notion of spline function:

Definition 4 *A spline function of order k and with knot sequence t is any linear combination of B-splines of order k for the knot sequence t:*

$$f(x) := \sum_i c_i B^k_{i,t}(x). \tag{3.4}$$

The collection of all such spline functions is denoted by $\mathbb{S}_{k,t}$.

In order to build up a sequence of knots and a basis of B-splines from the parameters of the space $\mathbb{P}_{k,\xi,\nu}$, we need to introduce the Curry-Schoenberg theorem:

Theorem 1 *For a strictly increasing sequence* $\xi = \{\xi_i\}_1^{l+1}$*, and a given nonnegative integer sequence* $\nu = \{\nu_i\}_2^l$ *with* $\nu_i \leq k$, $\forall i$ *:*

$$n := k + \sum_{i=2}^{l} (k - \nu_i) = kl - \sum_{i=2}^{l} \nu_i = dim\, \mathbb{P}_{k,\xi,\nu} \tag{3.5}$$

and let $t := \{t_i\}_1^{n+k}$ *be any nondecreasing sequence so that:*

(i) $t_1 \leq t_2 \leq ... \leq t_k \leq \xi_1$ *and* $\xi_{l+1} \leq t_{n+1} \leq ... \leq t_{n+k}$*,*

(ii) for $i = 2, ..., l$*, the number* ξ_i *occurs exactly* $k - \nu_i$ *times in* t*.*

Then, the sequence $\{B_{i,t}^k\}_{i=1}^n$ *of B-splines of order* k *for the knot sequence* t *is a basis for* $\mathbb{P}_{k,\xi,\nu}$ *on the segment* $[t_k, t_{n+1}]$*. So,*

$$\mathbb{P}_{k,\xi,\nu} = \mathbb{S}_{k,t} \;\; on \;\; [t_k, t_{n+1}]. \tag{3.6}$$

The proof of the Curry-Schoenberg theorem is realized in two steps: first, one verifies that each B-spline is in $\mathbb{P}_{k,\xi,\nu}$ as a function on the segment $[t_k, t_{n+1}]$, and second, one shows that the B-splines associated with the knot sequence t are linearly independent. To sum up, the theorem permits the construction of a B-spline basis for any particular piecewise polynomial space $\mathbb{P}_{k,\xi,\nu}$ and gives a recipe to generate an appropriate knot sequence t. Finally, the choice of t translates the continuity conditions (the smoothness of the spline) at a given breakpoint into the corresponding number of knots at that point.

The theorem doesn't limit the choice of the first k and last k knots. A common choice is

$$t_1 = ... = t_k = \xi_1 \;\; \text{and} \;\; t_{n+1} = ... = t_{n+k} = \xi_{l+1},$$

which imposes no continuity conditions at the end points ξ_1 and ξ_{l+1} of the segment of interest. In fact, this choice is consistent with the fact that the B-spline basis provides a valid representation for elements of $\mathbb{P}_{k,\xi,\nu}$ only on the interval $[t_k, t_{n+1}]$. Additionally, this knot distribution confers optimal continuity conditions at the inner points. The construction of such a knot sequence $t = \{t_i\}_1^{n+k}$, from the breakpoint sequence $\xi = \{\xi_i\}_1^{l+1}$ and the sequence $\nu = \{\nu_i\}_1^{l+1}$, can be displayed using the following diagram presented in Table 3.1.

Table 3.1: Translation of breakpoints and continuity conditions into knots of an appropriate multiplicity.

breakpoints	ξ_1	ξ_2	...	ξ_l	ξ_{l+1}
continuity conditions	$\nu_1 = 0$	ν_2	...	ν_l	$\nu_{l+1} = 0$
knot multiplicity	k	$k - \nu_2$	...	$k - \nu_l$	k
knots	$t_1, ..., t_k$	$t_{k+1}, ..., t_{2k-\nu_2}$	...	$t_{(n-1)k-\nu_l+1}, ..., t_n$	$t_{n+1}, ..., t_{n+k}$

Afterwards, thanks to the definition of a basis in terms of B-splines, we are able to manipulate the representation of any spline through its decomposition coefficients. To summarize, this representation, called B-representation, is characterized by the following set of parameters for $f \in \mathbb{P}_{k,\xi,\nu}$:

(i) The integers k and n. That is, the order of f and the number of linear parameters (i.e., $n = kl - \sum_i \nu_i = \dim \mathbb{P}_{k,\xi,\nu}$).

(ii) The vector $t = \{t_i\}_1^{n+k}$ containing the knots (constructed from the sequences ξ and ν).

(iii) The vector $c = \{c_i\}_1^n$ of the coefficients of f with respect to the B-spline basis $\{B_i\}_1^n$.

In terms of these parameters, one has

$$f(x) = \sum_i^n c_i B_i(x) \;\; \forall x \in [t_k, t_{n+1}], \tag{3.7}$$

and in particular, if $t_j \leq x \leq t_{j+1}$ for some $j \in [k, n]$, one has

$$f(x) = \sum_{i=j-k+1}^{j} c_i B_i(x) \;\; \forall x \in [t_j, t_{j+1}], \tag{3.8}$$

where the value of f at x only depends on k coefficients.

3.2 ONE-ELECTRON ATOMS

Also named hydrogen-like atoms (i.e. H, He$^+$, Li^{2+}...), the one-electron atoms are simple dynamical systems composed only by two particles: a nucleus and an electron. The time-independent Schrödinger equation of such a system can be expressed, in

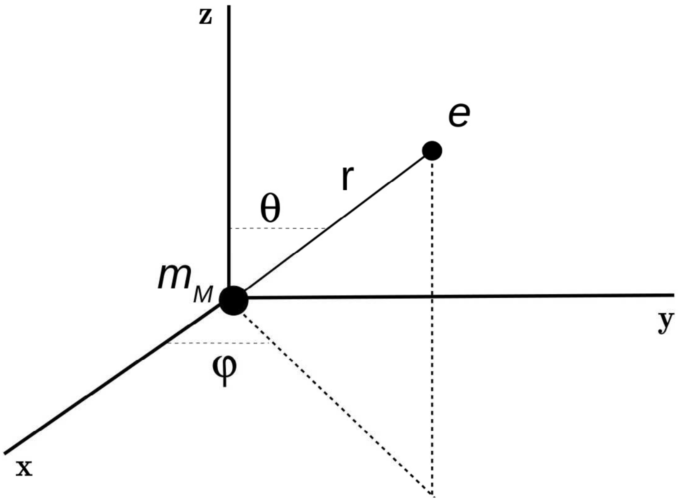

Figure 3.3: Hydrogen-like atom in spherical polar coordinates. The nucleus of mass m_M is placed at the center of the system while the relative position of the electron e is determined by the distance r and the two angles θ and φ.

atomic units, as follows,

$$\left[-\frac{1}{2}\nabla^2 + V(\mathbf{r})\right]\Psi(\mathbf{r}) = \varepsilon\Psi(\mathbf{r}), \tag{3.9}$$

where the first term is the electron kinetic energy operator, $V(\mathbf{r})$ is the nucleus-electron interaction potential and $\Psi(\mathbf{r})$ is the electron stationary state of energy ε. Moreover, different interaction potential models can be used to specify the nucleus-electron interaction $V(\mathbf{r})$. However, a natural choice is to use the Coulomb potential, which in spherical polar coordinates reads as

$$V(\mathbf{r}) = -\frac{Z}{r}, \tag{3.10}$$

where Z is the nuclear charge and r is the distance of the electron to the nucleus, see for instance Figure 3.3. In the case of using a central potential, such as Eq. (3.10), the solutions of Eq. (3.9) can be written as a product of an angular function $Y_l^m(\theta, \varphi)$ and a radial wave function $R_{n,l}(r)$ as follows

$$\Psi_{n,l,m}(\mathbf{r}) = R_{n,l}(r)Y_l^m(\theta, \varphi), \tag{3.11}$$

where $Y_l^m(\theta, \varphi)$ is a spherical harmonic, and the integers n, l and m label the stationary state $\Psi_{n,l,m}(\mathbf{r})$.

Finally, the problem presented in Eq. (3.9) is transformed into a one-dimensional problem given by the reduced radial Schrödinger equation,

$$\left[-\frac{1}{2}\frac{\mathrm{d}^2}{\mathrm{d}r^2}+\frac{l(l+1)}{2r^2}+V(r)\right]u_{n,l}(r)=\varepsilon\, u_{n,l}(r), \tag{3.12}$$

where the solutions $u_{n,l}(r)=R_{n,l}(r)/r$ verify the following conditions:

$$\int_0^\infty u^*_{n,l}(r)u_{n,l}(r)\mathrm{d}r = 1, \tag{3.13}$$

$$u_{n,l}(0) = 0. \tag{3.14}$$

The exact solutions of Eq. (3.12) can be found analytically when using the Coulomb potential, given by Eq. (4.25). Concretely, the Coulomb solutions are divided in two energy domains. Firstly, for $\varepsilon<0$, the solutions are associated to the bound states of the electron, where energy ε only can take negative discrete values. This domain of solutions is named the *discrete spectrum*. On the other hand, for $\varepsilon>0$, the solutions will represent unbound, also called continuum, states of the electron. In this case, the energy ε can take every positive value and, for that reason, this domain is called as the *continuous spectrum*. Thus, an ideal numerical method should be able to compute both energy domains with a high precision. The B-spline representation has been presented as an appropriate numerical technique which allows us to describe the discrete and the continuous spectra at the same time. Within the B-spline representation, the initial step for solving numerically the Schrödinger equation is to assume that the solutions of Eq. (3.12) can be approximated by spline functions in $\mathbb{P}_{k,\xi,\nu}$. A formal proof of this assumption doesn't exist, however, experience has demonstrated the accuracy of such an approximation. Futhermore, the problem of searching the solutions $u_{n,l}(r)$ becomes the problem of searching the approximate spline functions $f_{n,l}(r)$ that verify Eq. (3.12) under the conditions Eq. (3.13) and Eq. (3.14). In this manner, one has

$$u_{n,l}(r)\approx f_{n,l}(r)=\sum_i c_i B^k_{i,t}(r), \tag{3.15}$$

where the notation can be simplified by means of

$$u_{n,l}(r)=\sum_i c_i B^k_{i,t}(r), \tag{3.16}$$

The question posed now concerns the choice of the appropriate parameters of the B-spline basis, that is, of the subspace $\mathbb{P}_{k,\xi,\nu}$. Once again, experience has shown that the choice of such parameters is essential for an accurate interpolation. However, there is not any rule or perfect recipe that dictates us which parameters must be used. In each specific case, the properties of the investigated problem are going to impose some constraints that must be adapted in the adequate subspace $\mathbb{P}_{k,\xi,\nu}$. Subsequently, one shall always investigate the optimal parameters of $\mathbb{P}_{k,\xi,\nu}$ in each specific problem. The freedom of choosing these parameters confers a high flexibility to the method, as we are going to see. Let us now investigate, within a practical case, the strengths and the weaknesses of this approximation. Let us solve the Schrödinger equation for the Hydrogen atom (i.e. $Z = 1$) which solutions are well known analytically.

3.2.1 Solving the Schrödinger equation in the subspace $\mathbb{P}_{k,\xi,\nu}$

First of all, and regarding the case of the hydrogen atom, let us discuss about the choice of the parameters of the space $\mathbb{P}_{k,\xi,\nu}$:

- **The order k:** In general, the greater the order, the greater the numerical precision. However, the computational cost required for the evaluation of B-splines also increases. The experience has shown that for a central potential, such as the Coulomb potential, an optimal order can be found between $k = 5$ and $k = 15$ [Bachau 01]. On the other hand, the kinetic energy term, presented in the total Hamiltonian, imposes a minimal order to B-splines. As we know, spline functions of order k, which approximate the solutions of Eq. (3.12), must present at least a continuous second derivative everywhere. To ensure this condition, the minimal order must be at least $k = 3$.

- **The sequence of breakpoints ξ:** The target solutions $u_{n,l}(r)$ are represented over a finite region of the space, enclosed between two endpoints: $\xi_{\text{min}} \equiv r_{\text{min}}$ and $\xi_{\text{max}} \equiv r_{\text{max}}$. Naturally, for solving Eq. (3.12), one chooses $r_{\text{min}} = 0$ bohr, while r_{max} determines the total size of the "simulation box" (the region of interest). As we are going to show later, the choice of r_{max} is crucial in different aspects, affecting the quality of the numerical solutions. On the other hand, by fixing the sequence of breakpoints, one controls the number of pieces (intervals) in which the space is divided. The number of intervals in the simulation box has a direct impact on the numerical precision. Breakpoints can be distributed

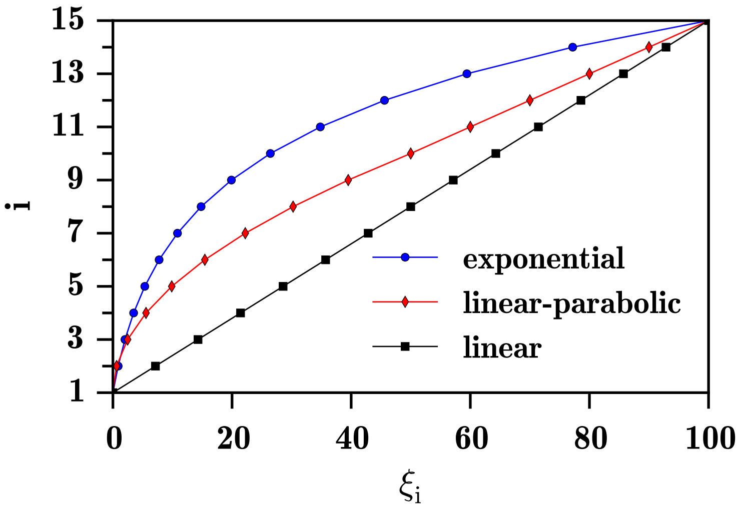

Figure 3.4: Different breakpoint sequences with $\xi_1 \equiv r_{\min} = 0$ bohr and $\xi_{15} \equiv r_{\max} = 100$ bohr.

easily in different manners in order to reach an accurate interpolation. In Figure 3.4, different breakpoint distributions are shown. If one is concerned with the computation of bound states, usually an exponential or a parabolic distribution is recommended. In this case, the points are localized close to $r_{\min}$ where one expects to describe the localized character of $u_{n,l}(r)$ with a high accuracy. Although, if one wants to properly reproduce the oscillations of the continuum states, a linear spacing is mandatory in order to achieve the same numerical accuracy over the whole space of interest.

- **The sequence of continuity conditions ν:** Usually, one chooses the maximal continuity limit at the inner breakpoints. As we have mentioned previously, hydrogen-like solutions must have a continuous second derivative in every interval of the sampled space. Differently, the treatment effectuated at the endpoints is conditioned by the boundary conditions of the studied problem. As our numerical solutions are obtained in a finite space region, additionally to the condition Eq. (3.14), one shall impose the following boundary condition

$$u_{n,l}(r_{\min}) = u_{n,l}(r_{\max}) = 0. \tag{3.17}$$

Then, one only searches those solutions which are zero at the borders of the simulation box. Henceforward, these boundary conditions can be achieved by imposing the minimal continuity limit at the bordered breakpoints, or simply by removing the first and the last B-spline functions from the basis.

- **The knot sequence t:** As we saw, this sequence defines the B-spline basis in $\mathbb{P}_{k,\xi,\nu}$. Thanks to the Curry-Schoenberg theorem, this sequence can be established by the breakpoints and the continuity conditions.

Once the parameters of $\mathbb{P}_{k,\xi,\nu}$ have been specially chosen for the problem of interest, and the knot sequence t has been established, a basis set of B-spline functions is immediately defined. The expansion of the solutions of Eq. (3.12) in terms of B-splines allows us to transform the differential equation into a linear algebra problem. Consequently, one finally works in a finite matrix space. At this point, the discrete nature of B-splines is revealed as a seductive issue from a computational point of view. In fact, the linear space of B-splines generate band matrices, which are a special type of sparse matrices for which optimal linear algebra algorithms exist [Anderson 99]. We note that this is not a trivial remark. Thanks to this particular aspect, high performance calculations can be carried out for big matrix dimensions, and currently associated numerical problems, such as *linear dependencies*, are almost inexistent and the idea of an *effective completeness* can be experienced. Let us now rewrite Eq. (3.12) within the *bra-ket* notation,

$$\hat{H}_l|u_{n,l}\rangle = \varepsilon_{n,l}|u_{n,l}\rangle, \tag{3.18}$$

where the hydrogen atom Hamiltonian is given by

$$\hat{H}_l = -\frac{1}{2}\frac{\mathrm{d}^2}{\mathrm{d}r^2} + \frac{l(l+1)}{2r^2} - \frac{1}{r}, \tag{3.19}$$

and the reduced radial wave functions are expressed in terms of B-splines such as

$$|u_{n,l}\rangle = \sum_{i=1}^{N_s} c_i^{n,l}|B_{i,t}^{k_s}\rangle, \tag{3.20}$$

where N_s is the dimension of the basis and k_s is the order of the B-splines[2]. If one multiplies Eq. (3.18) by $\langle B_{j,t}^{k_s}|$, a set of linear equations is obtained,

$$\sum_{i=1}^{N_s} c_i^{n,l}\langle B_{j,t}^{k_s}|\hat{H}_l|B_{i,t}^{k_s}\rangle = \varepsilon_{n,l}\sum_{i=1}^{N_s} c_i^{n,l}\langle B_{j,t}^{k_s}|B_{i,t}^{k_s}\rangle, \tag{3.21}$$

---

[2] From this moment, N_s is associated with the dimension of the basis and k_s with the order of the B-splines.

and the problem can be rewritten in the following compact matrix form

$$\mathbf{H}_l \, \mathbf{C} = \mathbf{E}_l \, \mathbf{S} \, \mathbf{C} \tag{3.22}$$

where $\mathbf{E}_l$ is a diagonal matrix that contains the eigenvalues $\{\varepsilon_{n,l}\}$, $\mathbf{C}$ is the vector matrix composed by the decomposition coefficients, and

$$\begin{aligned} \mathbf{H}_l \quad &= \{H_{i,j}\}_{i,j=1}^{N_s} \quad ; \quad \text{with} \;\; H_{i,j}^{l} = \langle B_{j,t}^{k_s} | \hat{H}_l | B_{i,t}^{k_s} \rangle, & (3.23) \\ \mathbf{S} \quad &= \{S_{i,j}\}_{i,j=1}^{N_s} \quad ; \quad \text{with} \;\; S_{i,j} = \langle B_{j,t}^{k_s} | B_{i,t}^{k_s} \rangle. & (3.24) \end{aligned}$$

The matrix $\mathbf{S}$ is positive defined and is called the “overlap matrix”. B-spline functions are non-orthogonal, and thus, overlaps between B-splines are not zero. The presence of $\mathbf{S}$ will impose the orthogonality to the solutions of Eq. (3.12). Finally, matrix elements can be evaluated as

$$\begin{aligned} H_{i,j} = \; & - \; \tfrac{1}{2} \int_{r_{\text{min}}}^{r_{\text{max}}} B_j(r) \left[\tfrac{\mathrm{d}^2}{\mathrm{d}r^2} B_i(r) \right] \mathrm{d}r \\ & + \; \tfrac{l(l+1)}{2} \int_{r_{\text{min}}}^{r_{\text{max}}} B_j(r) \; \tfrac{1}{r^2} \; B_i(r) \mathrm{d}r \\ & - \; \int_{r_{\text{min}}}^{r_{\text{max}}} B_j(r) \; \tfrac{1}{r} \; B_i(r) \mathrm{d}r, \end{aligned} \tag{3.25}$$

and

$$S_{i,j} \quad = \quad \int_{r_{\text{min}}}^{r_{\text{max}}} B_j(r) B_i(r) \mathrm{d}r, \tag{3.26}$$

where the knot sequence t and the order k_s have been removed from the expressions for clarity. The one-electron integrals over B-splines in Eq. (3.25) and Eq. (3.26) can be performed up to machine accuracy using Gauss-Legendre quadrature, see Appendix C. Moreover, thanks to the compact support of B-splines, one verifies that

$$H_{i,j} = S_{i,j} = 0 \;\; \forall \; j - k \geq i \geq j + k. \tag{3.27}$$

As a consequence, sparse matrices $\mathbf{H}_l$ and $\mathbf{S}$ are composed by a single diagonal band of $2k - 1$ nonzero elements. If one adds to this issue the fact that $\mathbf{H}_l$ and $\mathbf{S}$ are symmetric matrices, one only needs to compute $N_s(k_s + 1)$ elements instead of N_s^2 for a $N_s \times N_s$ matrix. At this point, we are addressing the resolution of the eigenvalue problem Eq. (3.22). Different methods are proposed in the literature [Press 07]. However, from a practical point of view, one can directly implement the optimized routines specially designed for band matrices in LAPACK (Linear Algebra Package) [Anderson 99]. On the other hand, if a specific eigenvalue or eigenfunction is required, the inverse iteration method can be easily implemented, see also [Press 07]. Nevertheless, we recall that the inverse iteration method is useless for continuum states. Therefore, other kind of techniques, such as the "shooting method", shall be implemented [Caillat 15]. In general, it is obvious that one will select a method that allows us to take advantage of the structure of the implicated matrices, especially when we have to deal with huge matrix dimensions.

Independently of the chosen numerical resolution method, in this section attention is focused strictly on the B-spline representation of the solutions of Eq. (3.12). We pass now to show our results on the hydrogen atom. In order to validate our implementation of B-splines, our results can be easily compared with the results presented by E. Cormier in his PhD thesis [Cormier 94] and by Bachau *et al.* [Bachau 01].

3.2.2 Eigenvalues and eigenfunctions

After solving the eigenvalue problem Eq. (3.22), solutions of Eq. (3.12) are given as an ensemble of discrete states of negative and positive energies. Therefore, one takes the negative solutions as a representation of the electron bound states, while the positive discrete states shall be interpreted as "continuum" states. In Table 3.2, a set of bound states is shown together with the differences between the computed and the exact eigenvalues. These differences, displayed as "δ", establish the deviation of the computed values from the exact ones. As the exact solutions are known, converged results are numerically obtained only when the machine accuracy is achieved, that is when the differences are lower or equal than the threshold $\delta_{\text{machine}} = 10^{-12}$.

Table 3.2: Hydrogen atom eigenvalues computed with a B-spline basis set of $N_s = 400$, $k_s = 8$, $r_{\max} = 200$ bohr and using a linear sequence of breakpoints. Numerical error is given in terms of $10^{-\delta}$. A very high accuracy is obtained up tu $n = 6$.

n	ε_{ns}	δ	ε_{np}	δ	ε_{nd}	δ	ε_{nf}	δ	ε_{ng}	δ
1	-0.50000000	14								
2	-0.12500000	13	-0.12500000	14						
3	-0.05555555	13	-0.05555555	13	-0.05555555	13				
4	-0.03125000	13	-0.03125000	13	-0.03125000	14	-0.03125000	13		
5	-0.02000000	13	-0.02000000	13	-0.02000000	13	-0.02000000	13	-0.02000000	13
6	-0.01388888	13	-0.01388888	13	-0.01388888	13	-0.01388888	13	-0.01388888	13
7	-0.01020408	9	-0.01020408	9	-0.01020408	9	-0.01020408	9	-0.01020408	10
8	-0.00781238	5	-0.00781240	5	-0.00781242	6	-0.00781245	6	-0.00781248	6

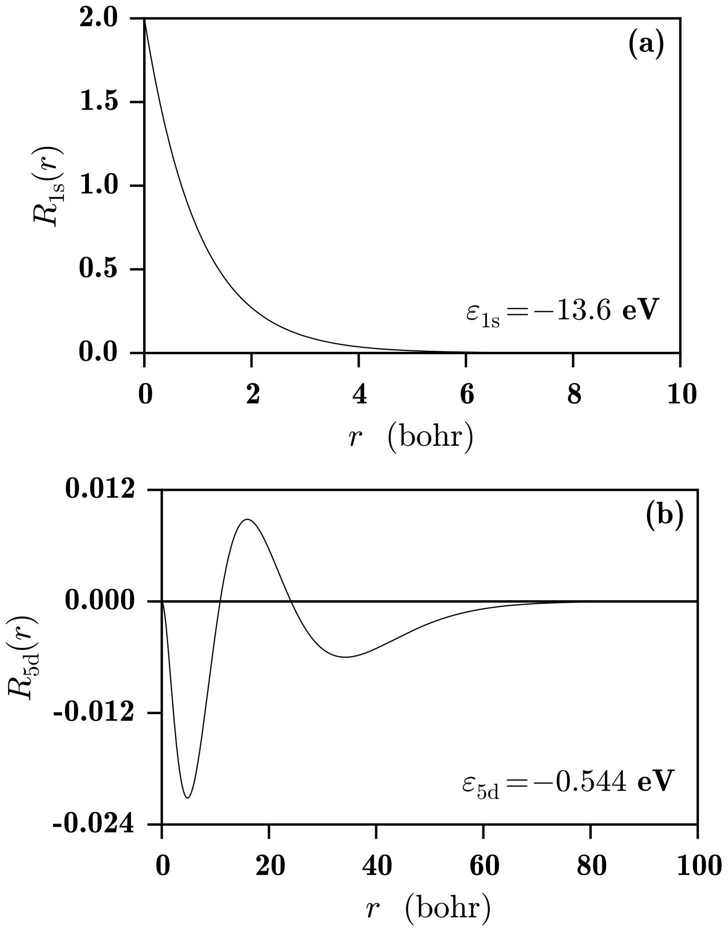

Figure 3.5: Hydrogen atom radial wave functions: 1s (a) and 5d (b) orbitals. Calculation performed with the following B-spline parameters: $N_s = 400$, $k_s = 8$, $r_{\max} = 200$ bohr and using a linear sequence of breakpoints.

In addition, the quality of the computed eigenfunctions Figure 3.5 can be quantify with the calculation of the expectation values of the powers of the electron position r, which are given by

$$\langle r^\nu \rangle_{n,l} = \int_0^\infty r^\nu |R_{n,l}(r)|^2 r^2 \mathrm{d}r. \tag{3.28}$$

Table 3.3: Analytical expressions of the expectation values $\langle r^\nu \rangle_{n,l}$ for the hydrogen atom (i.e. $Z = 1$) have been taken from Bethe and Salpeter's monograph *"Quantum Mechanics of One- and Two-Electron Atoms"* [Bethe 57].

ν	Analytical expressions of $\langle r^\nu \rangle_{n,l}$ for $Z = 1$
1	$[3n^2 - l(l+1)]/2$
2	$[5n^2 + 1 - 3l(l+1)]\ n^2/2$
3	$[35n^2(n^2-1) - 30n^2(l+2)(l-1) + 3(l+2)(l+1)l(l-1)]\ n^2/8$
4	$[63n^4 - 35n^2(2l^2+2l-3) + 5l(l+1)(3l^2+3l-10) + 12]\ n^4/8$
-1	$1/n^2$
-2	$(l+1/2)/n^3$

The expectation values $\langle r^{\nu}\rangle_{n,l}$ are interesting quantities related to observables that are well known in the case of one-electron atoms. For instance, Table 3.3 presents the analytical expressions of Eq. (3.28) for the Hydrogen atom. Subsequently, a comparison between the computed expectation values $\langle r^{\nu}\rangle_{n,l}$ and the analytical results given in Table 3.3 will give us the information about the quality of our numerical method. Figure 3.6 displays the numerical errors (the differences) between the computed and the exact values for different angular momenta up to the level $n = 12$. As one observes, up to the level $n = 7$, the numerical accuracy of our method is correct. In fact, the differences are found under the machine accuracy. However, above $n = 7$, the differences between the computed and the exact eigenfunctions start to be important.

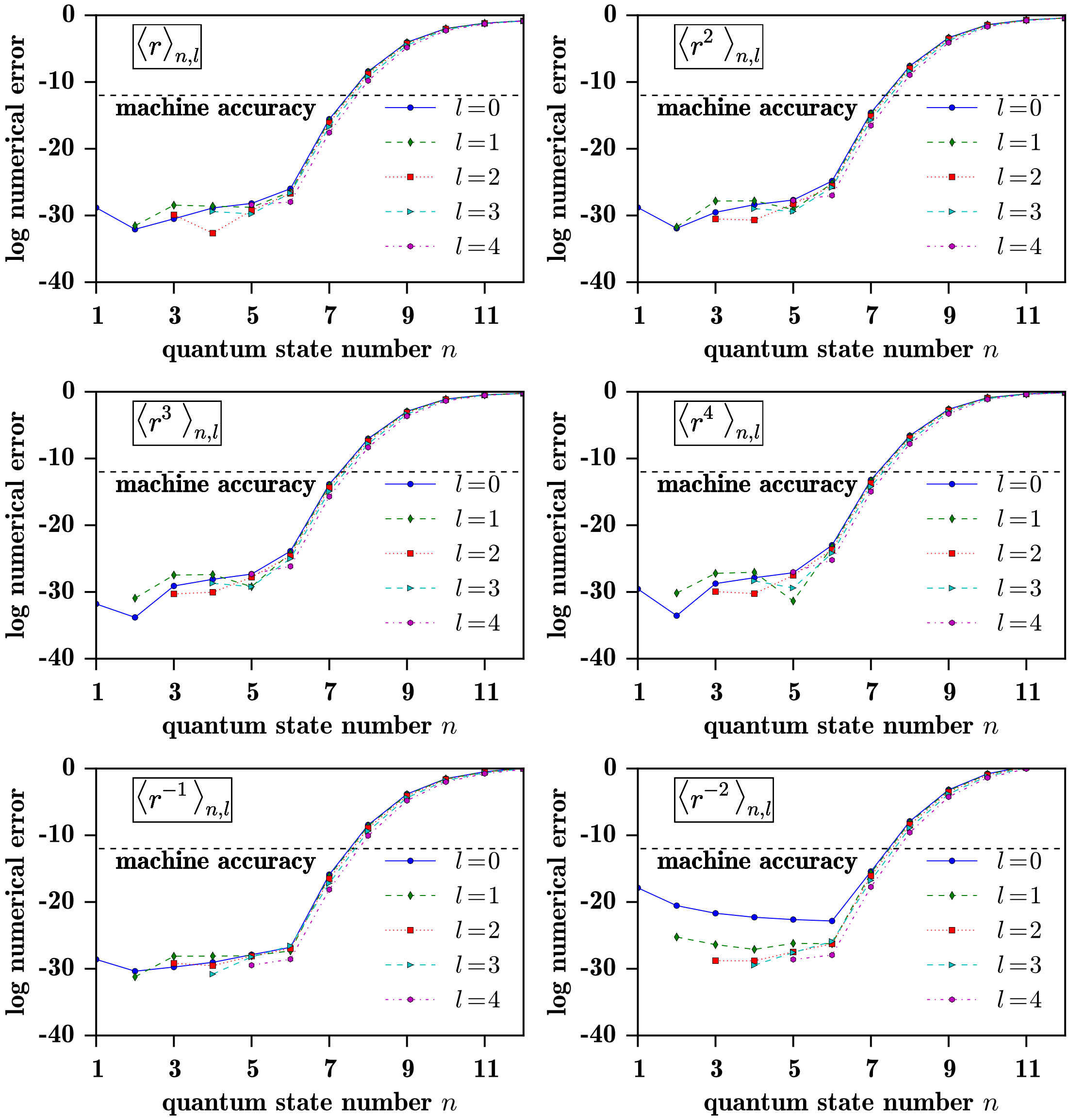

Figure 3.6: Numerical accuracy of the computed eigenfunctions for the hydrogen atom expressed in terms of the expectation values $\langle r^{\nu}\rangle_{n,l}$ for the first few bound states. B-spline parameters: $N_s = 400$, $k_s = 8$, $r_{\max} = 200$ bohr and linear sequence of breakpoints.

The reason of the deviations observed in Figure 3.6 is directly related to the fact that the hydrogen atom has been enclosed in a finite simulation box by imposing specific boundary conditions at the endpoints Eq. (3.17). This issue is translated to the addition of an artificial infinite potential barrier at $r = r_{\text{max}}$, where solutions must be zero. Then, the electron is finally affected by an effective potential $V_{\text{eff}}(r)$ that reads as

$$V_{\text{eff}}(r) = \begin{cases} \frac{l(l+1)}{2r^2} - \frac{1}{r} & \text{if} \quad 0 < r < r_{\text{max}}, \\ +\infty & \text{if} \quad r_{\text{max}} \leq r \quad . \end{cases} \tag{3.29}$$

In Figure 3.7, $V_{\text{eff}}(r)$ has been represented. Moreover, it is noticeable that the eigenfunctions associated to the Hamiltonian composed by $V_{\text{eff}}(r)$ are not the pure hydrogen atom solutions. However, experience shows us that increasing the size of the simulation box, that is, the value of r_{max}, the number of accurate solutions increases. In Table 3.4, the box size effects are exposed. The number n_{max} indicates the maximal quantum level used to calculate the expectation values $\langle r^\nu \rangle_{n,l}$ within the machine accuracy (i.e. $\delta_{\text{machine}} = 10^{-12}$).

Table 3.4: Size box effects. n_{max} indicates the maximal quantum level used to compute the expectation values $\langle r^\nu \rangle_{n,l}$ within the machine accuracy (i.e. $\delta_{\text{machine}} = 10^{-12}$). Calculations have been carried out with the following B-spline parameters: $k_s = 8$, and the number of B-splines has been modified in order to keep constant the breakpoint spacing $\Delta\xi \equiv \Delta r$.

r_{max}	bound states	n_{max}
100	8	4
200	12	7
500	19	12
1000	28	19

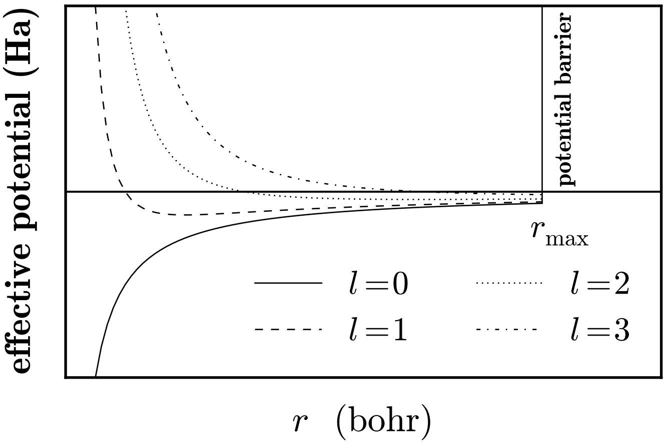

Figure 3.7: Representation of the effective potential $V_{\text{eff}}(r)$ for different angular momentum of an hydrogen atom enclosed in a box of size r_{max}. Figure inspired from [Cormier 94].

We observe that, for a linear sequence of breakpoints with a constant spacing $\Delta\xi \equiv \Delta r$, the number of bound states, as well as the quantum level $n_{\max}$, increases with the size box $r_{\max}$. The inaccurate computed states, those with a quantum number $n > n_{\max}$, can be interpreted as a set of "pseudo-Rydberg" states of the atom [Cormier 94].

3.2.3 B-spline parameters and numerical accuracy

For a given box size $r_{\max}$, the accuracy of a computed state can be increased by selecting an appropriate couple of parameters N_s and k_s, that is, by choosing the appropriate number of breakpoints and knots in the interval $[r_{\min}, r_{\max}]$. However, the converge rate of both parameters N_s and k_s is different. Experience shows us that depending on the required degree of accuracy, there is always an optimal couple (N_s, k_s) in terms of CPU time. Figure 3.8 shows different (N_s, k_s) couples achieving different degrees of accuracy on the hydrogen atom ground state energy, i.e. ε_{1s}. For excited states (not shown here), the converge behavior is very similar. In general, the higher k_s the lower the dimension N_s to reach a particular numerical accuracy. Usually, the order k_s is chosen to be in the range $k_s \in [7, 11]$ [Bachau 01].

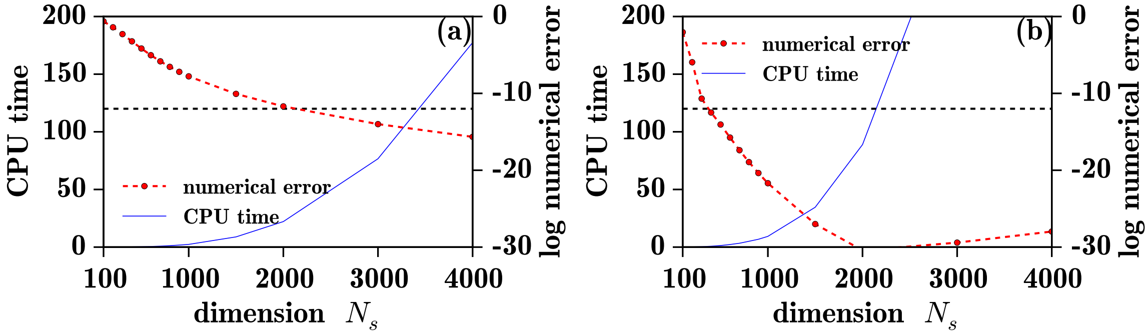

Figure 3.8: Convergence of two (N_s, k_s)-couples on the ground state energy ε_{1s}: (a) presents the couple $(N_s, 4)$ and (b) the couple $(N_s, 8)$. Box size is $r_{\max} = 1000$ bohr and the breakpoint sequence is chosen to be linear. Black dashed line represents machine accuracy.

3.2.4 Continuum states

The fact of enclosing our atomic system in a finite space region (simulation box of size $r_{\max}$) and imposing to solutions some specific boundary conditions, i.e. Eq. (3.17), translates to an effective potential $V_{\text{eff}}(r)$ in which an infinite potential barrier is placed at $r = r_{\max}$. Due to this effective potential, negative and positive solutions are given as an ensemble of discrete states. We have discussed the effects of the box size and the B-spline parameters on bound states (negative solutions), and one can

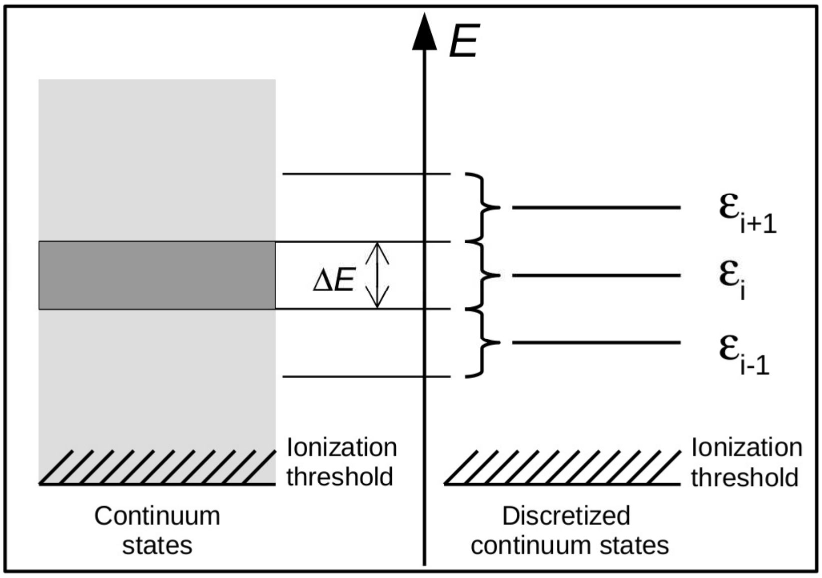

Figure 3.9: Interpretation of the discrete positive states. Figure inspired from [Cormier 94].

say that, the bigger the box size the lower the influences of the infinite potential barrier on the solutions. Thus, when the box size goes to infinity, $V_{\text{eff}}(r)$ becomes the pure atomic potential (which for the Hydrogen atom is the Coulomb potential). Consequently, more accurate results are obtained. On the other side, the discrete positive solutions must be interpreted as the atomic continuum states. Figure 3.9 shows an interpretation of the positive solutions of energy $\varepsilon_i > 0$. Each of this discrete states is considered as a band of continuum states with an energy width of ΔE. This discretized representation of the exact continuum approaches the exact continuum when the density of positive states goes to infinity, and then, the band width ΔE reduces to zero ($\Delta E \to 0$). The density of states is controlled by the box size and the number of B-splines in the basis.

In addition, eigenfunctions associated to the discrete positive energies shall reproduce the asymptotic sinusoidal behavior of the pure continuum states, see for instance Figure 3.10. For a given box size r_{max}, this behavior can be reproduced by choosing the correct B-splines parameters (N_s, k_s). At this particular point, one appreciates the flexibility of B-splines to accurately reproduce the oscillating behavior of the continuum states. In Figure 3.11, a wave function is displayed together with its weighted B-spline decomposition. We remark the quasi-absence of cancellations when describing the sign switches.

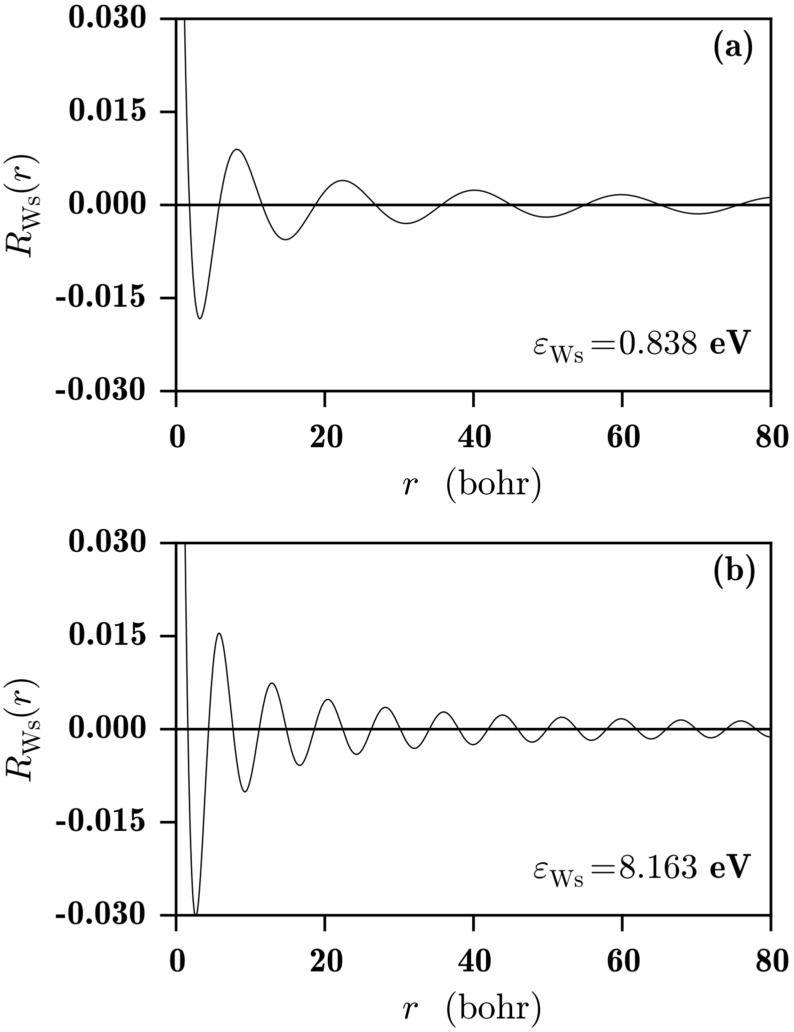

Figure 3.10: Energy normalized radial wave functions for two continuum states of symmetry "s". B-spline parameters: $N = 400$, $k = 8$, $r_{\max} = 200$ bohr and linear sequence of breakpoints.

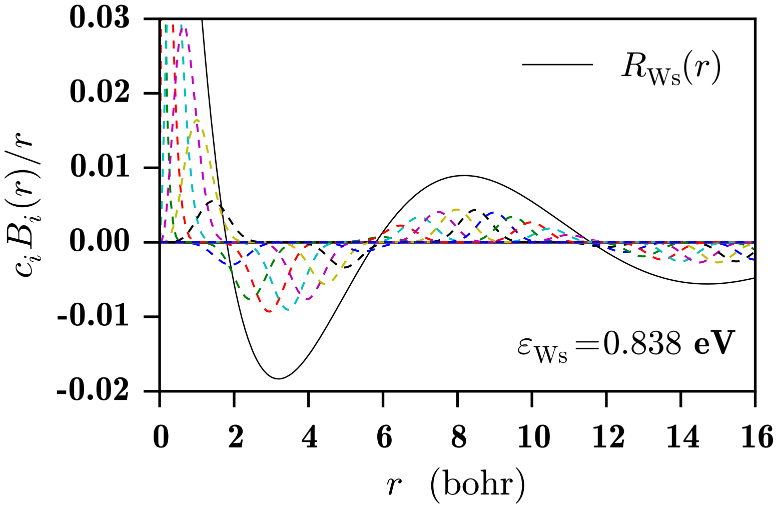

Figure 3.11: Weighted B-spline decomposition of a given continuum radial wave function of symmetry "s". B-spline parameters: $N = 400$, $k = 8$, $r_{\max} = 200$ bohr and linear sequence of breakpoints.

3.2.4.1 Energy spectrum

Figure 3.12 presents different energy spectra calculated with different r_{max} values. One observes that the number of discrete positive states increases with r_{max}. This behavior is a natural consequence of describing the hydrogen atom in a finite space region. In fact, the behavior observed in Figure 3.12 is identical to that of a free particle enclosed in a box with infinite potential barriers. We recall that the energy of a free particle in a box is given by

$$\varepsilon_i = \frac{i^2\,\pi^2}{2\,r_{\text{max}}^2} \quad \text{with} \quad i = 1, 2, \ldots \tag{3.30}$$

In addition, the box size effects on the computed discrete state energies $\{\varepsilon_i\}$ can be explored by slowly varying r_{max}. In Figure 3.13, one observes how energies are displaced when r_{max} increases. It is interesting to see, for example, how the state ε_{53} crosses the energy range ΔE simply by the fact of changing the value of r_{max}. Thus, in principle, any desired continuum state energy could be computed within our method using the corresponding B-spline parameters. Note that the curves are not straight lines but they change as $1/r_{\text{max}}^2$.

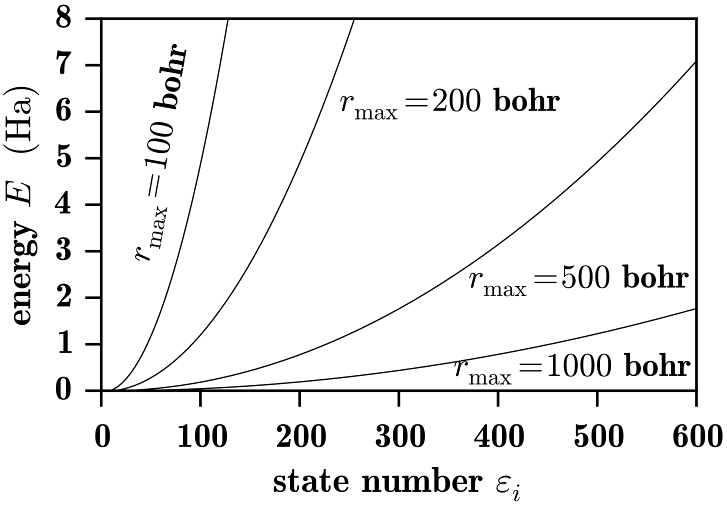

Figure 3.12: Energy spectra of discretized continuum states for different values of r_{max}. The dimension N_s of the basis is changed to keep constant the density of B-splines and the knot spacing. The order of B-splines was chosen to be $k_s = 8$ and the breakpoint sequence was of the linear form.

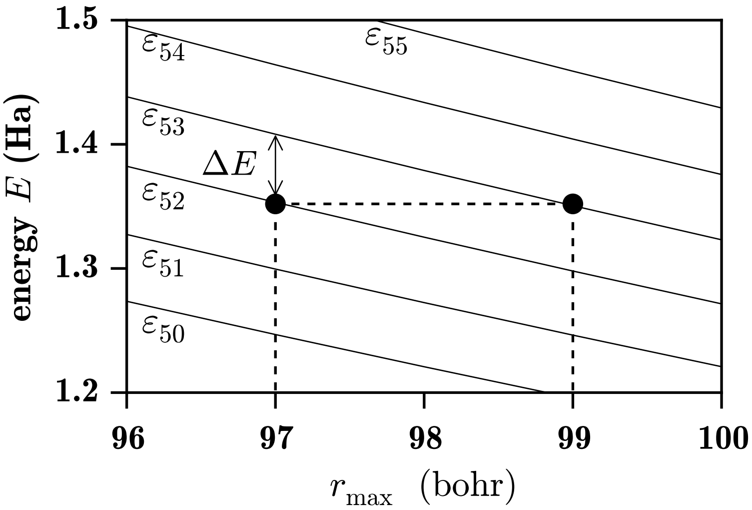

Figure 3.13: Size box effects on a series of discretized continuum states. We observe the state energy as a function of the box size $r_{\max}$. B-spline parameters: $N_s = 100$, $k_s = 8$ and the breakpoint sequence is linear.

3.2.4.2 Density of states

For a given angular symmetry, the radial density of states (DOS) is defined as the number of states per unit of energy. Figure 3.14 displays the DOS for the hydrogen atom computed with different values of $r_{\max}$. As we observed, the DOS increases with $r_{\max}$. As we previously saw, the continuum spectrum of the hydrogen atom, computed in a finite space region, is similar to the spectrum of a free particle enclosed in a box. As a consequence, the curves observed in Figure 3.14 can be fitted by the expression

$$\rho(\varepsilon) = \frac{1}{\pi\sqrt{2}}\frac{r_{\max}}{\sqrt{\varepsilon}}, \tag{3.31}$$

where $\rho(\varepsilon)$ is the DOS for a free particle in a box with infinite potential barriers.

From a computational point of view, the calculation of the DOS is not an easy task. However, if we assume that number of discretized continuum states in our calculation is infinity, the computed positive energies $\{\varepsilon_i\}$ can be associated to a continuous energy function $\tilde{\varepsilon}$ such as $\varepsilon_i = \tilde{\varepsilon}(i)\ \forall i$, see for instance [Macías 88, Cormier 94]. In order to obtain the DOS, one has to face the computation of the derivative of the energy with respect to the state index number, that is

$$\left.\frac{\partial \tilde{\varepsilon}(x)}{\partial x}\right|_{x=i}. \tag{3.32}$$

Eq. (3.32) can be estimated performing a Taylor expansion (for example, up to

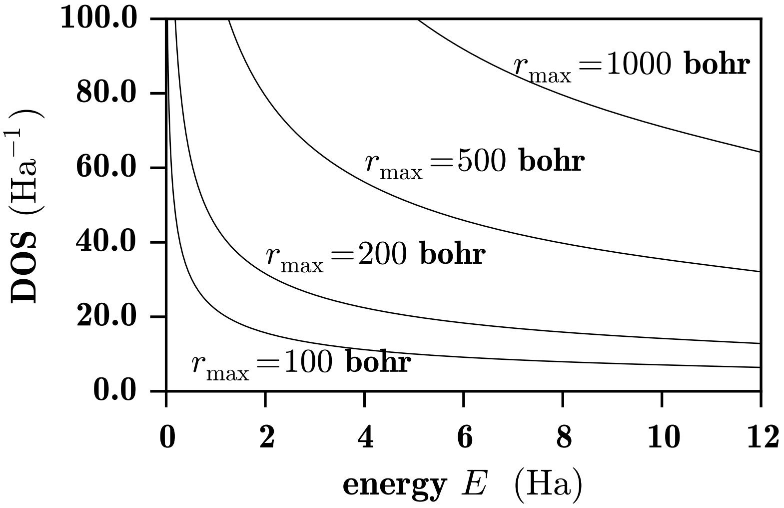

Figure 3.14: Box size effects on the density of states (DOS). The dimension N of the basis is changed in order to keep constant the density of B-splines and the knot spacing with respect $r_{\max}$, the order of B-splines is $k_s = 8$.

the 3rd order) of the function $\tilde{\varepsilon}(x)$ in $x = i - 1$ and $x = i + 1$, such as

$$\tilde{\varepsilon}(i+1) = \varepsilon_{i+1} = \varepsilon_i + \left.\frac{\partial \tilde{\varepsilon}}{\partial x}\right|_{x=i} + \frac{1}{2}\left.\frac{\partial^2 \tilde{\varepsilon}}{\partial x^2}\right|_{x=i} + \frac{1}{6}\left.\frac{\partial^3 \tilde{\varepsilon}}{\partial x^3}\right|_{x=i} \tag{3.33}$$

$$\tilde{\varepsilon}(i-1) = \varepsilon_{i-1} = \varepsilon_i - \left.\frac{\partial \tilde{\varepsilon}}{\partial x}\right|_{x=i} + \frac{1}{2}\left.\frac{\partial^2 \tilde{\varepsilon}}{\partial x^2}\right|_{x=i} - \frac{1}{6}\left.\frac{\partial^3 \tilde{\varepsilon}}{\partial x^3}\right|_{x=i} \tag{3.34}$$

and by difference one has

$$\left.\frac{\partial \tilde{\varepsilon}}{\partial x}\right|_{x=i} \approx \frac{\Delta \tilde{\varepsilon}}{\Delta x} = \frac{\varepsilon_{i+1} - \varepsilon_{i-1}}{2} + \frac{1}{6}\left.\frac{\partial^3 \tilde{\varepsilon}}{\partial x^3}\right|_{x=i}, \tag{3.35}$$

where the last term takes into account the variations of the curve $\tilde{\varepsilon}(x)$. In the case of a Coulomb potential enclosed in a finite box, the derivative can be approximated to the first term as

$$\left.\frac{\partial \tilde{\varepsilon}}{\partial x}\right|_{x=i} \approx \frac{\varepsilon_{i+1} - \varepsilon_{i-1}}{2}. \tag{3.36}$$

Thus, the DOS of an ensemble of discretized continuum states can be expressed as the inverse of Eq. (3.36), such as

$$\rho(\varepsilon_i) = \frac{2}{\varepsilon_{i+1} - \varepsilon_{i-1}}. \tag{3.37}$$

3.2.4.3 Normalization of the continuum wave functions

The last aspect that must be discussed is the normalization problem of the computed discretized continuum wave functions. Due to the imposed boundary conditions, every solution of Eq. (3.12) is orthonormalized in the index scale as follows,

$$\langle \Psi_i | \Psi_j \rangle = \delta_{i,j}. \tag{3.38}$$

However, as we know, the continuous solutions must be orthonormalized in the energy scale, that is, by the rule

$$\langle \Psi_{E'} | \Psi_E \rangle = \delta(E' - E). \tag{3.39}$$

Thus, the normalization problem is to find the adequate normalization coefficient to pass from the index scale (index representation) to the energy scale (energy representation). This problem has been attacked from different angles, here we present the most general technique [Landau 77].

For a given set of wave functions, which are orthonormalized over the discrete scale-variable "σ", that is

$$\langle \Psi_{\sigma'} | \Psi_\sigma \rangle = \delta(\sigma' - \sigma), \tag{3.40}$$

we look for having a different orthonormalization over the scale-variable "$h(\sigma)$", which depends on "σ". Then, we also have

$$\langle \Psi_{h(\sigma')} | \Psi_{h(\sigma)} \rangle = \delta(h(\sigma') - h(\sigma)). \tag{3.41}$$

If σ' approaches σ, one has that $h(\sigma') - h(\sigma) = [\mathrm{d}h(\sigma)/\mathrm{d}\sigma](\sigma' - \sigma)$, and from the properties of the delta function [3], one can write $\delta(h(\sigma') - h(\sigma)) = |\mathrm{d}h(\sigma)/\mathrm{d}\sigma|^{-1}\delta(\sigma' - \sigma)$, where $|\mathrm{d}h(\sigma)/\mathrm{d}\sigma|^{-1}$ is a constant. Consequently, we have

$$\langle \Psi_{h(\sigma')} | \Psi_{h(\sigma)} \rangle = \frac{1}{|\mathrm{d}h(\sigma)/\mathrm{d}\sigma|}\delta(\sigma' - \sigma). \tag{3.42}$$

By comparing Eq. (3.40) and Eq. (3.42), we deduce that the normalization factor

---

[3] We recall that the delta function is defined as $\delta(x) = 0$ for $x \neq 0$ and $\delta(0) = +\infty$. Some of its properties are:

(i) $\int_{-\infty}^{+\infty} \delta(x)\mathrm{d}x = 1$;

(ii) $\int_{-\infty}^{+\infty} \delta(x - a)f(x)\mathrm{d}x = f(a)$;

(iii) $\delta(-x) = \delta(x)$;

(iv) $\delta(\alpha x) = |\alpha|^{-1}\delta(x)$, where α is a constant.

between the σ and the $h(\sigma)$ scales must be given by

$$|\Psi_{h(\sigma)}\rangle = \frac{1}{\sqrt{|\mathrm{d}h(\sigma)/\mathrm{d}\sigma|}}|\Psi_{\sigma}\rangle. \tag{3.43}$$

In our particular case, the derivative $\mathrm{d}h(\sigma)/\mathrm{d}\sigma$ is given by the derivative of the energy with respect to the state index number, that is, Eq. (3.32). In consequence, as reported in the previous section, we can state that the normalization coefficient is determined by the DOS. The conversion from the index scale normalization to the energy scale normalization is finally given by

$$|\Psi_{\varepsilon_i}\rangle = \rho(\varepsilon_i)^{1/2}|\Psi_i\rangle = \sqrt{\frac{2}{\varepsilon_{i+1}-\varepsilon_{i-1}}}|\Psi_i\rangle, \tag{3.44}$$

where $|\Psi_{\varepsilon_i}\rangle$ symbolized the energy normalized states and $|\Psi_i\rangle$ the states obtained directly from our numerical calculation.

3.3 SOLVING THE TIME-DEPENDENT SCHRÖDINGER EQUATION

In this section, the resolution of the time-dependent Schrödinger equation (TDSE) within the B-spline representation for the case of an hydrogen-like atom is presented. We recall that the TDSE is given (in atomic units) by

$$i\frac{\partial}{\partial t}|\Psi(t)\rangle = \hat{H}(t)|\Psi(t)\rangle, \tag{3.45}$$

where time-dependent Hamiltonian is given by $\hat{H}(t) = \hat{H}_0 + \hat{H}_{\mathrm{int}}(t)$, where $\hat{H}_0$ is the field-free Hamiltonian,

$$\hat{H}_0 = \left[-\frac{1}{2}\frac{\partial^2}{\partial r^2} - \frac{1}{r}\frac{\partial}{\partial r} + \frac{1}{2}\frac{\hat{L}^2}{r^2} - \frac{Z}{r}\right], \tag{3.46}$$

where $\hat{L}^2$ is the angular momentum operator. The interaction Hamiltonian $\hat{H}_{\mathrm{int}}(t)$ can be expressed in the length or in the velocity gauge in spherical polar coordinates for a linear polarized electric field along the z-axis as

$$\begin{aligned} \hat{H}^{L}_{\mathrm{int}}(t) &= \mathcal{E}(t)\, r\cos\theta, & (3.47)\\ \hat{H}^{V}_{\mathrm{int}}(t) &= -iA(t)\left[cos\theta\frac{\partial}{\partial r} - \frac{sin\theta}{r}\frac{\partial}{\partial\theta}\right], & (3.48) \end{aligned}$$

where $\mathcal{E}(t)$ is the external electric field and the potential vector is defined as $A(t) = -\int_t^{\tau} \mathcal{E}(t')\mathrm{d}t'$, where τ is the duration of the laser pulse.

The time-dependent wave function $|\Psi(t)\rangle$ is composed by an angular part, given by the spherical harmonics $(Y_l^m(\Omega) \equiv Y_l^m(\theta,\phi))$, and a radial part, which is represented within the B-spline basis $(B_\nu(r) \equiv B_{\nu,t}^{k_s}(r))$ in the interval $[0, r_{\max}]$ as follows,

$$\Psi(\mathbf{r},t) = \sum_{\nu=1}^{N_s} \sum_{l=0}^{l_{\max}} \sum_{m=-l}^{+l} c_\nu^{l,m}(t) \frac{B_\nu(r)}{r} Y_l^m(\Omega), \tag{3.49}$$

where the decomposition coefficients $\{c_\nu^{l,m}(t)\}$ take into account the temporal dependence of the wave function. The use of this expansion translates Eq. (3.45) into its matrix form such as

$$i\,\mathbf{S}\,\frac{\mathrm{d}}{\mathrm{d}t}\mathbf{C}(t) = [\mathbf{H}_0 + \mathbf{H}_{\mathrm{int}}(t)]\,\mathbf{C}(t), \tag{3.50}$$

where $\mathbf{S}$ is the overlap matrix, $\mathbf{H}_0$ the field-free Hamiltonian and $\mathbf{H}_{\mathrm{int}}(t)$ is the electric field interaction matrix.

This equation can be solved using different numerical methods. In the following subsection, the Crank-Nicolson technique is briefly presented.

3.3.1 Time discretization

As we know, the formal solution of the TDSE can be written in terms of the time evolution operator such as

$$\begin{aligned} |\Psi(t)\rangle &= \hat{U}(t,t_0)|\Psi(t_0)\rangle \\ &= \hat{U}(t=t_n,t_{n-1})...\hat{U}(t_2,t_1)\hat{U}(t_1,t_0)|\Psi(t_0)\rangle, \end{aligned} \tag{3.51}$$

where $\hat{U}(t_{i+1},t_i)$ drives our system from time t_i to t_{i+1}. The temporal integration is then performed step by step from t_0 to t. The explicit form of $\hat{U}(t_{i+1},t_i)$ is given by

$$\hat{U}(t_{i+1},t_i) = \hat{T}\exp\left\{-i\int_{t_i}^{t_{i+1}} \hat{H}(t')\mathrm{d}t'\right\}, \tag{3.52}$$

where $\hat{T}$ is the time-ordering operator. Moreover, if the time step Δt (i.e. $\Delta t = t_{i+1} - t_i$) is small enough, the time evolution operator $\hat{U}(t_{i+1},t_i)$ can be approached by a simple first-order Taylor expansion in Δt. However, this leads to an error in Δt^2 and the norm of the time-dependent wave function can be lost during the time evolution. To avoid these issues, Crank *et al.* [Crank 47] proposed a technique which is unitary and the error is in Δt^3. This method is based in a truncated series expansion, allowing us to write that

$$|\Psi(t+\Delta t)\rangle \approx \left[\mathbb{I} - i\hat{H}\left(t+\frac{\Delta t}{2}\right)\frac{\Delta t}{2}\right]\left[\mathbb{I} + i\hat{H}\left(t+\frac{\Delta t}{2}\right)\frac{\Delta t}{2}\right]^{-1}|\Psi(t)\rangle, \tag{3.53}$$

where the integrand of Eq. (3.52) has been evaluated at the middle point of the time interval $[t, t+\Delta t]$. If now, Eq. (3.49) is used in Eq. (3.53), one can obtain the following equation for the expansion coefficients,

$$\mathbf{A}\left(t+\frac{\Delta t}{2}\right)\mathbf{C}(t+\Delta t) = \mathbf{C}'(t), \tag{3.54}$$

where the matrix $\mathbf{A}$ is defined for every time t as

$$\mathbf{A}\,(t) = \left[\mathbf{S} + i\left\{\mathbf{H}_0 + \mathbf{H}_{\text{int}}\,(t)\right\}\frac{\Delta t}{2}\right], \tag{3.55}$$

and the vector $\mathbf{C}'(t)$ is given by the product

$$\mathbf{C}'(t) = \left[\mathbf{S} - i\left\{\mathbf{H}_0 + \mathbf{H}_{\text{int}}\left(t+\frac{\Delta t}{2}\right)\right\}\frac{\Delta t}{2}\right]\mathbf{C}(t). \tag{3.56}$$

In order to solve Eq. (3.54), one shall perform two operations: (1) a vector-matrix product in Eq. (3.56) and (2) the inversion of matrix $\mathbf{A}$. When working with large basis set dimensions, this operations can be very costly. The inversion can be performed using a method based on the Krylov space, for example, the biconjugate gradient method, see for instance [Press 07].

3.3.2 Computation of the B-spline matrix elements

The evaluation of the B-spline matrix elements requires the calculation of radial and angular integrals. Radial integrals are going to be computed numerically, while the angular integrals are calculated analytically with the help of the recurrence relations of the spherical harmonics. In Appendix B, we recall definitions and relations of spherical harmonics.

We now determine the different matrix elements in Eq. (3.50).

Overlap matrix elements $(S_{\mu,\nu})_{l,l'}^{m,m'}$:

$$\begin{aligned}
(S_{\mu,\nu})_{l,l'}^{m,m'} &= \int_0^{r_{\max}} \int \tfrac{B_\mu(r)}{r} Y_{l'}^{m'}(\Omega) \times \tfrac{B_\nu(r)}{r} Y_l^m(\Omega) r^2 \mathrm{d}r\mathrm{d}\Omega \\
&= \int_0^{r_{\max}} B_\mu(r) B_\nu(r) \mathrm{d}r \times \int Y_{l'}^{m'}(\Omega) Y_l^m(\Omega)\mathrm{d}\Omega \\
&= \langle \mu | \nu \rangle \; \delta_{l',l} \; \delta_{m',m}.
\end{aligned} \tag{3.57}$$

Field-free Hamiltonian matrix elements $(H^0_{\mu,\nu})_{l,l'}^{m,m'}$:

$$\begin{aligned}
(H^0_{\mu,\nu})_{l,l'}^{m,m'} &= \int_0^{r_{\max}} \int \tfrac{B_\mu(r)}{r} Y_{l'}^{m'}(\Omega) \left[-\tfrac{1}{2}\tfrac{\partial^2}{\partial r^2} - \tfrac{1}{r}\tfrac{\partial}{\partial r} + \tfrac{1}{2}\tfrac{\hat{L}^2}{r^2} - \tfrac{1}{r} \right] \tfrac{B_\nu(r)}{r} Y_l^m(\Omega) r^2 \mathrm{d}r\mathrm{d}\Omega \\
&= \int_0^{r_{\max}} \int \tfrac{B_\mu(r)}{r} Y_{l'}^{m'}(\Omega) \left[-\tfrac{1}{2}\tfrac{\partial^2}{\partial r^2} \left[\tfrac{B_\nu(r)}{r}\right] - \tfrac{1}{r}\tfrac{\partial}{\partial r}\left[\tfrac{B_\nu(r)}{r}\right] \right. \\
&\quad \left. + \tfrac{l(l+1)}{2}\tfrac{B_\nu(r)}{r^3} - \tfrac{B_\nu(r)}{r^2} \right] Y_l^m(\Omega) r^2 \mathrm{d}r\mathrm{d}\Omega \\
&= \int_0^{r_{\max}} \int \tfrac{B_\mu(r)}{r} Y_{l'}^{m'}(\Omega) \left[-\tfrac{1}{2} \left[\tfrac{r^2 B''_\nu(r) - 2r B'_\nu(r) + 2B_\nu(r)}{r^3} \right] - \tfrac{1}{r} \left[\tfrac{B'_\nu(r) r - B_\nu(r)}{r^2} \right] \right. \\
&\quad \left. + \tfrac{l(l+1)}{2}\tfrac{B_\nu(r)}{r^3} - \tfrac{B_\nu(r)}{r^2} \right] Y_l^m(\Omega) r^2 \mathrm{d}r\mathrm{d}\Omega \\
&= \int_0^{r_{\max}} \int \tfrac{B_\mu(r)}{r} Y_{l'}^{m'}(\Omega) \left[-\tfrac{1}{2}\tfrac{B''_\nu(r)}{r} + \tfrac{l(l+1)}{2}\tfrac{B_\nu(r)}{r^3} - \tfrac{B_\nu(r)}{r^2} \right] Y_l^m(\Omega) r^2 \mathrm{d}r\mathrm{d}\Omega \\
&= \int_0^{r_{\max}} \tfrac{B_\mu(r)}{r} \left[-\tfrac{1}{2}\tfrac{B''_\nu(r)}{r} + \tfrac{l(l+1)}{2}\tfrac{B_\nu(r)}{r^3} - \tfrac{B_\nu(r)}{r^2} \right] \mathrm{d}r \times \int Y_{l'}^{m'}(\Omega) Y_l^m(\Omega)\mathrm{d}\Omega \\
&= \left[-\tfrac{1}{2} \left\langle \mu \left| \tfrac{\partial^2}{\partial r^2} \right| \nu \right\rangle + \tfrac{l(l+1)}{2} \left\langle \mu \left| \tfrac{1}{r^2} \right| \nu \right\rangle - \left\langle \mu \left| \tfrac{1}{r} \right| \nu \right\rangle \right] \; \delta_{l',l} \; \delta_{m',m}.
\end{aligned} \tag{3.58}$$

Electric field matrix elements in the length gauge $(H^L_{\mu,\nu})_{l'l}^{m'm}(t)$:

$$\begin{aligned}
(H^L_{\mu,\nu})_{l'l}^{m'm}(t) &= \int_0^{r_{\max}} \int \tfrac{B_\mu(r)}{r} Y_{l'}^{m'}(\Omega) \left[E(t) r \cos\theta \right] \tfrac{B_\nu(r)}{r} Y_l^m(\Omega) r^2 \mathrm{d}r\mathrm{d}\Omega \\
&= E(t) \int_0^{r_{\max}} B_\mu(r) \; r \; B_\nu(r)\mathrm{d}r \times \int Y_{l'}^{m'}(\Omega) \; [\cos\theta \; Y_l^m(\Omega)]\mathrm{d}\Omega \\
&= E(t)\langle \mu | r | \nu \rangle \times \int Y_{l'}^{m'}(\Omega) \; [a_{l+1,m} Y_{l+1}^m(\Omega) + a_{l-1,m} Y_{l-1}^m(\Omega)]\mathrm{d}\Omega \\
&= E(t)\langle \mu | r | \nu \rangle \{ a_{l+1,m} \int Y_{l'}^{m'}(\Omega) Y_{l+1}^m(\Omega)\mathrm{d}\Omega + a_{l-1,m} \int Y_{l'}^{m'}(\Omega) Y_{l-1}^m(\Omega)\mathrm{d}\Omega \} \\
&= E(t)\langle \mu | r | \nu \rangle \{ a_{l+1,m} \; \delta_{l',l+1}\delta_{m',m} + a_{l-1,m} \; \delta_{l',l-1}\delta_{m',m} \} \\
&= E(t)\langle \mu | r | \nu \rangle \; a_{l+1,m} \; \delta_{l',l+1}\delta_{m',m} + E(t)\langle \mu | r | \nu \rangle \; a_{l-1,m} \; \delta_{l',l-1}\delta_{m',m} \\
&= (H^L_{\mu,\nu})_{l',l+1}^{m'm}(t) + (H^L_{\mu,\nu})_{l',l-1}^{m'm}(t),
\end{aligned} \tag{3.59}$$

where

$$a_{l+1,m} = \left[\frac{(l-m+1)(l+m+1)}{(2l+1)(2l+3)} \right]^{1/2}, \tag{3.60}$$

$$a_{l-1,m} = \left[\frac{(l-m)(l+m)}{(2l+1)(2l-1)} \right]^{1/2}. \tag{3.61}$$

Electric field matrix elements in the velocity gauge $(H^V_{\mu,\nu})^{m',m}_{l',l}(t)$:

$$\begin{aligned}
(H^V_{\mu,\nu})^{m',m}_{l',l}(t) &= \int_0^{r_{\max}}\int \frac{B_\mu(r)}{r} Y^{m'}_{l'}(\Omega)\left\{-iA(t)\left[\cos\theta\frac{\partial}{\partial r}-\frac{\sin\theta}{r}\frac{\partial}{\partial\theta}\right]\right\}\frac{B_\nu(r)}{r}Y^m_l(\Omega)r^2\mathrm{d}r\mathrm{d}\Omega \\
&= -iA(t)\left\{\int_0^{r_{\max}}\int \frac{B_\mu(r)}{r}Y^{m'}_{l'}(\Omega)\left[\cos\theta\frac{\partial}{\partial r}\right]\frac{B_\nu(r)}{r}Y^m_l(\Omega)r^2\mathrm{d}r\mathrm{d}\Omega\right. \\
&\quad \left. -\int_0^{r_{\max}}\int \frac{B_\mu(r)}{r}Y^{m'}_{l'}(\Omega)\left[\frac{\sin\theta}{r}\frac{\partial}{\partial\theta}\right]\frac{B_\nu(r)}{r}Y^m_l(\Omega)r^2\mathrm{d}r\mathrm{d}\Omega\right\} \\
&= -iA(t)\left\{\int_0^{r_{\max}}\frac{B_\mu(r)}{r}\frac{\partial}{\partial r}\left[\frac{B_\nu(r)}{r}\right]r^2\mathrm{d}r\times\int Y^{m'}_{l'}(\Omega)\left[\cos\theta\, Y^m_l(\Omega)\right]\mathrm{d}\Omega\right. \\
&\quad \left. -\int_0^{r_{\max}}\frac{B_\mu(r)B_\nu(r)}{r}\mathrm{d}r\times\int Y^{m'}_{l'}(\Omega)\ \left[\sin\theta\frac{\partial}{\partial\theta}\ Y^m_l(\Omega)\right]\mathrm{d}\Omega\right\} \\
&= -iA(t)\left\{\int_0^{r_{\max}}\frac{B_\mu(r)}{r}\left[\frac{B'_\nu(r)r-B_\nu(r)}{r^2}\right]r^2\mathrm{d}r\right. \\
&\quad \times\int Y^{m'}_{l'}(\Omega)[a_{l+1,m}Y^m_{l+1}(\Omega)+a_{l-1,m}Y^m_{l-1}(\Omega)]\mathrm{d}\Omega \\
&\quad -\int_0^{r_{\max}}\frac{B_\mu(r)B_\nu(r)}{r}\mathrm{d}r \\
&\quad \left.\times\int Y^{m'}_{l'}(\Omega)[l\times a_{l+1,m}Y^m_{l+1}(\Omega)-(l+1)\times a_{l-1,m}Y^m_{l-1}(\Omega)]\mathrm{d}\Omega\right\} \\
&= -iA(t)\left\{\left[\left\langle\mu\left|\frac{\partial}{\partial r}\right|\nu\right\rangle-\langle\mu|\tfrac{1}{r}|\nu\rangle\right]\right. \\
&\quad \times[a_{l+1,m}\int Y^{m'}_{l'}(\Omega)Y^m_{l+1}(\Omega)\mathrm{d}\Omega+a_{l-1,m}\int Y^{m'}_{l'}(\Omega)Y^m_{l-1}(\Omega)\mathrm{d}\Omega] \\
&\quad -\langle\mu|\tfrac{1}{r}|\nu\rangle \\
&\quad \left.\times[l\ a_{l+1,m}\int Y^{m'}_{l'}(\Omega)Y^m_{l+1}(\Omega)\mathrm{d}\Omega-(l+1)\ a_{l-1,m}\int Y^{m'}_{l'}(\Omega)Y^m_{l-1}(\Omega)\mathrm{d}\Omega]\right\} \\
&= -iA(t)\left\{\left[\left\langle\mu\left|\frac{\partial}{\partial r}\right|\nu\right\rangle-\langle\mu|\tfrac{1}{r}|\nu\rangle\right]\times[a_{l+1,m}\ \delta_{l',l+1}\delta_{m',m}+a_{l-1,m}\ \delta_{l',l-1}\delta_{m',m}]\right. \\
&\quad \left.-\ \langle\mu|\tfrac{1}{r}|\nu\rangle\times[l\ a_{l+1,m}\ \delta_{l',l+1}\delta_{m',m}-(l+1)\ a_{l-1,m}\ \delta_{l',l-1}\delta_{m',m}]\right\} \\
&= -iA(t)\left\{\left[\left\langle\mu\left|\frac{\partial}{\partial r}\right|\nu\right\rangle-(l+1)\langle\mu|\tfrac{1}{r}|\nu\rangle\right]\times a_{l+1,m}\ \delta_{l',l+1}\delta_{m',m}\right\} \\
&\quad -iA(t)\left\{\left[\left\langle\mu\left|\frac{\partial}{\partial r}\right|\nu\right\rangle-l\times\langle\mu|\tfrac{1}{r}|\nu\rangle\right]\times a_{l-1,m}\ \delta_{l',l-1}\delta_{m',m}\right\} \\
&= (H^V_{\mu,\nu})^{m',m}_{l',l+1}(t)+(H^V_{\mu,\nu})^{m',m}_{l',l-1}(t),
\end{aligned}$$

where $a_{l+1,m}$ and $a_{l-1,m}$ are given by Eq. (3.60) and Eq. (3.61), respectively.

3.4 N-ELECTRON ATOMS

N-electron atoms present a complex electronic structure. This fact is related to the existence of the electron-electron interactions, which are of the same order of magnitude as the nucleus-electron interactions. Therefore, the electron dynamics is controlled by both interactions. The non-relativistic Hamiltonian for a N-electron atom can be expressed as

$$\hat{H}_0 = -\frac{1}{2}\sum_{i=1}^{N}\nabla^2_{r_i}-\sum_{i=1}^{N}\frac{Z}{r_i}+\sum_{i=1}^{N}\sum_{j>i}^{N}\frac{1}{r_{ij}}, \tag{3.62}$$

where the electron-electron interaction is given by the pairwise Coulomb potential

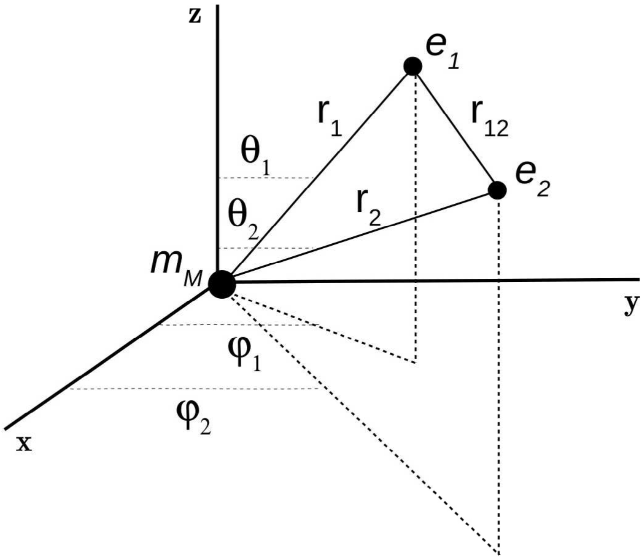

Figure 3.15: A two-electron atom in spherical polar coordinates. The nucleus of mass m_M is located at the center of the system while the relative positions of the electrons m_{e_1} and m_{e_2} are given by $\mathbf{r}_1 \equiv \{r_1, \theta_1, \phi_1\}$ and $\mathbf{r}_2 \equiv \{r_2, \theta_2, \phi_2\}$. The electron-electron distance is determined by the vector $r_{12} = |r_1 - r_2|$.

function,

$$w_{ee}(r_{ij}) = \frac{1}{r_{ij}}, \tag{3.63}$$

with $r_{ij} = |\mathbf{r}_i - \mathbf{r}_j|$ being the distance between the ith and the jth electron. In Figure 3.15, a two-electron atom in spherical harmonics is presented.

Due to the electron-electron interaction term, the Schrödinger equation associated to Eq. (3.62) cannot be solved and approximations must be done. In order to obtain accurate results, different methods have been developed during the last decades. One of the first approximations is the Hartree-Fock approximation [Hartree 57], which expresses the ground state wave function of the system as a single Slater determinant,

$$\Psi_0^{\mathrm{HF}}(\mathbf{x}_1, \mathbf{x}_2, ..., \mathbf{x}_N) = (N!)^{-1/2} \begin{vmatrix} \chi_i(\mathbf{x}_1) & \chi_j(\mathbf{x}_1) & \cdots & \chi_k(\mathbf{x}_1) \\ \chi_i(\mathbf{x}_2) & \chi_j(\mathbf{x}_2) & \cdots & \chi_k(\mathbf{x}_2) \\ \vdots & \vdots & & \vdots \\ \chi_i(\mathbf{x}_N) & \chi_j(\mathbf{x}_N) & \cdots & \chi_k(\mathbf{x}_N) \end{vmatrix}, \tag{3.64}$$

where N electrons occupy N spin-orbitals $\{\chi_i, \chi_j, ..., \chi_k\}$. For the propose of increasing the accuracy of the Hartree-Fock solution, one can introduce high-order terms to the wave function based on excited Slater determinants (also called configurations) [Szabo 96]. In principle, if one takes into account a *full configuration interaction* expansion of the wave function, exact results can be obtained. However, limitations arise from a computational point of view. Nevertheless, within the density functional theory, it is possible to correct some of the errors introduced by the Hartree-Fock approximation at the single determinant level [Koch 01].

A review of the different electronic-structure methods is far from the outlooks of the present section. However, a common point between all these methods is the computation of the two-electron integrals. This task can be seen as a fundamental brick. For this reason, in this section we are going to present in details how two-electron integrals can be computed within a basis of B-splines. We are not only interest on the pure Coulomb integrals, but also on the range-separation integrals, which are normally required in hybrid methods, as we will see later.

The numerical technique presented here to compute the two-electron integrals is based on direct integration. This is a very expensive method from a computational point of view, but is the simplest one. Other ways to obtain the two-electron integrals are based on the Poisson equation, which is a convenient technique when working with molecules, see for example [Becke 88].

3.4.1 Two-electron integrals for the Coulomb interaction

The Coulomb electron-electron interaction is given by

$$w_{ee}(|\mathbf{r}_1-\mathbf{r}_2|)=\frac{1}{\left(|\mathbf{r}_1|^2+|\mathbf{r}_2|^2-2|\mathbf{r}_1||\mathbf{r}_2|\cos\gamma\right)^{1/2}}, \tag{3.65}$$

where $\mathbf{r}_1$ and $\mathbf{r}_2$ are electron vector positions and γ is the angle between them. As it is shown in Appendix B, the multipolar expansion of this interaction is given by

$$w_{ee}(|\mathbf{r}_1-\mathbf{r}_2|)=\sum_{k=0}^{\infty}\left[\frac{r_<^k}{r_>^{k+1}}\right]\sum_{m_k=-k}^{k}(-1)^{m_k}C^k_{-m_k}(\Omega_1)C^k_{m_k}(\Omega_2), \tag{3.66}$$

where $r_< = \min(|\mathbf{r}_1|,|\mathbf{r}_2|)$ and $r_> = \max(|\mathbf{r}_1|,|\mathbf{r}_2|)$ and the renormalized spherical harmonics are defined as

$$C^k_{m_k}(\Omega)\equiv C^k_{m_k}(\theta,\phi)=\left(4\pi/(2k+1)\right)^{1/2}Y_k^{m_k}(\theta,\phi). \tag{3.67}$$

In a one-electron atomic orbital basis, where the spatial orbitals are given by

$$\langle\mathbf{r}|p\rangle\equiv\langle\mathbf{r}|n_p,l_p,m_p\rangle=\varphi_{n_p,l_p,m_p}(\mathbf{r})=\frac{u_{n_p,l_p}(r)}{r}Y_{l_p}^{m_p}(\theta,\phi), \tag{3.68}$$

the Coulomb two-electron integrals can be expressed as the sum of products of radial integrals and angular factors such as

$$\begin{aligned}\langle pq|w_{ee}|tu\rangle &= \sum_{k=0}^{\infty} R^k(p,q;t,u) \sum_{m_k=-k}^{k} \delta_{m_k,m_p-m_t}\delta_{m_k,m_q-m_u} \\ &\times (-1)^{m_k}\, c^k(l_p,m_p,l_t,m_t)\, c^k(l_q,m_q,l_u,m_u), \qquad (3.69)\end{aligned}$$

where the angular coefficients $c^k(l_p,m_p,l_t,m_t)$ and $c^k(l_q,m_q,l_u,m_u)$ are the Gaunt's coefficients, which are defined in details in Appendix B. However, we recall here that, the Gaunt's coefficient $c^k(l,m,l',m')$ is non zero only if $|l-l'| \leq k \leq l+l'$ and if $l+l'+k$ is an even integer, which makes the sum over k exactly terminate.

The two-dimensional radial Slater integrals are given by $R^k(p,q;t,u)$, where the labels p, q, t and u represent the radial functions of the one-electron atomic orbitals, $u_{n_p,l_p}(r_1)$, $u_{n_q,l_q}(r_2)$, $u_{n_t,l_t}(r_1)$ and $u_{n_u,l_u}(r_2)$. Moreover, these radial functions can be approximated using the B-spline representation as we explained before. Thus, for a given knot sequence $\{t_i\}_1^{N_s+k_s}$ on a finite space segment $[0,r_{\max}]$, one has

$$u_{n_p,l_p}(r_1) = \sum_{\alpha=1}^{N_s} c_\alpha^{n_p,l_p} B_\alpha^{k_s}(r_1), \qquad (3.70)$$

$$u_{n_q,l_q}(r_2) = \sum_{\lambda=1}^{N_s} c_\lambda^{n_q,l_q} B_\lambda^{k_s}(r_2), \qquad (3.71)$$

$$u_{n_p,l_t}(r_1) = \sum_{\beta=1}^{N_s} c_\beta^{n_t,l_t} B_\beta^{k_s}(r_1), \qquad (3.72)$$

$$u_{n_p,l_u}(r_2) = \sum_{\nu=1}^{N_s} c_\nu^{n_u,l_u} B_\nu^{k_s}(r_2). \qquad (3.73)$$

Afterwards, if this representation is implemented, the radial Slater integrals $R^k(p,q;t,u)$ are finally given by the following expression

$$R^k(p,q;t,u) = \sum_{\alpha=1}^{N_s}\sum_{\lambda=1}^{N_s}\sum_{\beta=1}^{N_s}\sum_{\nu=1}^{N_s} (c_\alpha^{n_p,l_p})^* (c_\lambda^{n_q,l_q})^* c_\beta^{n_t,l_t} c_\nu^{n_u,l_u}\; R^k(\alpha,\lambda;\beta,\nu), \qquad (3.74)$$

where $R^k(\alpha,\lambda;\beta,\nu)$ are the Slater matrix elements given by the two-dimensional integrals

$$R^k(\alpha,\lambda;\beta,\nu) = \int_0^{r_{\max}}\int_0^{r_{\max}} B_\alpha^{k_s}(r_1) B_\lambda^{k_s}(r_2) \left[\frac{r_<^k}{r_>^{k+1}}\right] B_\beta^{k_s}(r_1) B_\nu^{k_s}(r_2) \mathrm{d}r_1 \mathrm{d}r_2. \qquad (3.75)$$

3.4.1.1 Qiu and Froese Fischer Integration-Cell Algorithm

In order to directly evaluate the Slater matrix elements, defined by Eq. (3.75), one can implement the integration-cell algorithm, which was developed by Qiu *et al.* [Qiu 99], and entirely based on the piecewise nature of B-splines. We recall that, for a given knot sequence $\{t_i\}_1^{N_s+k_s}$, the B-spline $B_\alpha^{k_s}$ is non-zero only in the range $[t_\alpha, t_{\alpha+k_s}]$. This fact implies that only k_s B-splines are non-zero in the interval $T_\alpha = [t_\alpha, t_{\alpha+1}]$. Consequently, the k_s non-zero B-splines in T_α are labeled as follows: $B_\alpha^{k_s}$, $B_{\alpha+1}^{k_s}$,..., $B_{\alpha+k_s-1}^{k_s}$.

This behavior is translated into the computation of the two-dimensional integral $R^k(\alpha,\lambda;\beta,\nu)$. As a consequence, $R^k(\alpha,\lambda;\beta,\nu) = 0$ if either $|\alpha-\beta| \geq k_s$ or $|\lambda-\nu| \geq k_s$. Basically, contributions to this integral only occur when $B_\alpha^{k_s}(r_1)$ and $B_\beta^{k_s}(r_1)$, together with $B_\lambda^{k_s}(r_2)$ and $B_\nu^{k_s}(r_2)$, overlap. In addition, due to the inherent symmetry of $R^k(\alpha,\lambda;\beta,\nu)$, one can compute $R^k(\alpha,\lambda;\beta,\nu) \neq 0$ only for $\alpha \leq \beta$, $\lambda \leq \nu$ and $\alpha \leq \lambda$.

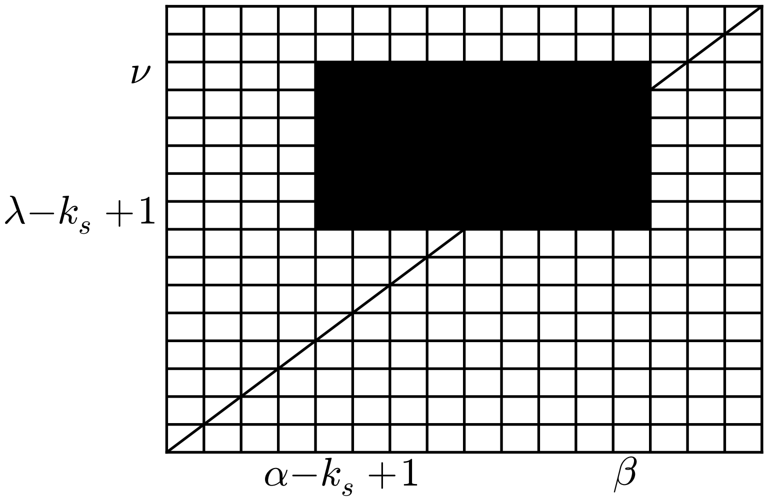

Figure 3.16: Schematic representation of the area over the cells that contribute to the integrand of the Slater matrix elements $R^k(\alpha,\lambda;\beta,\nu)$. The area is composed by a block of cells extended from the interval $T_{\alpha-k_s+1}$ to T_β in the axis r_1, and from the interval $T_{\lambda-k_s+1}$ to T_ν in the axis r_2. Figure inspired from [Qiu 99].

As well as this, it can be shown that, the area which contributes to $R^k(\alpha,\lambda;\beta,\nu)$ is extended from the knot interval $T_{\alpha-k_s+1}$ to the interval T_β in the axis r_1, and from the interval $T_{\lambda-k_s+1}$ to the interval T_ν in the axis r_2 coordinate, see for instance Figure 3.16. Since there are only k_s B-splines which are non-zero along the r_1 or r_2 coordinates in each cell, the integration is performed only with the non-zero $\{\alpha,\beta,\lambda,\nu\}$ combinations over each individual cell, and then, after summation, the Slater matrix elements are obtained. As one observes in Figure 3.16, there are two kinds of integration cells, those located over the off-diagonal elements, and those over the diagonal.

- **Integration over the off-diagonal cells:**

  Over the off-diagonal cells, the integration limits are not coupled and the integrand of $R^k(\alpha,\lambda;\beta,\nu)$ is separable. The two-dimensional integral is then reduced to a product of two one-dimensional integrals. Thus, for a given off-diagonal cell, defined, for example, between the knot intervals $T_\alpha = [t_\alpha, t_{\alpha+1}]$ and $T_\lambda = [t_\lambda, t_{\lambda+1}]$, in the r_1 and r_2 coordinates respectively, and for the case $t_\alpha < t_\lambda$, one has the following product:

$$R^k(\alpha,\lambda;\beta,\nu;T_\alpha,T_\lambda) = r^k(\alpha,\beta;T_\alpha) \times r^{-k-1}(\lambda,\nu;T_\lambda), \tag{3.76}$$

  where

$$\begin{aligned} r^k(\alpha,\beta;T_\alpha) &= \int_{t_\alpha}^{t_{\alpha+1}} B_\alpha^{k_s}(r_1)\, r_1^k\, B_\beta^{k_s}(r_1)\mathrm{d}r_1, & (3.77)\\ r^{-k-1}(\lambda,\nu;T_\lambda) &= \int_{t_\lambda}^{t_{\lambda+1}} B_\lambda^{k_s}(r_2)\, \frac{1}{r_2^{k+1}}\, B_\nu^{k_s}(r_2)\mathrm{d}r_2. & (3.78)\end{aligned}$$

  Eq. (3.77) and Eq. (3.78) can be evaluated using the Gauss-Legendre quadrature, as in the case of the one-electron integrals. Additionally, we remark that, in general, $r^k(\alpha,\beta;T_\alpha) = r^k(\beta,\alpha;T_\alpha)$ and that $r^{-k-1}(\alpha,\beta;T_\alpha) = r^{-k-1}(\beta,\alpha;T_\alpha)$. Then, only elements with $\alpha < \beta$ need to be calculated and stored for a later assembling.

- **Integration over the diagonal cells:**

  Over the diagonal cells, the integration limits are coupled and a two-dimensional integration shall be performed. Then, for a given diagonal cell, $T_\alpha = T_\lambda$, we have the following summation:

$$R^k(\alpha,\lambda;\beta,\nu;T_\alpha) = R^k_\Delta(\alpha,\lambda;\beta,\nu;T_\alpha) + R^k_\Delta(\lambda,\alpha;\nu,\beta;T_\alpha), \tag{3.79}$$

  where in general, a triangle element is given by the two-dimensional integral product

$$R^k_\Delta(\alpha,\lambda;\beta,\nu;T_\alpha) = \int_{t_\alpha}^{t_{\alpha+1}} B_\alpha^{k_s}(r_1)\, \frac{1}{r_1^{k+1}}\, B_\beta^{k_s}(r_1)\mathrm{d}r_1 \int_{t_\alpha}^{r_1} B_\lambda^{k_s}(r_2)\, r_2^k\, B_\nu^{k_s}(r_2)\mathrm{d}r_2. \tag{3.80}$$

Eq. (3.80) is computed again with the Gauss-Legendre quadrature and stored. The complementary triangle element is then obtained from the former, by doing a symmetric index exchange during the later assembling.

- **Assembly of the cell integrals:**

  To sum up, one only needs to compute and to store the cell integrals $r^k(\alpha, \beta; T_\alpha)$, $r^{-k-1}(\alpha, \beta; T_\alpha)$ and $R^k_\Delta(\alpha, \lambda; \beta, \nu; T_\alpha)$, and then, Slater matrix elements are obtained after the assembling of the different cell integrals. The computational cost of the assembling is $N_s^2 \times k_s^4$.

3.4.1.2 Some $F^k[p, q]$ and $G^k[p, q]$ integrals

In order to test our implementation of the integration-cell algorithm, and the accuracy of such a method, we decided to evaluate some of the well known Slater integrals, which are defined for a set of hydrogen orbital functions. We decided to reproduced the same integrals appearing in [Qiu 99].

First of all, the hydrogen radial functions are reproduced within our basis set of B-splines as

$$u_{n_p,l_p}(r) = \sum_{\alpha=1}^{N_s} c_\alpha^{n_p,l_p} B_\alpha^{k_s}(r) \tag{3.81}$$

where the decomposition coefficients are obtained after diagonalization of Eq. (3.18). Then, the target Slater integrals can be calculated as

$$\begin{aligned} F^k[p,q] \equiv R^k(p,q;p,q) &= \int_0^{r_{\max}} \int_0^{r_{\max}} \left|c_\alpha^{n_p,l_p}\right|^2 \left|c_\lambda^{n_q,l_q}\right|^2 R^k(\alpha,\lambda;\alpha,\lambda), \quad (3.82) \\ G^k[p,q] \equiv R^k(p,q;q,p) &= \int_0^{r_{\max}} \int_0^{r_{\max}} \left|c_\alpha^{n_p,l_p}\right|^2 \left|c_\lambda^{n_q,l_q}\right|^2 R^k(\alpha,\lambda;\lambda,\alpha), \quad (3.83) \end{aligned}$$

where the Slater matrix elements $R^k(\alpha, \lambda; \alpha, \lambda)$ and $R^k(\alpha, \lambda; \lambda, \alpha)$ are obtained with the integration-cell algorithm. In Table 3.5, we show the difference between the exact value and our calculated integrals. We observe that the numerical accuracy is obtained.

Table 3.5: Comparison of some $F^k[p,q]$ and $G^k[p,q]$ integrals computed with the integration-cell algorithm. B-spline parameters: knot sequence was chosen to be linear-parabolic, the order $k_s = 8$ and the dimension $N_s = 56$.

F^k/G^k	Computed value	Exact value[a]	Difference
$F^0[1s,1s]$	0.625000000000	5/8	0.178745906965E-13
$F^0[2s,1s]$	0.209876543210	17/81	0.269229083472E-14
$F^0[2s,2s]$	0.150390625000	77/512	0.252575738102E-14
$F^0[2p,1s]$	0.242798353909	59/243	0.671684929898E-14
$F^0[2p,2s]$	0.162109375000	83/512	0.341393580072E-14
$F^0[2p,2p]$	0.181640625000	93/512	0.552335954751E-14
$F^0[4s,4s]$	0.372714996338E-01	19541/524288	0.256253351871E-13
$F^0[4s,4p]$	0.380382537842E-01	19943/524288	0.220309881449E-13
$F^0[4s,4d]$	0.394687652588E-01	20693/524288	0.178190795452E-13
$F^0[4s,4f]$	0.414714813232E-01	21743/524288	0.161329283266E-13
$F^0[4p,4p]$	0.389347076416E-01	20413/524288	0.180411241502E-13
$F^0[4d,4d]$	0.426731109619E-01	22373/524288	0.733441085643E-14
$F^0[4f,4f]$	0.502262115479E-01	26333/524288	0.153349555276E-14
$G^0[2s,1s]$	0.219478737997E-01	16/729	0.156125112838E-14
$G^0[2p,3p]$	0.990904320000E-02	96768/9765625	0.111022302463E-15
$G^0[2p,4p]$	0.316121639091E-02	560/177147	0.778457159845E-15
$G^1[1s,2p]$	0.512117055327E-01	112/2187	0.722338855397E-14
$G^1[2s,2p]$	0.878906250000E-01	45/512	0.147104550763E-14
$G^1[2p,3s]$	0.942243840000E-02	92016/9765625	0.818789480661E-15
$G^1[2p,3d]$	0.373712486400E-01	1824768/48828125	0.217187379192E-14
$G^1[2p,4s]$	0.324150125163E-02	5168/1594323	0.131578775653E-14
$G^1[2p,4d]$	0.119925510703E-01	19120/1594323	0.161329283266E-14
$F^2[4f,4f]$	0.281402042934E-01	103275/3670016	0.193942084614E-14
$G^2[2p,3p]$	0.113246208000E-01	110592/9765625	0.149186218934E-15
$G^2[2p,4p]$	0.400420742848E-02	2128/531441	0.113884596198E-14
$G^2[2p,4f]$	0.300064666946E-02	4784/1594323	0.362557206479E-15
$G^3[2p,3d]$	0.217998950400E-01	1064448/48828125	0.129410371308E-14
$G^3[2p,4d]$	0.737617157878E-02	3920/531441	0.100267016911E-14
$F^4[4f,4f]$	0.188018253871E-01	69003/3670016	0.160982338571E-14
$G^4[2p,4f]$	0.195694348009E-02	1040/531441	0.251534904017E-15
$F^6[4f,4f]$	0.139102935791E-01	7293/524288	0.130277733046E-14

[a] From Ref. [Qiu 99].

3.4.2 Long-range and short-range two-electron integrals

The Coulomb electron-electron interaction, $w_{ee}(r)$, with $r = |\mathbf{r}_1 - \mathbf{r}_2|$, can be split into a short-range $w_{ee}^{\mathrm{sr}}(r)$ and a long-range $w_{ee}^{\mathrm{lr}}(r)$ component, using the appropriate separator function. In the literature, many different separator functions are proposed in order to assure the following relation

$$w_{ee}(r) = w_{ee}^{\mathrm{lr}}(r) + w_{ee}^{\mathrm{sr}}(r). \tag{3.84}$$

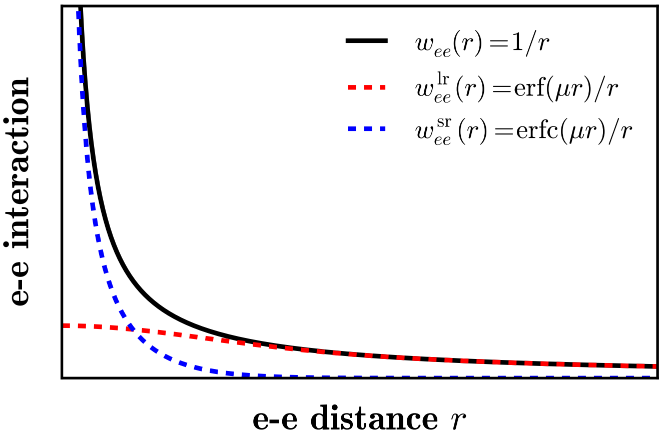

Figure 3.17: Schematic illustration of the Ewald attenuator.

A common separator function is given by the Ewald attenuator, which is based on the error function, such as

$$w_{ee}^{\mathrm{lr}}(r) = \frac{\mathrm{erf}(\mu\, r)}{r}, \tag{3.85}$$

$$w_{ee}^{\mathrm{sr}}(r) = \frac{\mathrm{erfc}(\mu\, r)}{r}, \tag{3.86}$$

where μ is a tunable range-separation parameter controlling the range of the separation. Figure 3.17 presents the splitting of the Coulomb interaction carried out by this separator function.

In order to compute two-electron integrals involving the operators Eq. (3.85) and Eq. (3.86), a multipolar expansion is required as in the Coulomb case, i.e. Eq. (3.66). However, a direct expansion of Eq. (3.85) and Eq. (3.86) is not an immediate task.

It is possible to expand Eq. (3.85) in a Taylor series, such as

$$w_{ee}^{\mathrm{lr}}(r) = \frac{2\mu}{\sqrt{\pi}} \sum_{n=0}^{\infty} \frac{(-\mu)^{2n}}{n!(2n+1)}\, r^{2n}, \tag{3.87}$$

which converges for all r [Gill 97]. Subsequently, the powers of the distance r^{2n} can be expanded as follows

$$r^{2n} = \sum_{k=0}^{\infty} L_{2n}^{k}(r_>, r_<) \sum_{m_k=-k}^{k} (-1)^{m_k} C_{-m_k}^{k}(\Omega_1) C_{m_k}^{k}(\Omega_2), \tag{3.88}$$

where, for $2n$ being an even positive integer, we have [Sack 64]

$$L_{2n}^{k}(r_>, r_<) = (-2n)^k\, r_>^{2n} \left[\frac{r_<}{r_>}\right]^k {}_2F_1\left(k-n, -\frac{1}{2}-n; k+\frac{3}{2}; \frac{r_<^2}{r_>^2}\right), \tag{3.89}$$

where the Gauss hypergeometric function is given by

$$ {}_2F_1(a,b;c;z) = 1 + \sum_{s=1}^{\infty} \frac{(a)_s(b)_s}{(c)_s s!} z^s, \tag{3.90}$$

with

$$\begin{aligned} (a)_0 &= 1, \\ (a)_s &= \frac{\Gamma(a+s)}{\Gamma(a)}. \end{aligned} \tag{3.91}$$

However, when the series Eq. (3.87) is truncated at $n = n_{\max}$, the series behaves as $(-r^2)^{n_{\max}}$ and it becomes worthless at large r. Nevertheless, other expansions have been proposed to overcome the limitations of Eq. (3.87). In the literature, one finds for example the use of methods based on a Gaussian expansion or on a Bessel expansion [Limpanuparb 11]. But, also in these cases, limitations exist. For this reason, attention is focused now on the short-range component, i.e. Eq. (3.86).

3.4.2.1 Exact expression for the short-range interaction

The multipolar expansion of the short-range interaction was derived by Marshall [Marshall 02], but it was Ángyán *et al.* [Ángyán 06] who obtained a compact exact general expression for Eq. (3.86).

First of all, one takes the Laplace transform of Eq. (3.86) in the variable $t = 1/4\mu^2$, such as

$$ w_{ee}^{\mathrm{sr}}(r) = \frac{\mathrm{erfc}(r/2\sqrt{t})}{r}; \quad \mathcal{L}[w_{ee}^{\mathrm{sr}}(r)] = \frac{\exp(r\sqrt{s})}{s\ r}. \tag{3.92}$$

Then, the Gegenbauer addition theorem can be applied to the Laplace transform [Watson 22], and one directly obtains

$$ \frac{\exp(r\sqrt{s})}{s\ r} = \frac{2}{\pi} \sum_{k=0}^{\infty} (2k+1) \frac{i_k(r_<\sqrt{s}) k_k(r_>\sqrt{s})}{\sqrt{s}} \sum_{m_k=-k}^{k} (-1)^{m_k} C_{-m_k}^k(\Omega_1) C_{m_k}^k(\Omega_2), \tag{3.93}$$

where the Bessel functions $i_k(z)$ and $k_k(z)$ are defined as

$$ k_k(z) = \frac{\pi}{2z} e^{-z} \sum_{p=0}^{k} \frac{(k+p)!}{p!(k-p)!(2z)^p} \tag{3.94}$$

$$i_k(z) = \frac{1}{2z}\left(e^z\sum_{p=0}^{k}\frac{(-1)^p(k+p)!}{p!(k-p)!(2z)^p} + (-1)^{k+1}e^{-z}\sum_{p=0}^{k}\frac{(k+p)!}{p!(k-p)!(2z)^p}\right). \tag{3.95}$$

Thus, the multipolar expansion of Eq. (3.86) can be written as

$$w_{ee}^{\text{sr}}(r) = \sum_{k=0}^{\infty} S^k(r_>, r_<; t) \sum_{m_k=-k}^{k} (-1)^{m_k} C^k_{-m_k}(\Omega_1) C^k_{m_k}(\Omega_2), \tag{3.96}$$

where

$$S^k(r_>, r_<; t) = \frac{2(2k+1)}{\pi}\mathcal{L}^{-1}\left[\frac{i_k(r_<\sqrt{s})k_k(r_>\sqrt{s})}{\sqrt{s}}\right]. \tag{3.97}$$

Moreover, Ángyán *et al.* determined a general expression for Eq. (3.97) by performing an order by order determination of the inverse Laplace transform [Ángyán 06]. They found that the radial μ-dependent function, $S^k(r_>, r_<; \mu)$, can be written in terms of the scaled radial coordinates $\eta = \mu\, r_>$ and $\zeta = \mu\, r_<$, as follows

$$S^k(r_>, r_<; \mu) = \mu\; \Phi^k(\eta, \zeta), \tag{3.98}$$

with

$$\Phi^k(\eta,\zeta) = H^k(\eta,\zeta) + F^k(\eta,\zeta) + \sum_{m=1}^{k} F^{k-m}(\eta,\zeta)\frac{\eta^{2m}+\zeta^{2m}}{(\zeta\;\eta)^m}, \tag{3.99}$$

and the introduced auxiliary functions

$$H^k(\eta,\zeta) = \frac{1}{2(\zeta\;\eta)^{k+1}}\left[\left(\eta^{2k+1}+\zeta^{2k+1}\right)\operatorname{erfc}(\eta+\zeta) - \left(\eta^{2k+1}-\zeta^{2k+1}\right)\operatorname{erfc}(\eta-\zeta)\right], \tag{3.100}$$

and

$$F^k(\eta,\zeta) = \frac{2}{\pi^{1/2}}\sum_{p=0}^{k}\left(-\frac{1}{4(\zeta\;\eta)}\right)^{p+1}\frac{(k+p)!}{p!(k-p)!} \times \left[(-1)^{k-p}e^{-(\eta+\zeta)^2} - e^{-(\eta-\zeta)^2}\right]. \tag{3.101}$$

Finally, the associated short-range two-electron integrals $\langle pq|w_{ee}^{\text{sr}}|tu\rangle$ can be determined identical to the Coulomb integrals, Eq. (3.69), with the simple difference that the radial term is not given by the standard Slater matrix elements. Now, the radial kernel in Eq. (3.75) is changed to that of Eq. (3.98). In addition, due to the fact that the radial kernel $S^k(r_>, r_<; \mu)$ is not separable in simple products of the variables $r_>$ and $r_<$, the integration-cell algorithm is modified in order to calculate all integrals as non-separable two-dimensional integrals, as in the case of the off diagonal cells for the Coulomb interaction. In a second step, the long-range two-electron integrals can be simply obtained by difference

$$\langle pq|w_{ee}^{\mathrm{lr}}|tu\rangle = \langle pq|w_{ee}|tu\rangle - \langle pq|w_{ee}^{\mathrm{sr}}|tu\rangle. \tag{3.102}$$

3.4.2.2 Power series expansion of the short-range interaction

The derived expression for the kth-order radial function, $S^k(r_>, r_<; \mu) = \mu\, \Phi^k(\eta, \zeta)$, gives us the possibility to work with the multipolar expansion of the short-range interaction. Nevertheless, it is not separable in the variables $r_>$ and $r_<$. In order to arrive at a separable radial expression in η and ζ, Ángyán *et al.* also introduced a power series expansion of the radial function $\Phi^k(\eta, \zeta)$ in the smaller reduced variable ζ [Ángyán 06]. In this section we explore the validity of this expansion, which is given by

$$\Phi^k(\eta, \zeta) = \sum_{n=0}^{\infty} \frac{D_n^k(\eta)}{\eta^{k+1}} \zeta^{k+2n}, \tag{3.103}$$

where $D_n^k(\eta)$ is given by

$$D_0^0(\eta) = \mathrm{erfc}(\eta), \tag{3.104}$$

for $n = k = 0$,

$$D_0^k(\eta) = \mathrm{erfc}(\eta) + \frac{e^{-(\eta)^2}}{\sqrt{\pi}} 2^{k+1} \sum_{m=1}^{k} \frac{2^{-m}(\mu r_>)^{-2m+2k+1}}{(2k-2m+1)!!}, \tag{3.105}$$

for $n = 0$ and $k \geq 1$, and

$$D_n^k(\eta) = \frac{e^{-(\eta)^2}}{\sqrt{\pi}} \frac{2^{k+1}(2k+1)}{n!(2n+2k+1)} \sum_{m=1}^{n} \binom{m-n-1}{m-1} \frac{2^{n-m}(\eta)^{2n-2m+2k+1}}{(2k+2n-2m+1)!!}, \tag{3.106}$$

for $n \geq 1$ and $k \geq 1$. Figure 3.18 presents the expansion function $D_n^k(\eta)$ for different k and n values. Note that, although higher order terms are almost invisible for the chosen scale, their contribution is non-negligible once they are multiplied by ζ^{k+2n}.

In order to explore the range of validity of Eq. (3.103), one can follow the approach proposed by Ángyán *et al.* [Ángyán 06]. The exact function $\Phi^k(\eta, \zeta)$ is compared with the truncated function $\tilde{\Phi}^k_{n_{\max}}(\eta, \zeta)$, which is defined as

$$\tilde{\Phi}^k_{n_{\max}}(\eta, \zeta) = \sum_{n=0}^{n_{\max}} \frac{D_n^k(\eta)}{\eta^{k+1}} \zeta^{k+2n}. \tag{3.107}$$

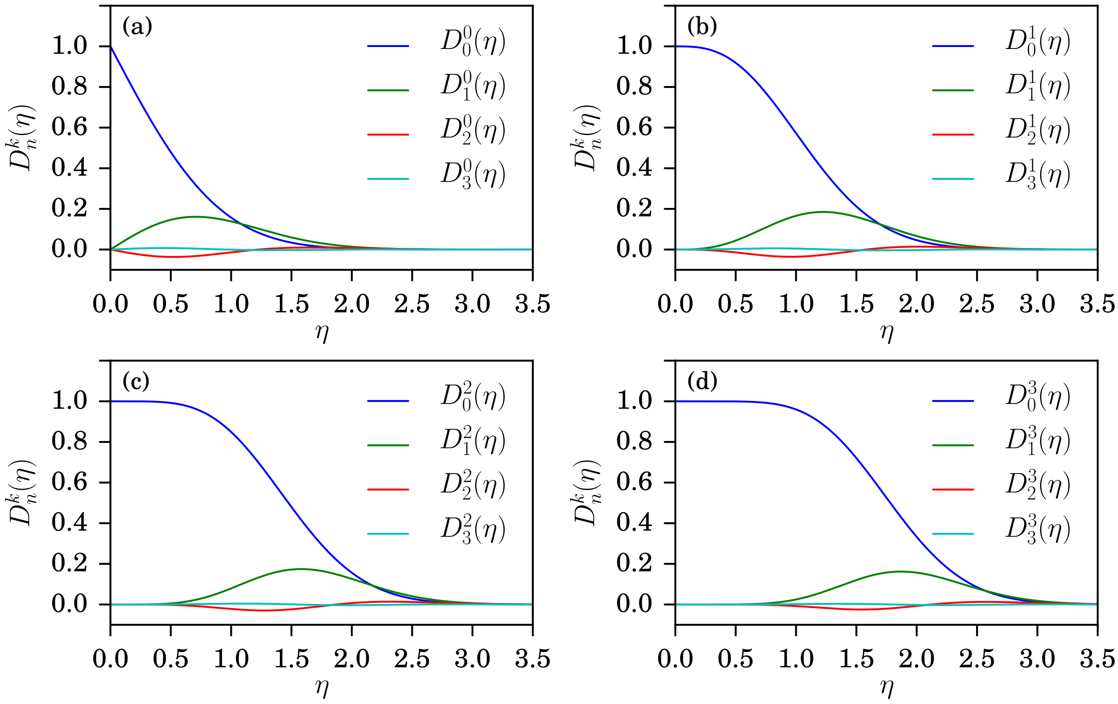

Figure 3.18: Radial expansion function of different orders, $D_n^0(\eta)$,$D_n^1(\eta)$, $D_n^2(\eta)$ and $D_n^3(\eta)$. Figure inspired from [Ángyán 06].

The range of validity for the truncated series expansion Eq. (3.107) is estimated, for different orders, comparing the plots of $\Phi^k(\zeta,\zeta)$ and $\tilde{\Phi}^k_{n_{\max}}(\zeta,\zeta)$, together with the Coulomb interaction kernel $\mathcal{G}^k(\zeta,\zeta)$, which is defined from the following relations

$$\mathcal{G}^k(r_>, r_<) = \left[\frac{r_<^k}{r_>^{k+1}}\right] = \mathcal{G}^k(r_>, r_<) = \mu\, \mathcal{G}^k(\eta,\zeta). \tag{3.108}$$

In Figure 3.19 the radial functions $\mathcal{G}^k(\zeta,\zeta)$, $\Phi^k(\zeta,\zeta)$ and $\tilde{\Phi}^k_{n_{\max}}(\zeta,\zeta)$ are presented for different k values. One observes that, at higher orders of k and at small values of ζ, $\Phi^k(\zeta,\zeta)$ is almost identical to the Coulomb interaction. If attention is focused on the truncated short-range radial function $\tilde{\Phi}^k_{n_{\max}}(\zeta,\zeta)$, one observes that, for $n_{\max} = 0$, it goes to zero too quickly, and for higher k and $n_{\max} > 0$, oscillations appear making the truncated expansion unusable. As a matter of fact, these divergences show us that the truncated expansion in ζ, i.e. Eq. (3.103), shall not be used in the computation of short-range two-electron integrals. Therefore, the implementation of the exact expression Eq. (3.98) was chosen for the calculation of the short-range two-electron integrals.

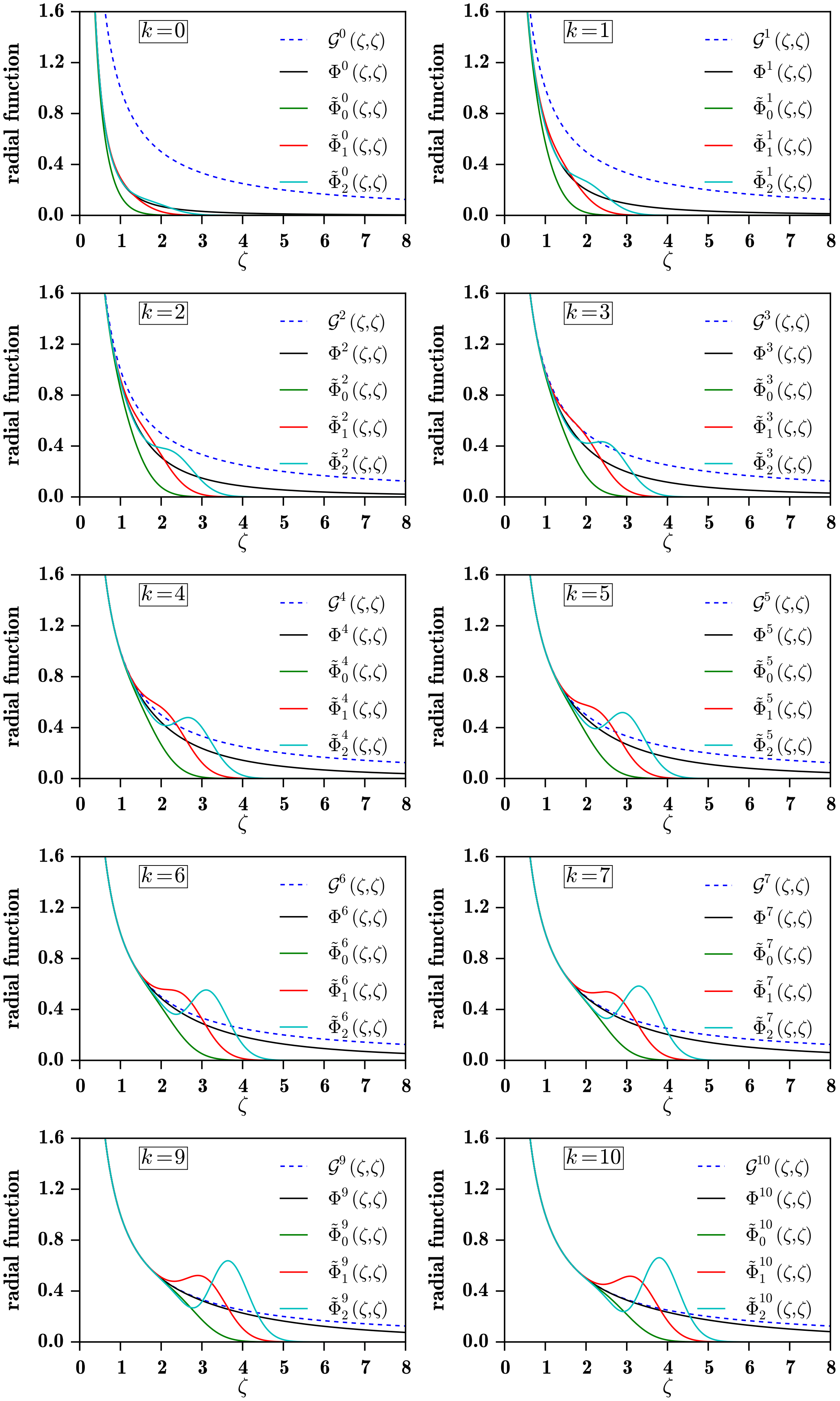

Figure 3.19: Exploration of the range of validity of the truncated short-range expansion $\tilde{\Phi}^k_{n_{\max}}(\eta,\zeta)$. Diagonal values of $\tilde{\Phi}^k_{n_{\max}}(\eta,\zeta)$, $\Phi^k(\eta,\zeta)$ and $\mathcal{G}^k(\eta,\zeta)$, i.e. $\eta=\zeta$.

3.5 MOLECULES

In previous sections attention has been focused on the use of B-splines in atomic calculations. Now, the computation of molecular electronic structures is addressed. Due to the complexity of such systems, we have decided to make use of two commercial quantum chemistry packages, i.e. *Molpro* [Werner 15] and *Qchem* [Shao 15]. These codes have been optimally developed to carry out molecular calculations at different levels of theory. In addition, they are based on Gaussian-type orbital (GTO) functions, see for example [Boys 50, Pople 78]. For this reason, a brief review on GTO functions is given in this section. Moreover, we introduce the use of Kaufmann GTO functions and *"ghost atoms"*. In a second step, we present the TDCIS framework proposed by Luppi *et al.* [Luppi 13] to investigate multiphoton ionization processes in molecules. Finally, at the end of this section, some calculations on the molecular hydrogen ion H_2^+ are shown. In particular, the basis set effects on the energy spectrum and in high-harmonic generation are noted.

Let us now introduce the total field-free Hamiltonian for a N-electron molecule, which is expressed, as we know, in terms of nuclear and electronic position vectors, $\mathbf{R}_A$ and $\mathbf{r}_i$, as follows (in atomic units)

$$\hat{H}_{\text{total}} = -\sum_{i=1}^{N}\frac{1}{2}\nabla_i^2 - \sum_{A=1}^{M}\frac{1}{2M_A}\nabla_A^2 - \sum_{i=1}^{N}\sum_{A=1}^{M}\frac{Z_A}{r_{iA}} + \sum_{i=1}^{N}\sum_{j>i}^{N}\frac{1}{r_{ij}} + \sum_{A=1}^{M}\sum_{B>A}^{M}\frac{Z_A Z_B}{R_{AB}}, \tag{3.109}$$

where Z_A is the atomic number of the nucleus A, and M_A is the mass of the nucleus A. The interatomic distance between two nuclei is given by $R_{AB} = |\mathbf{R}_A - \mathbf{R}_B|$ and the distance between the ith electron and the Ath nucleus is $r_{iA} = |\mathbf{r}_i - \mathbf{R}_A|$. As usual, the distance between two electrons is given by $r_{ij} = |\mathbf{r}_i - \mathbf{r}_j|$.

Here we are interested on electron dynamics, so the Born-Oppenheimer approximation is assumed. As a consequence, the total wave function can be rewritten as a product of two functions such as

$$\Phi_{\text{total}}(\{\mathbf{r}_i\};\{\mathbf{R}_A\}) = \Phi_{\text{elec}}(\{\mathbf{r}_i\};\{\mathbf{R}_A\}) \times \Phi_{\text{nucl}}(\{\mathbf{R}_A\}), \tag{3.110}$$

where the pure electronic wave function $\Phi_{\text{elec}}(\{\mathbf{r}_i\};\{\mathbf{R}_A\})$ depends parametrically on the nuclear coordinates and satisfies the following equation

$$\hat{H}^0_{\text{elec}}\Phi_{\text{elec}} = E_{\text{elec}}\Phi_{\text{elec}}, \tag{3.111}$$

where the field-free electronic Hamiltonian is given by

$$\hat{H}^0_{\text{elec}} = -\sum_{i=1}^{N}\frac{1}{2}\nabla_i^2 - \sum_{i=1}^{N}\sum_{A=1}^{M}\frac{Z_A}{r_{iA}} + \sum_{i=1}^{N}\sum_{j>i}^{N}\frac{1}{r_{ij}}. \tag{3.112}$$

For fixed nuclei, the total molecular energy is defined by adding the nuclear repulsion energy to the electronic energy as follows,

$$E_{\text{total}} = E_{\text{elec}} + \sum_{A=1}^{M}\sum_{B>A}^{M}\frac{Z_A Z_B}{R_{AB}}. \tag{3.113}$$

In general, the ground state of the molecule can be described by the Hartree-Fock determinant $|\Psi_0^{\text{HF}}\rangle = |\chi_1\chi_2...\chi_a\chi_b...\chi_N\rangle$, where the spin-orbitals $\{\chi_i\}$ are obtained after solving the Hartree-Fock-Roothaam equations. If the total number of spin-orbitals is $2O > N$, it is then possible to generate an ensemble of $(2O)!/N!(2O-N)!$ excited configurations using the Hartree-Fock ground state as a reference. Then, the molecular wave function can be represented as

$$|\Phi_{\text{elec}}\rangle = c_0|\Psi_0^{\text{HF}}\rangle + \sum_{ra} c_a^r|\Psi_a^r\rangle + \sum_{\substack{a<b\\ r<s}} c_{ab}^{rs}|\Psi_{ab}^{rs}\rangle + ..., \tag{3.114}$$

where the singly excited configurations $\{|\Psi_a^r\rangle\}$ are Slater determinants in which an electron has been promoted from an occupied spin-orbital χ_a to a virtual one χ_r, i.e. $|\Psi_a^r\rangle = |\chi_1\chi_2...\chi_r\chi_b...\chi_N\rangle$. Subsequently, a doubly excited configuration $|\Psi_{ab}^{rs}\rangle$ implies the promotion of two electrons from occupied spin-orbitals χ_a and χ_b to the virtual χ_r and χ_s. The same holds for higher order excited configurations.

However, the use of a full configuration interaction expansion of the wave function is not possible for a computational point of view, and approximations must be done. In the last years, quantum chemistry codes have been developed within different levels of theory making use of the mathematical properties of the GTO functions. Once we are able to compute the electronic structure of an investigated molecule, it is possible to used the "outputs" of such a calculation and performing a time-dependent propagation in presence of a laser field. This is the framework developed by Luppi *et al.* [Luppi 13] and used during my PhD in order to explore multiphoton processes in molecules. Before describing the propagation method, let us introduce the GTO functions.

3.5.1 Gaussian-type orbitals

In order to solve the molecular Hartree-Fock equation, quantum chemistry packages usually represent the molecular spin-orbitals within a basis set of GTO functions, such as

$$\chi_m(\mathbf{r}) = \sum_{\mu} c_{\mu}^{m}\, G_{\mu}(\mathbf{r}), \tag{3.115}$$

where the GTO function centered on the nucleus A is defined in cartesian coordinates as

$$G_{\mu}(\mathbf{r}) = N_{\mu}\, x_A^{i_\mu}\, y_A^{j_\mu}\, z_A^{k_\mu}\, e^{-\alpha_\mu\, |\mathbf{r}_A|^2}, \tag{3.116}$$

where N_μ is the normalization factor, $\mathbf{r}_A = \mathbf{r} - \mathbf{R}_A$ and the total angular momentum l is given by the sum $i_\mu + j_\mu + k_\mu = l$.

In the context of single and multiphoton processes, the main problems reported when using GTO functions are related to their local nature. Due to this issue, GTO functions are incapable to accurately reproduce Rydberg and continuum states. For the purposes of increasing the performance of GTO basis sets, it is possible to add Kaufmann's functions to the basis [Kaufmann 89]. Kaufmann *et al.* proposed a universal Gaussian basis set for describing Rydberg and continuum states using the appropriate exponents α_μ. In their work, Kaufmann *et al.* presented a systematic procedure to obtain such optimal exponents [Kaufmann 89]. Moreover, GTO functions are normally defined over nuclei in molecules. However, it is also possible to define a GTO function over other space region. When these regions do not contain any nucleus they are denominated as *"ghost atoms"*. This term refers to the absent of nuclei in the region where a set of GTO functions can be defined. The GTO functions defined over a ghost atom are given by Eq. (3.116) but where $\mathbf{r}_A$ is substituted by $\mathbf{r}_{\mathrm{Gh}} = \mathbf{r} - \mathbf{R}_{\mathrm{Gh}}$, where $\mathbf{R}_{\mathrm{Gh}}$ is the position vector of the ghost atom.

The influences of the Kaufmann GTO functions and of ghost atoms have been reported in the calculation of multiphoton processes in atoms and molecules, see for example [Luppi 13, Coccia 16a, Coccia 16b]. As well as this, more informations on

GTO functions can be found in the book *"Molecular Electronic Structure Theory* written by T. Helgaker, P. Jorgensen, and J. Olsen [Helgaker 00].

3.5.2 Time-dependent configuration interaction singles theory

Within the dipole approximation, the TDSE for a N-electron molecule can be written in the length gauge in atomic units as follows

$$i\frac{\mathrm{d}}{\mathrm{d}t}\Phi_{\mathrm{elec}}(t) = \left[\hat{H}^0_{\mathrm{elec}} + \mathcal{E}(t)\cdot\mathbf{R}\right]\Phi_{\mathrm{elec}}(t), \tag{3.117}$$

where the field-free Hamiltonian $\hat{H}^0_{\mathrm{elec}}$ is given by Eq. (3.112) and the total position operator is $\mathbf{R} = \sum_{i=1}^{N}\mathbf{r}_i$, and the electric field $\mathcal{E}(t)$ is normally given by

$$\mathcal{E}(t) = \mathcal{E}_0\,\hat{\mathbf{e}}\,\cos^2\left(\frac{\pi t}{\tau}\right)\cos(\omega t + \phi), \tag{3.118}$$

where τ is the duration of the pulse.

The time-dependent configuration interaction singles (TDCIS) method proposes us to expand the time-dependent wave function $|\Phi_{\mathrm{elec}}(t)\rangle$ onto the time-independent singly excited configurations $\{|\Psi_a^r\rangle\}$, here refered to us as $\{|\Psi_S\rangle\}$,

$$|\Phi_{\mathrm{elec}}(t)\rangle = \sum_{S=0}^{W} c_S(t)|\Psi_S\rangle, \tag{3.119}$$

where W is the total number of excited configurations and $S = 0$ represents the Hartree-Fock configuration. Note that the expansion coefficients take into account the time dependence of the wave function. Afterwards, inserting Eq. (3.119) into Eq. (3.117), and projecting over the corresponding bras, a time-dependent equation for the expansion coefficients is obtained. In a compact matrix form it is given by

$$i\,\frac{\mathrm{d}}{\mathrm{d}t}\mathbf{C}(t) = \left[\mathbf{H}^0 + \mathbf{V}(t)\right]\mathbf{C}(t), \tag{3.120}$$

where $\mathbf{C}(t)$ is the vector matrix for the time-dependent coefficients, $\mathbf{H}^0$ is the field-free diagonal matrix of elements $\mathbf{H}^0_{S,S'} = \langle\Psi_S|\hat{H}^0_{\mathrm{elec}}|\Psi_{S'}\rangle = E_{S'}\delta_{S,S'}$ (where $E_{S'}$ is the energy of the eigenstate S'), and $\mathbf{V}(t)$ is the non-diagonal interaction matrix of elements $\mathbf{V}_{S,S'}(t) = \langle\Psi_S|\mathcal{E}(t)\cdot\mathbf{R}|\Psi_{S'}\rangle$.

In order to solve Eq. (3.120), one commonly chooses the Hartree-Fock ground state as initial condition, i.e. $|\Phi_{\mathrm{elec}}(t=0)\rangle \equiv |\Psi_0^{\mathrm{HF}}\rangle$. Then, time is discretized and the split-propagator approximation technique can be used to separate the contributions from the field-free Hamiltonian and the time-dependent interaction [Press 07]. As a consequence, Eq. (3.120) is translated into the following expression

$$\mathbf{C}(t+\Delta t) \approx e^{-i\,\mathbf{V}(t)\,\Delta t}\, e^{-i\,\mathbf{H}^0\,\Delta t}\,\mathbf{C}(t), \tag{3.121}$$

where Δt is the time step. As the field-free matrix $\mathbf{H}^0$ is diagonal, $e^{-i\,\mathbf{H}^0\,\Delta t}$ is also a diagonal matrix of elements $e^{-i\,E_{S'}\,\Delta t}\,\delta_{S,S'}$. Moreover, the exponential of the non-diagonal interaction matrix can be computed as follows

$$e^{-i\,\mathbf{V}(t)\,\Delta t} = \mathbf{U}^{\dagger}\, e^{-i\,\mathbf{V_d}(t)\,\Delta t}\,\mathbf{U}, \tag{3.122}$$

where $\mathbf{U}$ is a unitary matrix that transforms the interaction representation from the CIS basis into a basis in which it is diagonal, i.e. $\mathbf{V}(t) = \mathbf{U}^{\dagger}\,\mathbf{V_d}(t)\,\mathbf{U} = \mathcal{E}(t)\,\mathbf{U}^{\dagger}\,\mathbf{R_d}\,\mathbf{U}$ where $\mathbf{V_d}(t) = \mathcal{E}(t)\cdot\mathbf{R_d}$ is the diagonal representation of the interaction matrix and $\mathbf{R_d}$ is the diagonal representation of the total position operator. As one can see, the time dependence is factorized in a multiplicative function independent of $\mathbf{R_d}$. As a consequence, the unitary matrix $\mathbf{U}$ is time-independent, allowing us to compute $\mathbf{U}$ only once before the time propagation.

An important aspect to take into account during the propagation is the control of the ionization. During the time propagation, one shall eliminate any unphysical reflexions[4] from the time-dependent wave function. To do this, one used to remove the high-energy electron density from the calculation. This can be done, for example, using the heuristic lifetime model proposed by Klinkusch *et al.* [Klinkusch 09]. Within this heuristic model, the CIS state energies above the ionization threshold are replaced by complex energies such as

$$E_S \to E_S - \frac{i}{2}\Gamma_S, \tag{3.123}$$

where Γ_S is the ionization rate of the single-excited configuration $|\Psi_S\rangle$. In addition, the lifetime t_S of the state S is defined as $t_S = 1/\Gamma_S$. In general, the ionization rate Γ_S is parametrized using a classical picture of the ionization process. Basically, one considers that an electron, placed on a spin-orbital χ_a with an energy $\varepsilon_a >$

---

[4] Unphysical reflexions are errors introduced to the time-dependent wave function during the propagation as a consequence of the incompleteness of the CIS space on which the time-dependent wave function has been represented, and also, due to the limitations of the implemented GTO basis.

0, can be associated with an escaping electron with a kinetic energy of $\varepsilon_a = \frac{1}{2}v^2$, where the escape velocity is given by $v = d/t_S$. The escape length d represents the traveled distance by the electron during the time t_S. The escape length is the single parameter that has to be introduced by the user into the model. Usually, the escape length d is chosen to be identical to the maximal distance gained by an electron in an electromagnetic field within the classical picture of the three-step model, i.e. $d = 2\ \mathcal{E}_0/\omega^2$, where $\mathcal{E}_0$ is the amplitude of the electric field and ω is the carrier frequency. Finally, this heuristic model is proposed as an alternative to the complex absorbing potentials or to the wave function absorbers [Risoud 17].

Once the time-dependent coefficients are known, the induced dipole-moment can be calculated in the length gauge as follows

$$D(t) = -\langle\Phi(t)|\mathbf{R}|\Phi(t)\rangle = -\sum_{S,S'} c_S^*(t)\, c_{S'}(t)\, R_{S,S'}, \tag{3.124}$$

where $R_{S,S'} = \langle\Psi_S|\mathbf{R}|\Psi_{S'}\rangle$ is the total position matrix element. Consequently, a molecular high-harmonic generation spectrum can be obtained from the square root of the Fourier transform of Eq. (3.124) as

$$P(\omega) = \left|\int_0^{\tau} D(t)h(t)e^{i\omega t}\mathrm{d}t\right|^2, \tag{3.125}$$

where $h(t)$ is an apodization function that can be chosen to be, for example, of the sin-square window form.

3.5.3 Exploring the accuracy of the GTO basis

In order to show the range of validity of GTO functions, we present here an study on the molecular hydrogen ion H_2^+. In addition we investigate the basis set effects on high-harmonic spectra calculated using the TDCIS method previously introduced. This project was carried out in the context of an international collaboration I did during my PhD with E. Coccia at the Dipartimento di Scienze Chimiche in Padova and at the Dipartimento di Scienze Chimiche e Farmaceutiche in Trieste.

For the purposes of representing the field-free Hamiltonian of the H_2^+ molecule, we decided to implement over each hydrogen atom of the molecule a 6-aug-cc-pVTZ+5K atom-centered basis, where “5K” symbolized the used of 5 Kaufmann GTO functions for each angular momentum. In Table 3.6, the implemented Kaufmann exponents are

Table 3.6: Kaufmann exponents for each angular momentum. Here n is not the principal quantum number, n represents the GTO Kaufmann exponent index. In our 6-aug-cc-pVTZ+5K basis, 5 Kaufmann functions have been included for each angular momentum up to $l = 2$.

n	$l = 0$	$l = 1$	$l = 2$
1	0.245645	0.430082	0.622557
2	0.098496	0.169341	0.242160
3	0.052725	0.089894	0.127840
4	0.032775	0.055611	0.078835
5	0.022327	0.037766	0.053428

given. The total number of GTO functions presented in our GTO basis was 226.

Within the 6-aug-cc-pVTZ+5K basis, it is possible to solve the Hartree-Fock equation in order to obtain an ensemble of molecular orbitals with the code *Qchem* [Shao 15]. In order to eliminate possible linear dependencies problems, during the diagonalization of the Hartree-Fock Hamiltonian, 25 GTO functions were removed automatically from the basis by *Qchem*. Linear dependencies are numerical errors arising due to the high degree of overlap between the GTO functions.

After the diagonalization of the Hartree-Fock Hamiltonian, the CIS matrix can be built up with the calculated Hartree-Fock molecular orbitals. The diagonalization of the CIS matrix gives us an ensemble of excited states. For the case of the molecular hydrogen ion H_2^+ these excited states correspond to the exact ones.

3.5.3.1 Potential energy curves

In Figure 3.20, some of the lowest potential energy curves are shown for some of the lowest excited states. One can observe that their behavior is correct and in concordance with the curves given by Fetic *et al.* [Fetic 17]. Additionally, Table 3.7 presents some electronic eigenvalues for the first states of symmetry σ and π. Our results are directly compared with the accurate calculations carried out by Fetic *et al.* [Fetic 17]. They implemented a basis set of B-splines in elliptical coordinates (ξ, η, φ), where the box size was chosen to be $\xi_{\max} = 60$ au, the total number of B-splines (of order 10) was 80 and the number of spherical harmonics was 20. This comparison gives us a measure of the accuracy of the *Qchem* calculation with the 6-aug-cc-pVTZ+5K basis.

In Table 3.7 we observe that the difference between energies (expressed in terms of $10^{-\delta}$) is more important in the ground state that in higher energy states. In order

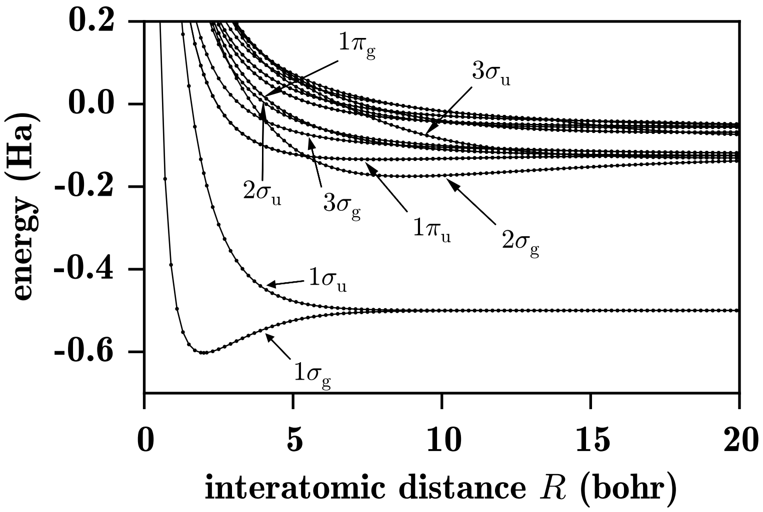

Figure 3.20: Some potential energy curves of the molecular hydrogen ion H_2^+ for the first lowest bound states calculated with a 6-aug-cc-pVTZ+5K basis with the code *Qchem*.

to clarify this fact, one could do two things: first, comparing the *Qchem* energies with an exact (analytical) calculation of H_2^+, and second, performing a systematic study on different GTO basis. For example, by changing the angular momentum of the GTO functions, the number of diffuse functions in the basis or by including a different number of Kaufmann functions.

These proposed explorations are beyond the principal aim of the present manuscript and are postponed to a future work. Nevertheless, we can say that the bound state energies, computed with the 6-aug-cc-pVTZ+5K basis, are quite accurate.

Table 3.7: Comparison of some electronic eigenvalues (in Ha) of the hydrogen molecular ion H_2^+ at the equilibrium interatomic distance calculated with a 6-aug-cc-pVTZ+5K basis with the code *Qchem*. The error difference is given in terms of $10^{-\delta}$.

State	Eigenvalue	Eigenvalue[a]	δ
$1\sigma_g$	-1.1024194974	-1.1026342145	4
$1\sigma_u$	-0.6673174571	-0.6675343922	4
$1\pi_u$	-0.4287137515	-0.4287718199	5
$2\sigma_g$	-0.3607918005	-0.3608648753	5
$2\sigma_u$	-0.2553534735	-0.2554131651	5
$1\pi_g$	-0.2266921320	-0.2266996266	6

[a] From Ref. [Fetic 17].

3.5.3.2 Energy spectrum

Attention is now focused on Rydberg and continuum states. In order to increase the density of these states, we decided to add a set of ghost atoms to our 6-aug-cc-

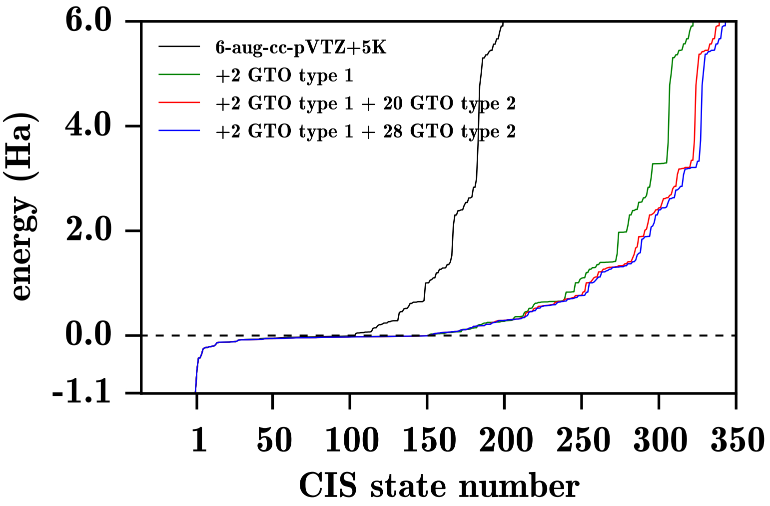

Figure 3.21: Energy spectrum of the molecular hydrogen ion H_2^+ computed at the interatomic equilibrium distance. In black: calculation with the 6-aug-cc-pVTZ+5K basis over each hydrogen atom. In green: calculation with the 6-aug-cc-pVTZ+5K basis plus the addition of two basis *GTO type 1* over ghost atoms (see text). In red: calculation with the 6-aug-cc-pVTZ+5K basis plus the addition of two basis *GTO type 1* over two ghost atoms and 20 functions *GTO type 2* over 20 ghost atoms (see text). In blue: calculation with the 6-aug-cc-pVTZ+5K basis plus the addition of two basis *GTO type 1* over two ghost atoms and 28 functions *GTO type 2* over 28 ghost atoms (see text).

pVTZ+5K basis. The addition of ghost atoms may suppose the inclusion of linear dependencies in the calculation. For this reason, the position of ghost atoms has to be chosen carefully. Furthermore, the type of GTO functions placed over the ghost atoms have also to be tested.

In our study, attention was focused only in ghost atoms distributed along the molecular axis (z-axis). Moreover, after different tests, two types of GTO basis functions where placed over the ghost atoms:

- **GTO type 1:** This GTO basis is composed by Kaufmann and diffuse GTO functions with angular momentum $l = 1$ and $l = 2$. We have used 5 Kaufmann and 4 diffuse GTO functions for each value of l. This basis set was placed over two ghost atoms located at $\mathbf{R}_{\mathrm{Gh}_1} = 9.448\ \hat{\boldsymbol{k}}$ au and at $\mathbf{R}_{\mathrm{Gh}_2} = -9.448\ \hat{\boldsymbol{k}}$ au, where $\hat{\boldsymbol{k}}$ is the unitary vector of the direction. The center of the molecule is placed at $\mathbf{R}_{\mathrm{CM}} = 0\ \hat{\boldsymbol{k}}$.

- **GTO type 2:** This GTO basis is simply composed by a single Kaufmann GTO function of angular momentum $l = 0$ where the exponent is $\alpha_1 = 0.245645$. An ensemble of this GTO function has been distributed over the z-axis with an spacing of 0.9488 au between each function. In the positive range of the z-axis, the first *GTO type 2* function was placed at $\mathbf{R}_{\mathrm{Gh}_1} = (9.448 + 0.9448)\,\hat{\boldsymbol{k}}$, and, in the negative range, at $\mathbf{R}_{\mathrm{Gh}_2} = -(9.448+0.9448)\,\hat{\boldsymbol{k}}$. In our calculation, the same number of *GTO type 2* functions was used in the positive and in the negative ranges of the z-axis.

Figure 3.21 presents different energy spectra of the H_2^+ computed with the 6-aug-cc-pVTZ+5K basis and with the addition of the non-atom-centered basis *GTO type 1* and *GTO type 2*. We observed that the number of Rydberg and continuum states increases when two *GTO type 1* basis are introduced in our calculation. As well as this, when 20 functions *GTO type 2* are introduced, the number of continuum states increases. However, we are limited by the linear dependencies and the inclusion of more functions *GTO type 2* dose not improve the energy spectrum.

3.5.3.3 Ghost atoms effects on high-harmonic generation

The effects of the basis set on the electron dynamics can be investigated by analyzing the HHG spectra of the H_2^+. In Figure 3.22 we show two HHG spectra calculated with the same laser parameters but with two different basis sets. In Figure 3.22(a) the HHG spectrum was computed with the 6-aug-cc-pVTZ+5K basis, and, in Figure 3.22(b) we used the 6-aug-cc-pVTZ+5K basis together with 2 basis *GTO type 1* and 28 functions *GTO type 2*. In Figure 3.22 the red line indicates the two-center minimum predicted by Lein's model [Lein 02], and the blue line denotes the cut-off energy predicted by the three-step model [Lewenstein 94].

In Figure 3.22(a) one observes that the 6-aug-cc-pVTZ+5K is not able to properly describe the HHG spectrum of the H_2^+ for the given laser parameters. The expected two-center interference minimum and the cut-off region are not described. In Figure 3.22(b), we can see the existence of high-energy peaks, corresponding to high-energy continuum states. This spectrum can be compared to the HHG spectrum computed by Fetic *et al.* [Fetic 17]. With this comparison one observes that the low-energy part of our spectrum is correctly described while the high-energy part, such as the cut-off region, is not accurately described with the addition of ghost atoms.

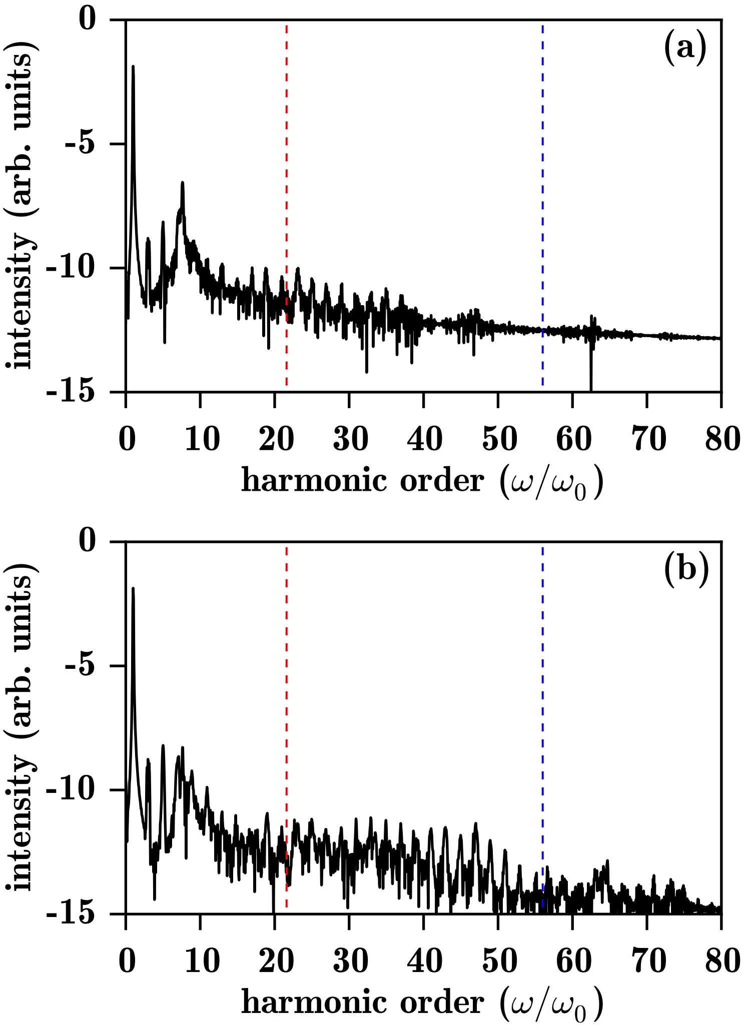

Figure 3.22: High-harmonic generation spectra of the molecular hydrogen ion H_2^+ computed in the length gauge with **(a)** a basis set of 6-aug-cc-pVTZ+5K and with **(b)** a 6-aug-cc-pVTZ+5K basis with 2 basis *GTO type 1* and 28 functions *GTO type 2* (see text). The laser pulse is polarized along the molecular axis with an intensity of $I = 3 \times 10^{14}$ W/cm^2 and a wavelength of $\lambda = 800$ nm. The total number of optical cycles was 18 using a $\cos^2$ envelope.

CHAPTER 4

Range-separated DFT for atomic spectra

In this chapter, we have reproduced our article titled *"Linear-response range-separated density-functional theory for atomic photoexcitation and photoionization spectra"*, published in *J. Chem. Phys.* **150**, 234104 (2019) [Zapata 19].

In this work, we have investigated the performance of the range-separated hybrid (RSH) scheme, which combines long-range Hartree-Fock (HF) and a short-range density-functional approximation (DFA), for calculating photoexcitation and photoionization spectra of the H and He atoms, using a B-spline basis set in order to correctly describe the continuum part of the spectra. The study of these simple systems allows us to quantify the influence on the spectra of the errors coming from the short-range exchange-correlation DFA and from the missing long-range correlation in the RSH scheme. We study the differences between using the long-range HF exchange (nonlocal) potential and the long-range exact exchange (local) potential. Contrary to the former, the latter supports a series of Rydberg states and gives reasonable photoexcitation and photoionization spectra, even without applying linear-response theory. The most accurate spectra are obtained with the linear-response time-dependent range-separated hybrid (TDRSH) scheme. In particular, for the He atom at the optimal value of the range-separation parameter, TDRSH gives slightly more accurate photoexcitation/photoionization spectra than standard linear-response time-dependent HF. More generally, the present work shows the potential of range-separated density-functional theory for calculating linear and nonlinear optical properties involving continuum states.

4.1 INTRODUCTION

Nowadays, time-dependent density-functional theory (TDDFT) [Runge 84], applied within the linear-response formalism [Gross 85, Casida 95, Petersilka 96], is a widely used approach for calculating photoexcitation spectra (transitions from bound to bound states) of electronic systems. In spite of many successes, it is however well known that usual (semi-)local density-functional approximations (DFAs), i.e. the local-density approximation (LDA) and generalized-gradient approximations (GGAs), for the exchange-correlation potential and its associated exchange-correlation kernel do not correctly describe long-range electronic transitions, such as those to Rydberg [Casida 98] and charge-transfer [Dreuw 03] states in atomic and molecular systems. A better description of Rydberg excitations can be obtained with exchange-correlation potential approximations having the correct $-1/r$ long-range asymptotic decay [van Leeuwen 94, Tozer 98, Casida 00, Schipper 00], even though it has been shown that accurate Rydberg excitation energies and oscillator strengths can in fact be extracted from LDA calculations in small atoms [Wasserman 03, Wasserman 05]. A more general solution for correcting both Rydberg and charge-transfer excitations is given by range-separated TDDFT approaches [Tawada 04, Yanai 04, Peach 06, Livshits 07, Baer 10, Fromager 13, Rebolini 13] which express the long-range part of the exchange potential and kernel at the Hartree-Fock (HF) level. These range-separated approaches also give reasonably accurate values for the ionization energy threshold [Yanai 04, Gerber 05, Tsuneda 10].

Linear-response TDDFT has also been used for calculating photoionization spectra (transitions from bound to continuum states) of atoms and molecules [Zangwill 80, Levine 84, Stener 95, Stener 97, Stener 97, Stener 00, Stener 01, Stener 05, Stener 06, Toffoli 06, Stener 07, Zhou 09]. These calculations are less standard in quantum chemistry since they involve spatial grid methods or B-spline basis sets for a proper description of the continuum states. In this case as well, usual (semi-)local DFAs provide a limited accuracy and asymptotically corrected exchange-correlation potential approximations give more satisfactory results. More accurate still, but less common, are photoionization spectra calculated with the exact-exchange (EXX) potential [Stener 01] or the localized HF exchange potential and its associated kernel [Zhou 09]. Recently, range-separated approximations have been successfully used for calculating photoexcitation and photoionization spectra of molecular systems using time-propagation TDDFT with Gaussian basis sets together with an effective lifetime model compensating for the missing continuum states [Lopata 13, Fernando 15, Sissay 16]. However, to the best of our knowledge, range-separated approximations have not yet been used in frequency-domain linear-response TDDFT calculations of photoionization spectra.

In this work, we explore the performance of the linear-response time-dependent range-separated hybrid (TDRSH) scheme [Rebolini 13, Toulouse 13] for calculating photoexcitation and photoionization spectra of the H and He atoms using a B-spline basis set to accurately describe the continuum part of the spectra. The TDRSH scheme allows us to treat long-range exchange effects at the HF level and short-range exchange-correlation effects within (semi-)local DFAs. First, the dependence of the range-separated hybrid (RSH) orbital energies on the range-separation parameter is investigated, as well as the effect of replacing the long-range HF exchange nonlocal potential by the long-range EXX local potential (resulting in a scheme that we refer to as RSH-EXX). Second, oscillator strengths directly computed with the RSH and the RSH-EXX orbitals are compared with oscillator strengths obtained with the linear-response TDRSH scheme. The study of the H atom allows us to quantify the residual self-interaction error coming from the short-range exchange-correlation DFA, and the study of the He atom permits to quantify the effect of the missing long-range correlation in the RSH scheme. This work constitutes a first step for applying range-separated TDDFT to strong-field phenomena, such as high-harmonic generation or above-threshold ionization, where long-range effects and continuum states play an important role.

The outline of the paper is as follows. In Section 4.2, firstly, we briefly review the RSH scheme and introduce the RSH-EXX variant, and, secondly, we review the linear-response TDRSH method. In Section 4.3, the basis set of B-spline functions is defined, and we indicate how the range-separated two-electron integrals are computed using an exact spherical harmonic expansion for the range-separated interaction. In Section 4.4 results are presented and discussed. Firstly, we show the performance of the B-spline basis set for describing the density of continuum states of the H atom within the different methods. Secondly, the dependence of the orbital energies of the H and He atoms on the range-separation parameter is analyzed. Thirdly, different calculated photoexcitation/photoionization spectra for the H and He atoms are discussed and compared with exact results. In Section 5.6, conclusions and perspectives are given. Unless otherwise indicated, Hartree atomic units are used throughout the paper.

4.2 RANGE-SEPARATED DENSITY-FUNCTIONAL THEORY

4.2.1 Range-separated hybrid scheme

Range-separated density-functional theory (see, e.g., Refs. [Savin 96, Toulouse 04]) is based on the splitting of the Coulomb electron-electron interaction $w_{\text{ee}}(r) = 1/r$ into long-range (lr) and short-range (sr) contributions

$$w_{\text{ee}}(r) = w_{\text{ee}}^{\text{lr}}(r) + w_{\text{ee}}^{\text{sr}}(r), \tag{4.1}$$

and the most common forms for the long-range and short-range interactions are

$$w_{\text{ee}}^{\text{lr}}(r) = \frac{\text{erf}(\mu r)}{r}, \tag{4.2}$$

and

$$w_{\text{ee}}^{\text{sr}}(r) = \frac{\text{erfc}(\mu r)}{r}. \tag{4.3}$$

where erf and erfc are the error function and the complementary error function, respectively, and μ is a tunable range-separation parameter controlling the range of the separation. Using this decomposition, it is possible to rigorously combine a long-range wave-function approach with a complementary short-range DFA.

The simplest approach in range-separated density-functional theory consists in using a single-determinant wave function for the long-range interaction. This leads to the RSH scheme [Ángyán 05] which spin orbitals $\{\varphi_p(\mathbf{x})\}$ (where $\mathbf{x} = (\mathbf{r}, \sigma)$ are space-spin coordinates) and orbital energies ε_p can be determined for a given system by the following eigenvalue problem,

$$\left(-\frac{1}{2}\boldsymbol{\nabla}^2 + v_{\text{ne}}(\mathbf{r}) + v_{\text{H}}(\mathbf{r}) + v_{\text{xc}}^{\text{sr}}(\mathbf{x})\right)\varphi_p(\mathbf{x}) + \int v_{\text{x}}^{\text{lr,HF}}(\mathbf{x}, \mathbf{x}')\varphi_p(\mathbf{x}')\text{d}\mathbf{x}' = \varepsilon_p\varphi_p(\mathbf{x}), \tag{4.4}$$

where $v_{\text{ne}}(\mathbf{r})$ is the nuclei-electron potential, $v_{\text{H}}(\mathbf{r})$ is the Hartree potential for the Coulomb electron-electron interaction,

$$v_{\text{H}}(\mathbf{r}) = \int n(\mathbf{x}')w_{\text{ee}}(|\mathbf{r} - \mathbf{r}'|)\text{d}\mathbf{x}', \tag{4.5}$$

where $n(\mathbf{x}) = \sum_i^{\text{occ}} |\varphi_i(\mathbf{x})|^2$ are the spin densities (i refers to occupied spin orbitals),

$v_{\mathrm{x}}^{\mathrm{lr,HF}}(\mathbf{x},\mathbf{x}')$ is the nonlocal HF exchange potential for the long-range electron-electron interaction,

$$v_{\mathrm{x}}^{\mathrm{lr,HF}}(\mathbf{x},\mathbf{x}') = -\sum_{i}^{\mathrm{occ}} \varphi_i^*(\mathbf{x}')\varphi_i(\mathbf{x}) w_{\mathrm{ee}}^{\mathrm{lr}}(|\mathbf{r}-\mathbf{r}'|), \tag{4.6}$$

and $v_{\mathrm{xc}}^{\mathrm{sr}}(\mathbf{x})$ is the short-range exchange-correlation potential

$$v_{\mathrm{xc}}^{\mathrm{sr}}(\mathbf{x}) = \frac{\delta \bar{E}_{\mathrm{xc}}^{\mathrm{sr}}}{\delta n(\mathbf{x})}, \tag{4.7}$$

where $\bar{E}_{\mathrm{xc}}^{\mathrm{sr}}$ is the complement short-range exchange-correlation density functional. In this work, we use the short-range spin-dependent LDA exchange-correlation functional of Ref. [Paziani 06] for $\bar{E}_{\mathrm{xc}}^{\mathrm{sr}}$. The long-range and short-range potentials, $v_{\mathrm{x}}^{\mathrm{lr,HF}}(\mathbf{x},\mathbf{x}')$ and $v_{\mathrm{xc}}^{\mathrm{sr}}(\mathbf{x})$, explicitly depend on the range-separation parameter μ, and consequently the spin orbitals, the orbital energies, and the density also implicitly depend on it. For $\mu = 0$, $v_{\mathrm{x}}^{\mathrm{lr,HF}}(\mathbf{x},\mathbf{x}')$ vanishes and $v_{\mathrm{xc}}^{\mathrm{sr}}(\mathbf{x})$ becomes the usual full-range LDA exchange-correlation potential, and thus the RSH scheme reduces to standard Kohn-Sham LDA. For $\mu \to \infty$, $v_{\mathrm{x}}^{\mathrm{lr,HF}}(\mathbf{x},\mathbf{x}')$ becomes the usual full-range HF exchange potential and $v_{\mathrm{xc}}^{\mathrm{sr}}(\mathbf{x})$ vanishes, and thus the RSH scheme reduces to standard HF.

In the present paper, we also consider the following variant of the RSH scheme,

$$\left(-\frac{1}{2}\boldsymbol{\nabla}^2 + v_{\mathrm{ne}}(\mathbf{r}) + v_{\mathrm{H}}(\mathbf{r}) + v_{\mathrm{xc}}^{\mathrm{sr}}(\mathbf{x}) + v_{\mathrm{x}}^{\mathrm{lr,EXX}}(\mathbf{x})\right)\varphi_p(\mathbf{x}) = \varepsilon_p\varphi_p(\mathbf{x}), \tag{4.8}$$

in which the long-range nonlocal HF exchange potential has been replaced by the long-range local EXX [Talman 76, Görling 94, Görling 95] potential

$$v_{\mathrm{x}}^{\mathrm{lr,EXX}}(\mathbf{x}) = \frac{\delta E_{\mathrm{x}}^{\mathrm{lr}}}{\delta n(\mathbf{x})}, \tag{4.9}$$

where $E_{\mathrm{x}}^{\mathrm{lr}}$ is the long-range exchange density functional [Toulouse 06a, Toulouse 06b]. We will refer to this scheme as RSH-EXX. The calculation of the EXX potential is involved [Filippi 96, Görling 99, Ivanov 99], with the exception of one- and two-electron systems. Indeed, for one-electron systems, the long-range EXX potential is simply

$$v_{\mathrm{x}}^{\mathrm{lr,EXX}}(\mathbf{x}) = -v_{\mathrm{H}}^{\mathrm{lr}}(\mathbf{r}), \tag{4.10}$$

and for systems of two electrons in a single spatial orbital, it is

$$v_{\mathrm{x}}^{\mathrm{lr,EXX}}(\mathbf{x}) = -\frac{1}{2} v_{\mathrm{H}}^{\mathrm{lr}}(\mathbf{r}), \tag{4.11}$$

where $v_{\mathrm{H}}^{\mathrm{lr}}(\mathbf{r}) = \int n(\mathbf{x}') w_{\mathrm{ee}}^{\mathrm{lr}}(|\mathbf{r} - \mathbf{r}'|) \mathrm{d}\mathbf{x}'$ is the long-range Hartree potential. For these one- and two-electron cases, it can be shown that Eq. (4.4) and Eq. (4.8) give identical occupied orbitals but different unoccupied orbitals. More generally, for systems with more than two electrons, the HF and EXX exchange potentials give similar occupied orbitals but very different unoccupied orbitals.

Once orbitals and orbital energies are obtained from Eq. (4.4) and Eq. (4.8), the bare oscillator strengths can be calculated. They are defined as

$$f_{ia}^{0} = \frac{2}{3} \omega_{ia}^{0} \sum_{\nu = x,y,z} |d_{\nu,ia}|^2, \tag{4.12}$$

where i and a refer to occupied and unoccupied spin orbitals, respectively, $\omega_{ia}^{0} = \varepsilon_a - \varepsilon_i$ are the bare excitation energies and $d_{\nu,ia} = \int \varphi_i^*(\mathbf{x}) r_\nu \varphi_a(\mathbf{x}) \mathrm{d}\mathbf{x}$ are the dipole-moment transition integrals. We will consider these bare excitation energies ω_{ia}^{0} and oscillator strengths f_{ia}^{0} for a first approximation to photoexcitation/photoionization spectra.

4.2.2 Linear-response time-dependent range-separated hybrid

In the time-dependent extension of the RSH scheme within linear response (referred to as TDRSH) [Rebolini 13, Toulouse 13, Fromager 13], one has to solve the following pseudo-Hermitian eigenvalue equation

$$\begin{pmatrix} \mathbf{A} & \mathbf{B} \\ -\mathbf{B}^* & -\mathbf{A}^* \end{pmatrix} \begin{pmatrix} \mathbf{X}_n \\ \mathbf{Y}_n \end{pmatrix} = \omega_n \begin{pmatrix} \mathbf{X}_n \\ \mathbf{Y}_n \end{pmatrix}, \tag{4.13}$$

whose solutions come in pairs: excitation energies $\omega_n > 0$ with eigenvectors $(\mathbf{X}_n, \mathbf{Y}_n)$, and de-excitation energies $\omega_n < 0$ with eigenvectors $(\mathbf{Y}_n^*, \mathbf{X}_n^*)$. The elements of the matrices $\mathbf{A}$ and $\mathbf{B}$ are

$$A_{ia,jb} = (\varepsilon_a - \varepsilon_i)\delta_{ij}\delta_{ab} + K_{ia,jb}, \tag{4.14}$$

$$B_{ia,jb} = K_{ia,bj}, \tag{4.15}$$

where i,j and a,b refer to occupied and unoccupied RSH spin orbitals, respectively, and the coupling matrix $\mathbf{K}$ contains the contributions from the Hartree kernel $f_{\mathrm{H}}(\mathbf{r}_1,\mathbf{r}_2) = w_{\mathrm{ee}}(|\mathbf{r}_1 - \mathbf{r}_2|)$, the long-range HF exchange kernel $f_{\mathrm{x}}^{\mathrm{lr,HF}}(\mathbf{x}_1,\mathbf{x}_2;\mathbf{x}_1',\mathbf{x}_2') = -w_{\mathrm{ee}}^{\mathrm{lr}}(|\mathbf{r}_1-\mathbf{r}_2|)\delta(\mathbf{x}_1-\mathbf{x}_2')\delta(\mathbf{x}_1'-\mathbf{x}_2)$, and the adiabatic short-range exchange-correlation kernel $f_{\mathrm{xc}}^{\mathrm{sr}}(\mathbf{x}_1,\mathbf{x}_2) = \delta v_{\mathrm{xc}}^{\mathrm{sr}}(\mathbf{x}_1)/\delta n(\mathbf{x}_2)$

$$\begin{aligned} K_{ia,jb} &= \langle aj|f_{\mathrm{H}}|ib\rangle + \langle aj|f_{\mathrm{x}}^{\mathrm{lr,HF}}|ib\rangle + \langle aj|f_{\mathrm{xc}}^{\mathrm{sr}}|ib\rangle \\ &= \langle aj|w_{\mathrm{ee}}|ib\rangle - \langle aj|w_{\mathrm{ee}}^{\mathrm{lr}}|bi\rangle + \langle aj|f_{\mathrm{xc}}^{\mathrm{sr}}|ib\rangle, \end{aligned} \tag{4.16}$$

where $\langle aj|w_{\mathrm{ee}}|ib\rangle$ and $\langle aj|w_{\mathrm{ee}}^{\mathrm{lr}}|bi\rangle$ are the two-electron integrals associated with the Coulomb and long-range interactions, respectively, and

$$\langle aj|f_{\mathrm{xc}}^{\mathrm{sr}}|ib\rangle = \iint \varphi_a^*(\mathbf{x}_1)\varphi_j^*(\mathbf{x}_2) f_{\mathrm{xc}}^{\mathrm{sr}}(\mathbf{x}_1,\mathbf{x}_2)\varphi_i(\mathbf{x}_1)\varphi_b(\mathbf{x}_2)\mathrm{d}\mathbf{x}_1\mathrm{d}\mathbf{x}_2. \tag{4.17}$$

Since we use the short-range LDA exchange-correlation density functional, for $\mu = 0$ the TDRSH scheme reduces to the usual linear-response time-dependent local-density approximation (TDLDA). For $\mu \to \infty$, the TDRSH scheme reduces to standard linear-response time-dependent Hartree-Fock (TDHF).

The time-dependent extension of the RSH-EXX variant within linear response (referred to as TDRSH-EXX) leads to identical equations with the exception that the long-range HF exchange kernel $f_{\mathrm{x}}^{\mathrm{lr,HF}}(\mathbf{x}_1,\mathbf{x}_2;\mathbf{x}_1',\mathbf{x}_2')$ is replaced by the long-range frequency-dependent EXX kernel [Görling 98a, Görling 98b]

$$f_{\mathrm{x}}^{\mathrm{lr,EXX}}(\mathbf{x}_1,\mathbf{x}_2;\omega) = \delta v_{\mathrm{x}}^{\mathrm{lr,EXX}}(\mathbf{x}_1,\omega)/\delta n(\mathbf{x}_2,\omega). \tag{4.18}$$

For one-electron systems, the long-range EXX kernel is simply

$$f_{\mathrm{x}}^{\mathrm{lr,EXX}}(\mathbf{x}_1,\mathbf{x}_2;\omega) = -f_{\mathrm{H}}^{\mathrm{lr}}(\mathbf{r}_1,\mathbf{r}_2), \tag{4.19}$$

and, for systems with two electrons in a single spatial orbital, it is

$$f_{\mathrm{x}}^{\mathrm{lr,EXX}}(\mathbf{x}_1,\mathbf{x}_2;\omega) = -\frac{1}{2} f_{\mathrm{H}}^{\mathrm{lr}}(\mathbf{r}_1,\mathbf{r}_2), \tag{4.20}$$

where $f_{\mathrm{H}}^{\mathrm{lr}}(\mathbf{r}_1,\mathbf{r}_2) = w_{\mathrm{ee}}^{\mathrm{lr}}(|\mathbf{r}_1 - \mathbf{r}_2|)$ is the long-range Hartree kernel. For these one- and two-electron cases, TDRSH and TDRSH-EXX give rise to identical excitation energies and oscillator strengths.

Finally, we can calculate the corresponding TDRSH (or TDRSH-EXX) oscillator strengths as

$$f_n = \frac{2}{3}\omega_n \sum_{\nu=x,y,z} \left|d_{\nu,ia}(X_{n,ia}+Y_{n,ia})\right|^2 . \tag{4.21}$$

In the limit of a complete basis set, the linear-response oscillator strengths in Eq. (4.21) always fulfill the Thomas-Reiche-Kuhn (TRK) sum rule, $\sum_n f_n = N$ where N is the electron number. The bare oscillator strengths of Eq. (4.12) fulfill the TRK sum rule only in the case where the orbitals have been obtained from an effective local potential, i.e. for LDA and RSH-EXX but not for HF and RSH (see Ref. [Toulouse 13]).

4.3 IMPLEMENTATION IN A B-SPLINE BASIS SET

In practice, each spin orbital is decomposed into a product of a spatial orbital and a spin function, $\varphi_p(\mathbf{x}) = \varphi_p(\mathbf{r})\delta_{\sigma_p,\sigma}$ where σ_p is the spin of the spin orbital p, and we use spin-adapted equations. As we investigate atomic systems, the spatial orbitals are written in spherical coordinates,

$$\varphi_p(\mathbf{r}) = R_{n_p l_p}(r) Y_{l_p}^{m_p}(\Omega), \tag{4.22}$$

where $Y_{l_p}^{m_p}(\Omega)$ are the spherical harmonics (Ω stands for the angles θ, ϕ) and the radial functions $R_{n_p l_p}(r)$ are expressed as linear combinations of B-spline functions of order k_s,

$$R_{n_p l_p}(r) = \sum_{\alpha=1}^{N_\mathrm{s}} c_\alpha^{n_p l_p} \frac{B_\alpha^{k_\mathrm{s}}(r)}{r}, \tag{4.23}$$

where N_s is the dimension of the basis. To completely define a basis of B-spline functions, a non-decreasing sequence of $N_\mathrm{s}+k_\mathrm{s}$ knot points (some knot points are possibly coincident) must be given [de Boor 78]. The B-spline function $B_\alpha^{k_\mathrm{s}}(r)$ is non zero only on the supporting interval $[r_\alpha, r_{\alpha+k_\mathrm{s}}]$ (containing $k_\mathrm{s}+1$ consecutive knot points) and is a piecewise function composed of polynomials of degree $k_\mathrm{s}-1$ with continuous first $k_\mathrm{s}-m$ derivatives across each knot of multiplicity m. We have chosen the first and the last knots to be k_s-fold degenerate, i.e. $r_1 = r_2 = \cdots = r_{k_\mathrm{s}} = R_\mathrm{min}$ and $r_{N_\mathrm{s}+1} = r_{N_\mathrm{s}+2} = \cdots = r_{N_\mathrm{s}+k_\mathrm{s}} = R_\mathrm{max}$, while the multiplicity of the other knots is unity. The spatial grid spacing was chosen to be constant in the whole radial space between two consecutive non-coincident points and is given by $\Delta r = R_{\text{max}}/(N_{\text{s}} - k_{\text{s}} + 1)$. In the present work, the first and the last B-spline functions were removed from the calculation to ensure zero boundary conditions at $r = R_{\text{min}}$ and $r = R_{\text{max}}$. The results presented in this paper have been obtained using the following parameters: $k_{\text{s}} = 8$, $N_{\text{s}} = 200$, $R_{\text{min}} = 0$, and $R_{\text{max}} = 100$ bohr. Moreover, we need to use only s and p_z spherical harmonics.

Working with such a B-spline representation, one must compute matrix elements involving integrals over B-spline functions. The principle of the calculation of one-electron and two-electron integrals over B-spline functions are well described by Bachau *et al.* in Ref. [Bachau 01]. We will now briefly review the computation of the standard Coulomb two-electron integrals over B-spline functions, and then we will present the calculation of the long-range or short-range two-electron integrals over B-spline functions, the latter being original to the present work.

4.3.1 Coulomb two-electron integrals

The Coulomb electron-electron interaction is given by

$$w_{\text{ee}}(|\mathbf{r} - \mathbf{r}'|) = \frac{1}{\left(|\mathbf{r}|^2 + |\mathbf{r}'|^2 - 2|\mathbf{r}||\mathbf{r}'|\cos\gamma\right)^{1/2}}, \tag{4.24}$$

where $\mathbf{r}$ and $\mathbf{r}'$ are electron vector positions and γ is the angle between them. The multipolar expansion for this interaction is

$$w_{\text{ee}}(|\mathbf{r} - \mathbf{r}'|) = \sum_{k=0}^{\infty} \left[\frac{r_<^k}{r_>^{k+1}}\right] \sum_{m_k=-k}^{k} (-1)^{m_k} C_{-m_k}^k(\Omega) C_{m_k}^k(\Omega'), \tag{4.25}$$

where $r_< = \min(|\mathbf{r}|, |\mathbf{r}'|)$ and $r_> = \max(|\mathbf{r}|, |\mathbf{r}'|)$ and $C_{m_k}^k(\Omega) = (4\pi/(2k+1))^{1/2}\, Y_k^{m_k}(\Omega)$ are the renormalized spherical harmonics. The Coulomb two-electron integrals, in the spatial orbital basis, can then be expressed as the sum of products of radial integrals and angular factors

$$\begin{aligned} \langle pq|w_{\text{ee}}|tu\rangle &= \sum_{k=0}^{\infty} R^k(p,q;t,u) \sum_{m_k=-k}^{k} \delta_{m_k, m_p - m_t}\delta_{m_k, m_q - m_u} \\ &\times (-1)^{m_k} c^k(l_p, m_p, l_t, m_t) c^k(l_q, m_q, l_u, m_u), \end{aligned} \tag{4.26}$$

where $R^k(p,q;t,u)$ are the two-dimensional radial Slater integrals and the angular coefficients $c^k(l_p,m_p,l_t,m_t)$ and $c^k(l_q,m_q,l_u,m_u)$ are obtained from the Gaunt coefficients [Cowan 81, Čertík 12]. The coefficient $c^k(l,m,l',m')$ is non zero only if $|l-l'| \leq k \leq l+l'$ and if $l+l'+k$ is an even integer, which makes the sum over k in Eq. (4.26) exactly terminate. The Slater integrals are defined as

$$\begin{aligned} R^k(p,q;t,u) &= \sum_{\alpha=1}^{N_\mathrm{s}} \sum_{\lambda=1}^{N_\mathrm{s}} \sum_{\beta=1}^{N_\mathrm{s}} \sum_{\nu=1}^{N_\mathrm{s}} c_\alpha^{n_p l_p} c_\lambda^{n_q l_q} c_\beta^{n_t l_t} c_\nu^{n_u l_u} \\ &\quad \times R^k(\alpha,\lambda;\beta,\nu), \end{aligned} \tag{4.27}$$

where $R^k(\alpha,\lambda;\beta,\nu)$ are the Slater matrix elements given by

$$\begin{aligned} R^k(\alpha,\lambda;\beta,\nu) &= \int_0^\infty \int_0^\infty B_\alpha^{k_\mathrm{s}}(r) B_\lambda^{k_\mathrm{s}}(r') \left[\frac{r_<^k}{r_>^{k+1}}\right] \\ &\quad \times B_\beta^{k_\mathrm{s}}(r) B_\nu^{k_\mathrm{s}}(r') \mathrm{d}r \mathrm{d}r'. \end{aligned} \tag{4.28}$$

In order to compute the Slater matrix elements $R^k(\alpha,\lambda;\beta,\nu)$, we have implemented the integration-cell algorithm developed by Qiu and Froese Fischer [Qiu 99]. This algorithm exploits all possible symmetries and B-spline properties to evaluate efficiently the integrals in each two-dimensional radial region on which the integrals are defined. Gaussian quadrature is used to compute the integrals in each cell.

4.3.2 Long-range and short-range two-electron integrals

A closed form of the multipolar expansion of the short-range electron-electron interaction defined in Eq. (4.3) was determined by Ángyán *et al.* [Ángyán 06], following a previous work of Marshall [Marshall 02] who applied the Gegenbauer addition theorem to the Laplace transform of Eq. (4.3). This exact expansion is

$$w_\mathrm{ee}^\mathrm{sr}(|\mathbf{r}-\mathbf{r}'|) = \sum_{k=0}^{\infty} S^k(r_>,r_<;\mu) \times \sum_{m_k=-k}^{k} (-1)^{m_k} C_{-m_k}^k(\Omega) C_{m_k}^k(\Omega'), \tag{4.29}$$

where the μ-dependent radial function is written in terms of the scaled radial coordinates $\Xi = \mu\, r_>$ and $\xi = \mu\, r_<$ as

$$S^k(r_>,r_<;\mu) = \mu\, \Phi^k(\Xi,\xi), \tag{4.30}$$

with

$$\begin{aligned}\Phi^k(\Xi,\xi) &= H^k(\Xi,\xi) + F^k(\Xi,\xi) \\ &+ \sum_{m=1}^{k} F^{k-m}(\Xi,\xi)\frac{\Xi^{2m}+\xi^{2m}}{(\xi\ \Xi)^m},\end{aligned} \tag{4.31}$$

and the introduced auxiliary functions

$$\begin{aligned}H^k(\Xi,\xi) &= \frac{1}{2(\xi\ \Xi)^{k+1}}\left[\left(\Xi^{2k+1}+\xi^{2k+1}\right)\mathrm{erfc}(\Xi+\xi)\right. \\ &\left. - \left(\Xi^{2k+1}-\xi^{2k+1}\right)\mathrm{erfc}(\Xi-\xi)\right],\end{aligned} \tag{4.32}$$

and

$$\begin{aligned}F^k(\Xi,\xi) &= \frac{2}{\pi^{1/2}}\sum_{p=0}^{k}\left(-\frac{1}{4(\xi\ \Xi)}\right)^{p+1}\frac{(k+p)!}{p!(k-p)!} \\ &\times\left[(-1)^{k-p}e^{-(\Xi+\xi)^2}-e^{-(\Xi-\xi)^2}\right].\end{aligned} \tag{4.33}$$

In order to arrive at a separable expression in Ξ and ξ, Ángyán *et al.* [Ángyán 06] also introduced a power series expansion of the radial function $\Phi^k(\Xi,\xi)$ in the smaller reduced variable ξ. However, the range of validity of this expansion truncated to the first few terms is limited to small values of ξ, i.e. $\xi \lesssim 1.5$, and higher-order expansions show spurious oscillations. After some tests, we decided to use the exact short-range radial function $\Phi^k(\Xi,\xi)$ without expansion in our work.

The expression of the short-range two-electron integrals $\langle pq|w_{\text{ee}}^{\text{sr}}|tu\rangle$ is then identical to the one in Eq. (4.26) with the simple difference that the radial term is not given by the standard Slater matrix elements. Now, the radial kernel in Eq. (4.28) is changed to that of Eq. (4.30). Due to the fact that the radial kernel is not multiplicatively separable in the variables $r_>$ and $r_<$, the integration-cell algorithm is modified in order to calculate all integrals as non-separable two-dimensional integrals. In a second step, the long-range two-electron integrals can be simply obtained by difference

$$\langle pq|w_{\text{ee}}^{\text{lr}}|tu\rangle = \langle pq|w_{\text{ee}}|tu\rangle - \langle pq|w_{\text{ee}}^{\text{sr}}|tu\rangle. \tag{4.34}$$

4.4 RESULTS AND DISCUSSION

In this section, photoexcitation and photoionization spectra for the H and He atoms are presented. Photoexcitation and photoionization processes imply transitions from bound to bound and from bound to continuum states, respectively. For this reason, we first check the density of continuum states obtained with our B-spline basis set. After that, we show how orbital energies for the H and He atoms are influenced by the range-separation parameter μ. Finally, having in mind these aspects, we discuss the different calculated spectra. All the studied transitions correspond to dipole-allowed spin-singlet transitions from the Lyman series, i.e. $1\text{s} \to n\text{p}$.

4.4.1 Density of continuum states

In Figure 4.1, the radial density of states (DOS) of a free particle in a spherical box is compared with the radial DOS of the continuum p orbitals of the H atom computed with the exact Hamiltonian or with the HF or LDA effective Hamiltonian using the B-spline basis set. The radial DOS of a free particle is given by [Bachau 01] $\rho(\varepsilon) = R_{\text{max}}/\pi\sqrt{2\varepsilon}$ where R_{max} is the radial size of the box, while for the different Hamiltonians using the B-spline basis set (with the same R_{max}) the radial DOS is calculated by finite differences as $\rho(\varepsilon_p) = 2/(\varepsilon_{p+1} - \varepsilon_{p-1})$ where ε_p are positive orbital energies.

As one can observe, the radial DOS computed with the LDA or the HF Hamiltonian is essentially identical to the DOS of the free particle. This can be explained by the fact that since the unoccupied LDA and HF orbitals do not see a $-1/r$ attractive potential they are all unbound and they all contribute to the continuum, similarly to the free-particle case. By contrast, for the exact Hamiltonian with the same B-spline basis set, one obtains a slightly smaller DOS in the low-energy region. This is due to the presence of the $-1/r$ attractive Coulomb potential which supports a series of bound Rydberg states, necessarily implying less unoccupied orbitals in the continuum for a given basis.

We have checked that, by increasing the size of the simulation box, together with the number of B-spline functions in the basis so as to keep constant the density of B-spline functions, the DOS of the exact Hamiltonian converges, albeit slowly, to the free-particle DOS. This must be the case since, for potentials vanishing at infinity, the global density of unbound states is independent of the potential for

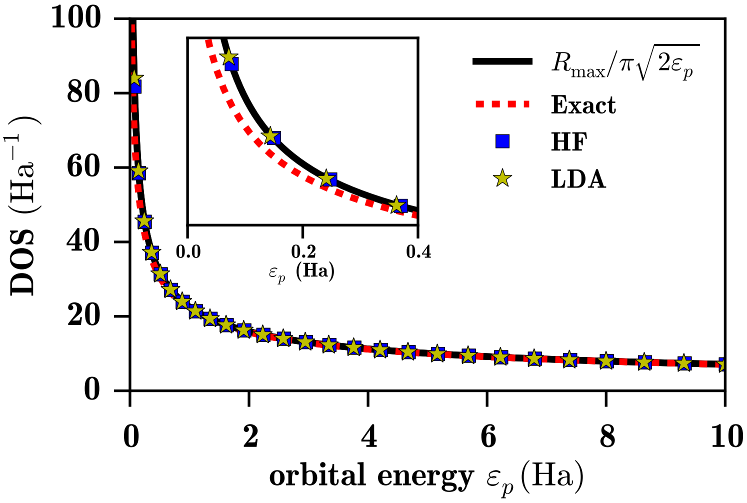

Figure 4.1: Radial density of states (DOS) for a free particle, $\rho(\varepsilon_p) = R_{\max}/\pi\sqrt{2\varepsilon_p}$, in a spherical box of size $R_{\max} = 100$ bohr, and for the continuum p orbitals of the H atom computed with the exact Hamiltonian, or with the HF or LDA effective Hamiltonian using the B-spline basis set with the same $R_{\max}$.

an infinite simulation box (only the local DOS depends on the potential, see e.g. Ref. [Dick 12]). From a numerical point of view, the computation of the DOS can be seen as a convergence test. With the present basis set, a huge energy range of the continuum spectrum is described correctly, and the difference between the DOS of the exact Hamiltonian and the free-particle DOS at low energies ($0.0 - 0.2$ Ha) is only about 10^{-4} Ha^{-1}. This difference is small enough to fairly compare the different methods considered in this paper.

The calculation of the DOS is also important in order to compute proper oscillator strengths involving continuum states. Because of the use of a finite simulation box, the calculated positive-energy orbitals form, of course, a discrete set and not strictly a continuum. These positive-energy orbitals are thus not energy normalized as the exact continuum states should be. To better approximate pointwise the exact continuum wave functions, the obtained positive-energy orbitals should be renormalized. Following Macías *et al.* [Macías 88], we renormalize the positive-energy orbitals by the square root of the DOS as $\tilde{\varphi}_p(\mathbf{r}) = \sqrt{\rho(\varepsilon_p)}\varphi_p(\mathbf{r})$.

4.4.2 Range-separated orbital energies

In Figure 4.2 we show the 1s and the low-lying p orbital energies for the H atom calculated with both the RSH and RSH-EXX methods as a function of the range-separation parameter μ.

As one observes in Figure 4.2(a), with the RSH method only the 1s ground state

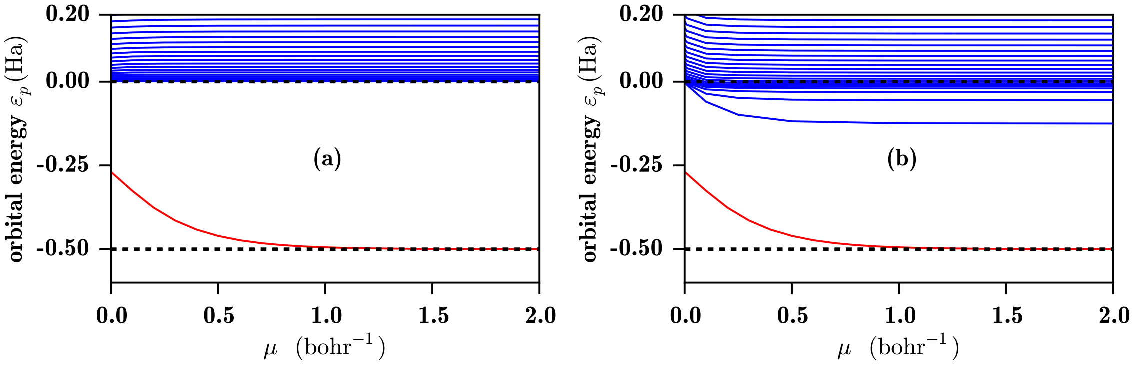

Figure 4.2: Orbital energies obtained with the RSH **(a)** and with the RSH-EXX **(b)** methods as a function of range-separation parameter μ for the H atom. The occupied 1s orbital energy is plotted in red and the unoccupied p orbital energies are plotted in blue. Horizontal dotted lines indicate the exact 1s orbital energy (-0.5 Ha) and the ionization limit (0 Ha).

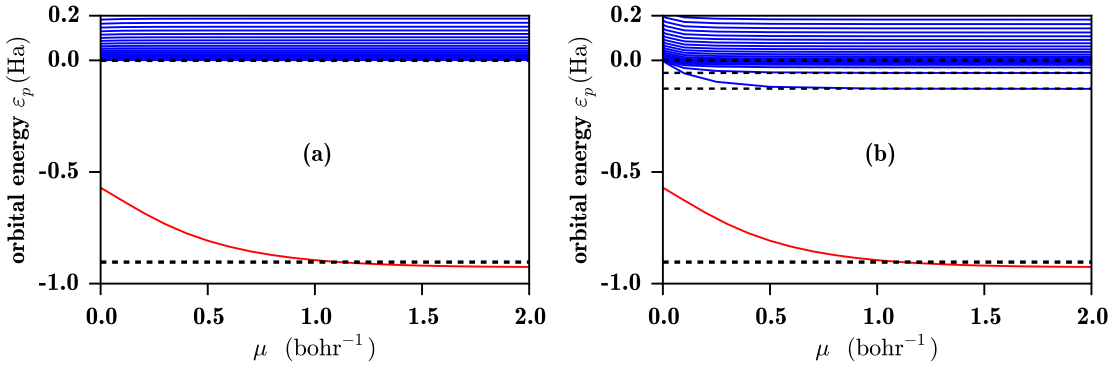

Figure 4.3: Orbital energies obtained with the RSH **(a)** and with the RSH-EXX **(b)** methods as a function of range-separation parameter μ for the He atom. The occupied 1s orbital energy is plotted in red and the unoccupied p orbital energies are plotted in blue. Horizontal dotted lines indicate exact Kohn-Sham orbital energies [Umrigar 98], including the opposite of the exact ionization energy (-0.9036 Ha) for the 1s orbital energy and the ionization limit (0 Ha).

is bound, and the energy of this state is strongly dependent on μ. At $\mu = 0$, the self-interaction error introduced by the LDA exchange-correlation potential is maximal. But, when μ increases, the long-range HF exchange potential progressively replaces the long-range part of the LDA exchange-correlation potential and the self-interaction error is gradually eliminated until reaching the HF limit for $\mu \to \infty$, where one obtains the exact 1s orbital energy. The p orbitals (and all the other unoccupied orbitals) are always unbound and their (positive) energies are insensible to the value of μ. One also observes that the approximate continuum of p orbitals has a DOS correctly decreasing as the energy increases, as previously seen in Figure 4.1.

In Figure 4.2(b), one sees that the 1s orbital energy computed with the RSH-EXX method is identical to the 1s orbital energy obtained by the RSH scheme, as expected. However, a very different behavior is observed for the unoccupied p orbitals. Starting from the LDA limit at $\mu = 0$ where all unoccupied orbitals are unbound, when the value of μ increases one sees the emergence of a series of bound Rydberg states coming down from the continuum. This is due to the introduction of an attractive $-1/r$ term in the long-range EXX potential, which supports a Rydberg series. For $\mu \to \infty$, we obtain the spectrum of the exact hydrogen Hamiltonian calculated with the B-spline basis set. Necessarily, with the finite basis used, the appearance of the discrete bound states is accompanied by a small reduction of the density of continuum states, as we already observed in Figure 4.1 with the exact Hamiltonian.

Another interesting aspect that can be observed in Figure 4.2(b) is the fact that the different bound-state energies reach their exact $\mu \to \infty$ values at different values of μ. Thus, for a fixed small value of μ, each bound-state energy is affected differently by the self-interaction error. For the compact 1s orbital, the self-interaction error is eliminated for $\mu \gtrsim 1$ bohr^{-1}. For the more diffuse 2p Rydberg state, the self-interaction error is essentially eliminated with $\mu \gtrsim 0.5$ bohr^{-1}. When we continue to climb in the Rydberg series, the orbitals become more and more diffuse and the self-interaction error is eliminated from smaller and smaller values of μ.

In Figure 4.3, the 1s and low-lying p orbital energies for the He atom are shown. Again, for the RSH method, one sees in Fig. Figure 4.3(a) that only the occupied 1s orbital is bound and all the unoccupied p orbitals are in the continuum. Similarly to the case of the H atom, at $\mu = 0$ the 1s orbital energy is too high, which can essentially be attributed to the self-interaction error in the LDA exchange-correlation potential. This error decreases when μ increases and the 1s orbital energy converges to its HF value for $\mu \to \infty$. However, contrary to the case of the H atom, for this two-electron system, the 1s HF orbital energy is not equal to the opposite of the exact ionization energy but is slightly too low due to missing correlation effects. In the spirit of the optimally tuned range-separated hybrids [Livshits 07, Baer 10, Stein 09b, Stein 09a], the range-separation parameter μ can be chosen so that the HOMO orbital energy is equal to the opposite of the exact ionization energy, which gives $\mu = 1.115$ bohr^{-1} for the He atom.

As regards the RSH-EXX method, one sees again in Figure 4.3(b) that, for this two-electron system, the 1s RSH-EXX orbital energy is identical to the 1s RSH orbital energy. As in the case of the H atom, the introduction of the long-range EXX potential generates a series of bound Rydberg states, whose energies converge to the

Kohn-Sham EXX orbital energies for $\mu \to \infty$. For the Rydberg states of the He atom, it turns out that the Kohn-Sham EXX orbital energies are practically identical to the exact Kohn-Sham orbital energies [Umrigar 98], implying that the Kohn-Sham correlation potential has essentially no effect on these Rydberg states. As we will see, contrary to the RSH case, the set of unoccupied RSH-EXX orbitals can be considered as a reasonably good first approximation for the computation of photoexcitation and photoionization spectra, even before applying linear-response theory.

4.4.3 Photoexcitation/photoionization in the hydrogen atom

In Figure 4.4, photoexcitation/photoionization spectra for the H atom calculated with different methods are shown. For the calculation using the exact Hamiltonian, the spectrum is correctly divided into a discrete and a continuum part, corresponding to the photoexcitation and photoionization processes, respectively. As already discussed in Section 4.4.1, for all calculations, the continuum states have been renormalized, or equivalently the oscillator strengths of the continuum part of the spectrum have been renormalized as $\tilde{f}_{1\text{s}\to n\text{p}} = \rho(\varepsilon_{n\text{p}}) f_{1\text{s}\to n\text{p}}$ where $\rho(\varepsilon_{n\text{p}})$ is the DOS at the corresponding positive orbital energy $\varepsilon_{n\text{p}}$. Moreover, for better readability of the spectra, following Refs. [Friedrich 98, Wasserman 03, Yang 09], we have also renormalized the oscillator strengths of the discrete part of the spectrum as $\tilde{f}_{1\text{s}\to n\text{p}} = n^3 f_{1\text{s}\to n\text{p}}$ where n is the principal quantum number of the excited p orbital. This makes the transition between the discrete and the continuum part of the spectrum smooth. Another thing is, since we are working with a finite B-spline basis set principally targeting a good continuum, we obtain only a limited number of Rydberg states and the last Rydberg

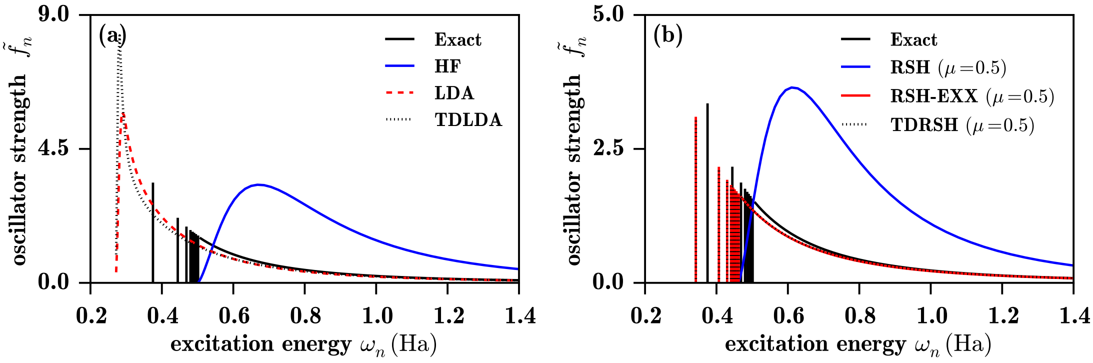

Figure 4.4: Photoexcitation/photoionization spectra calculated with different methods for the H atom. In **(a)** comparison of the HF, LDA, and TDLDA methods with respect to the calculation with the exact Hamiltonian. In **(b)** comparison of the RSH, RSH-EXX, and TDRSH methods (all of them with a range-separation parameter of $\mu = 0.5$ bohr^{-1}) with respect to the calculation with the exact Hamiltonian.

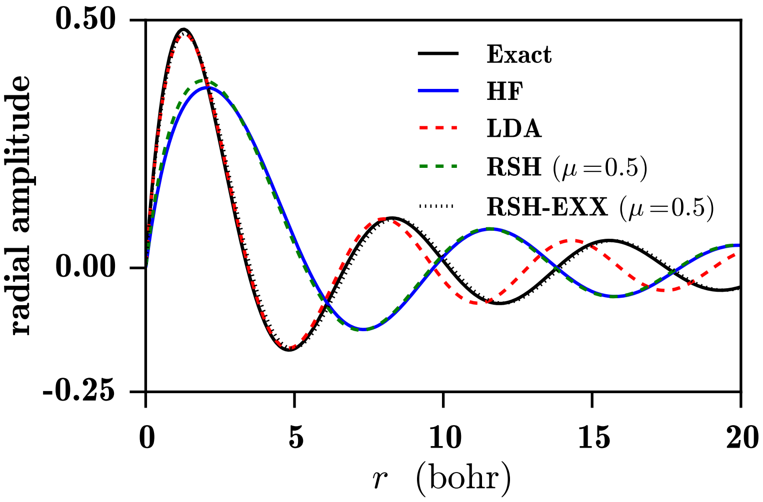

Figure 4.5: Comparison of the renormalized radial amplitude $\tilde{R}(r) = \sqrt{\rho(\varepsilon)}R(r)$ of the continuum p orbital involved in the transition energy $\omega_n = \varepsilon - \varepsilon_{1s} = 0.8$ Ha calculated by HF, LDA, RSH, and RSH-EXX (with a range-separation parameter of $\mu = 0.5$ bohr^{-1}) with respect to the exact calculation for the H atom.

states near the ionization threshold are not accurately described. In particular, the corresponding oscillator strengths are overestimated (not shown). To fix this problem, we could for example use quantum defect theory in order to accurately extract the series of Rydberg states [Al-Sharif 98, Friedrich 98, van Faassen 06, van Faassen 09]. However, for the propose of the present work, we did not find necessary to do that, and instead we have simply corrected the oscillator strengths of the last Rydberg states by interpolating between the oscillator strengths of the first five Rydberg states and the oscillator strength of the first continuum state using a second-order polynomial function of the type $\tilde{f}_n = c_0 + c_1\ \omega_n + c_2\ \omega_n^2$. This procedure was applied for all spectra having a discrete part.

Let us first discuss the spectra in Figure 4.4(a). The LDA spectrum, calculated using the bare oscillator strengths of Eq. (4.12), does not possess a discrete photoexcitation part, which was of course expected since the LDA potential does not support bound Rydberg states, as seen in the $\mu = 0$ limit of Figure 4.2. The ionization threshold energy, giving the onset of the continuum spectrum, is much lower than the exact value (0.5 Ha) due to the self-interaction error in the ground-state orbital energy. At the ionization threshold, the LDA oscillator strengths are zero, in agreement with the Wigner-threshold law [Wigner 48, Sadeghpour 00] for potentials lacking a long-range attractive $-1/r$ Coulomb tail. Close above the ionization threshold, the LDA spectrum has an unphysical large peak, which corresponds to continuum states with an important local character. However, as noted in Ref. [Wasserman 03], at the exact Rydberg transition energies, the LDA continuum oscillator strengths are actually reasonably good approximations to the exact discrete oscillator strengths, which was explained by the fact that the LDA potential is approximately the exact Kohn-Sham potential shifted by a constant. Moreover, above the exact ionization energy, LDA reproduces relatively well the exact photoionization spectrum and becomes essentially asymptotically exact in the high-energy limit. This is consistent with the fact that, at a sufficiently high transition energy, the LDA continuum orbitals are very similar to the exact ones, at least in the spatial region relevant for the calculation of the oscillation strengths, as shown in Figure 4.5.

The TDLDA spectrum differs notably from the LDA spectrum only in that the unphysical peak at around 0.3 Ha, close above its ionization threshold, has an even larger intensity. This increased intensity comes from the contribution of the LDA exchange-correlation kernel (not shown). The LDA exchange-correlation kernel being local, its larger impact is for the low-lying LDA continuum orbitals having a local character. As the TRK sum rule must be satisfied, the higher peak in the TDLDA spectrum is followed by a decrease of the oscillator strengths faster than in the LDA spectrum, until they reach the same asymptotic behavior.

The HF spectrum in 4.4(a) not only has no discrete photoexcitation part, as expected since the unoccupied HF orbitals are unbound (see the $\mu \to \infty$ limit of Figure 4.2a), but does not even look as a photoionization spectrum. The HF unoccupied orbitals actually represent approximations to the continuum states of the H^- anion, and are thus much more diffuse than the exact continuum states of the H atom, as shown in Figure 4.5. Consequently, the HF spectrum has in fact the characteristic shape of the photodetachment spectrum of the H^- anion [Bethe 57, Rau 96] (with the caveat that the initial state is the 1s orbital of the H atom instead of the 1s orbital of the H^- anion). Finally, note that, for the H atom, linear-response TDHF gives of course the exact photoexcitation/photoionization spectrum.

Let us now discuss the spectra obtained with the range-separated methods in Figure 4.4(b). The common value of the range-separation parameter $\mu = 0.5$ bohr^{-1} has been used [Gerber 05]. The RSH spectrum looks like the photodetachment spectrum of the H^- anion. This is not surprising since the RSH effective Hamiltonian contains a long-range HF exchange potential. The RSH continuum orbitals are similarly

Table 4.1: Excitation energies (ω_n in Ha) and oscillator strengths (f_n) of the first discrete transitions calculated with different methods for the He atom. The ionization energy is also given.

Transition	Exact[a]		TDHF		RSH-EXX[b]		TDRSH[b]	
	ω_n	f_n	ω_n	f_n	ω_n	f_n	ω_n	f_n
$1^1S \to 2^1P$	0.7799	0.2762	0.7970	0.2518	0.7766	0.3303	0.7827	0.2547
$1^1S \to 3^1P$	0.8486	0.0734	0.8636	0.0704	0.8474	0.0857	0.8493	0.0708
$1^1S \to 4^1P$	0.8727	0.0299	0.8872	0.0291	0.8721	0.0344	0.8729	0.0292
$1^1S \to 5^1P$	0.8838	0.0150	0.8982	0.0148	0.8835	0.0172	0.8839	0.0148
$1^1S \to 6^1P$	0.8899	0.0086	0.9042	0.0087	0.8897	0.0100	0.8899	0.0087
Ionization energy	0.9036		0.9180		0.9036		0.9036	

[a] From Ref. [Kono 84].
[b] Calculations were performed with $\mu = 1.115$ bohr^{-1}.

diffuse as the HF continuum orbitals, as shown in Figure 4.5. The RSH ionization threshold energy is slightly smaller than the exact value (0.5 Ha) due to the remaining self-interaction error in the 1s orbital energy stemming from the short-range LDA exchange-correlation potential at this value of μ. The RSH-EXX ionization threshold is identical to the RSH one, but, contrary to the RSH spectrum, the RSH-EXX spectrum correctly shows a discrete photoexcitation part and a continuum photoionization part. Beside the small redshift of the spectrum, the self-interaction error at this value of μ manifests itself in slightly too small RSH-EXX oscillator strengths. The RSH-EXX continuum orbitals are very similar to the exact continuum orbitals, as shown in Figure 4.5. Finally, at this value of μ, TDRSH gives a photoexcitation/photoionization spectrum essentially identical to the RSH-EXX spectrum.

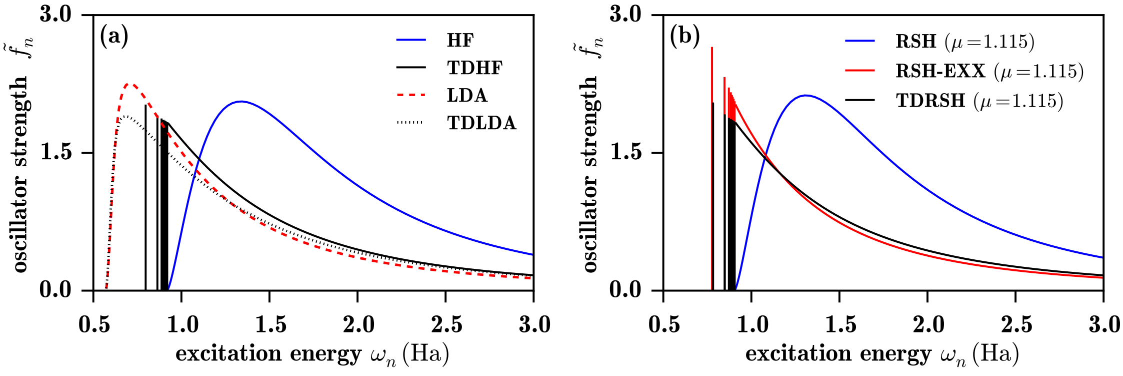

Figure 4.6: Photoexcitation and photoionization spectra calculated with different methods for the He atom. In **(a)** comparison of HF, TDHF, LDA, and TDLDA methods. In **(b)** comparison of RSH, RSH-EXX, and TDRSH methods (all of them with a range-separation parameter of $\mu = 1.115$ bohr^{-1}).

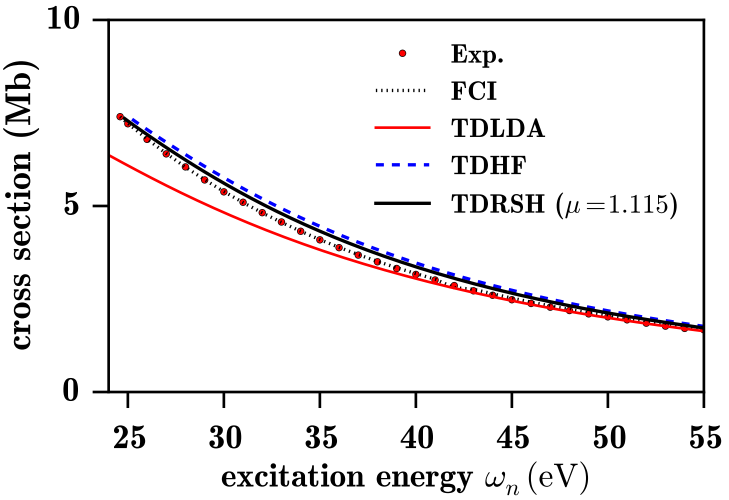

Figure 4.7: Photoionization cross-section profile for the He atom. Normalized cross sections are given (in Hartree atomic units) by $\sigma_n = (2\pi^2/c)\tilde{f}_n$ where $\tilde{f}_n$ are the renormalized oscillator strengths and c is the speed of light. Conversion factors 1 Ha = 27.207696 eV and 1 bohr^2 = 28.00283 Mb are employed. The experimental data and the FCI results are from Ref. [Venuti 96].

4.4.4 Photoexcitation/photoionization in the helium atom

In Figure 4.6, different photoexcitation/photoionization spectra for the He atom are shown. As in the H atom case, the oscillator strengths of the discrete part of the TDHF, RSH-EXX, and TDRSH spectra have been interpolated (using again the oscillator strengths of first five Rydberg states and of the first continuum state) to correct the overestimation of the oscillator strengths for the last Rydberg transitions. The excitation energies and the (non-interpolated) oscillator strengths of the first five discrete transitions are reported in Table 4.1 and compared with exact results. The photoionization part of some of the calculated spectra are compared with full configuration-interaction (FCI) calculations and experimental results in Figure 4.7.

In Figure 4.6(a), one sees that the HF spectrum looks again like a photodetachment spectrum, corresponding in this case to the He$^-$ anion. By contrast, TDHF gives a reasonable photoexcitation/photoionization spectrum. In particular, for the first discrete transitions listed in Table 4.1, TDHF gives slightly too large excitation energies by at most about 0.02 Ha (or 0.5 eV) and slightly too small oscillator strengths by at most about 0.025. The ionization energy is also slightly too large by about 0.015 Ha, as already seen from the HF 1s orbital energy in the $\mu \to \infty$ limit of Figure 4.3. As regards the photoionization part of the spectrum, one sees in Figure 4.7 that TDHF gives slightly too large photoionization cross sections.

The LDA spectrum in Figure 4.6(a) is also similar to the LDA spectrum for the H atom. The ionization threshold energy is much too low, and the spectrum lacks a discrete part and has an unphysical maximum close above the ionization threshold. Except from that, taking as reference the TDHF spectrum (which is close to the exact spectrum), the LDA spectrum is a reasonable approximation to the photoionization spectrum and, again as noted in Ref. [Wasserman 03], a reasonable continuous approximation to the photoexcitation spectrum. In comparison to LDA, TDLDA [1] gives smaller and less accurate oscillator strengths in the lower-energy part of the spectrum but, the TRK sum rule having to be preserved, larger oscillator strengths in the higher-energy part of the spectrum, resulting in an accurate high-energy asymptotic behavior as seen in Figure 4.7.

Figure 4.6(b) shows the spectra calculated with RSH, RSH-EXX, and TDRSH using for the range-separation parameter the value $\mu = 1.115$ bohr^{-1} which imposes the exact ionization energy, as explained in Subection 4.4.2. The RSH spectrum is similar to the HF spectrum and does not represent a photoexcitation/photoionization spectrum. By contrast, the RSH-EXX spectra is qualitatively correct for a photoexcitation/photoionization spectrum. As shown in Table 4.1, in comparison with TDHF, RSH-EXX gives more accurate Rydberg excitation energies, with a largest error of about 0.003 Ha (or 0.08 eV), but less accurate oscillator strengths which are significantly overestimated. The TDRSH method also gives a correct photoexcitation/photoionization spectrum, with the advantage that it gives Rydberg excitation energies as accurate as the RSH-EXX ones and corresponding oscillator strengths as accurate as the TDHF ones. As shown in Figure 4.7, TDRSH also gives a slightly more accurate photoionization cross-section profile than TDHF.

---

[1] Contrary to our Figure 4.6(a), the TDLDA spectrum of the He atom shown in Figure 6 of Ref. [Wasserman 03] has a larger maximum than the LDA spectrum. This discrepancy is due to the fact that the TDLDA spectrum shown in Ref. [Wasserman 03] comes in fact from Ref. [Stener 01], where it was calculated by replacing the LDA 1s orbital energy by the opposite of the exact ionization energy. We have checked that this results not only in an energy shift of the spectrum but also to larger oscillator strengths. The true TDLDA spectrum of the He atom is thus the one shown in the present Figure 4.6(a).

4.5 CONCLUSIONS

We have investigated the performance of the RSH scheme for calculating photoexcitation/photoionization spectra of the H and He atoms, using a B-spline basis set in order to correctly describe the continuum part of the spectra. The study of these simple systems allowed us to quantify the influence on the spectra of the errors coming from the short-range exchange-correlation LDA and from the missing long-range correlation in the RSH scheme. For the He atom, it is possible to choose a value for the range-separation parameter μ for which these errors compensate each other so as to obtain the exact ionization energy.

We have studied the differences between using the long-range HF exchange nonlocal potential and the long-range EXX local potential. Contrary to the former, the latter supports a series of Rydberg states and the corresponding RSH-EXX scheme, even without applying linear-response theory, gives reasonable photoexcitation/photoionization spectra. Nevertheless, the most accurate spectra are obtained with linear-response TDRSH (or TDRSH-EXX since they are equivalent for one- and two-electron systems). In particular, for the He atom at the optimal value of μ, TDRSH gives slightly more accurate photoexcitation and photoionization spectra than standard TDHF.

The present work calls for further developments. First, the merits of TDRSH (and/or TDRSH-EXX) for calculating photoexcitation/photoionization spectra of larger atoms and molecules, where screening effects are important, should now be investigated. Second, it would be interesting to test the effects of going beyond the LDA for the short-range exchange-correlation functional [Toulouse 05, Goll 06] and adding long-range wave-function correlation [Fromager 13, Hedegard 13, Rebolini 16]. Third, time-propagation TDRSH could be implemented to go beyond linear response and tackle strong-field phenomena, such as high-harmonic generation and above-threshold ionization [Labeye 18].

CHAPTER 5

Optimal basis set for strong laser fields

In this chapter we have reproduced our article titled *"On the optimal basis set for electron dynamics in strong laser fields: The case of molecular ion H_2^+"*, published in *J. Chem. Theory Comput.* **14**, *11, 5846-5858 (2018)* [Labeye 18]. This work was realized in collaboration with Dr. Richard Taïeb's group at the Laboratoire de Chime-Physique Matière et Rayonnement (Sorbonne Université - CNRS), Dr. Emanuele Coccia at the Dipartimento di Scienze Chimiche e Farmaceutiche (Università di Trieste) and Dr. Valérie Véniard at the Laboratoire des Solides Irradiés (École Polytechnique).

Today, a clear understanding of the mechanisms that control the electron dynamics in strong laser field is still a challenge that requires to be interpreted by advanced theory. Development of accurate theoretical and computational methods, able to provide a precise treatment of the fundamental processes generated in the strong field regime, is therefore crucial. A central aspect is the choice of the basis for the wavefunction expansion. Accuracy in describing multiphoton processes is strictly related to the intrinsic properties of the basis, such as numerical convergence, computational cost, and representation of the continuum. By explicitly solving the 1D and 3D time-dependent Schrödinger equation for H_2^+ in presence of an intense electric field, we explore the numerical performance of using a real-space grid, a B-spline basis, and a Gaussian basis (improved by optimal Gaussian functions for the continuum). We analyze the performance of the three bases for high-harmonic generation and above-threshold ionization for H_2^+. In particular, for high-harmonic generation, the capability of the basis to reproduce the two-center interference and the hyper-Raman phenomena is investigated.

5.1 INTRODUCTION

The optical response of a molecular system to an intense and ultrashort laser pulse is a subject of increasing interest since the advent of the attosecond laser pulses [Chini 14]. Recent advances in laser technology are continuously triggering the introduction of new time-resolved spectroscopies, offering the opportunity to investigate electron dynamics in molecules with unprecedented time resolution [Krausz 14]. For example, electronic charge migrations have been traced in molecules using attosecond pulses [Lépine 14], electron correlation effects have been also observed in photoemission processes on the attosecond scale [Ossiander 17, Bergues 12] and above-threshold ionization (ATI) together with high-harmonic generation (HHG) spectra have been used to explain the attosecond dynamics of electronic wave packets in molecules [Nisoli 17, Haessler 10].

Despite these exciting experimental achievements, reaching a clear understanding of the mechanisms that control the electron dynamics under the action of a strong laser field is still a challenge that requires theoretical support [Nisoli 17]. It is crucial to develop accurate theoretical and computational methods capable to provide precise treatments of the fundamental processes generated by a strong laser field [Palacios 15, Telnov 07, Lee 08, Madsen 07].

Nowadays, the electron dynamics problem in strong fields is tackled by two main families of methods: time-dependent density-functional theory (TDDFT) and time-dependent wave-function methods [Nisoli 17, Coccia 16b, Gao 17, Liu 16, Ulusoy 11, Chu 05]. With these methods, developments have been focused on the accurate description of electron correlation. However, because of the complexity of nonlinear optical phenomena, such as HHG and ATI, another important aspect needs to be carefully addressed: the choice of the one-electron basis for representing the time-dependent wave function. In fact, a reliable description of the electron dynamics in strong laser fields depends on the accuracy in reproducing the bound states and, even more important, the continuum states of the molecular system considered. In addition, choosing a good basis can improve the numerical convergence of the results and reduce the computational cost of simulations.

Most of the proposed numerical methods in literature directly describe the system wave function on a real-space grid [Krause 92, Wassaf 03, Ruiz 06, Sawada 16] or through a numerically defined grid-based basis set of functions, as in the case of the discrete-variable representation method [Tao 09], the pseudospectral grid method, or the finite-element method [Pabst 16]. Within these approaches, schemes have been proposed to compute ATI spectra in molecules [De Giovannini 12] and to study the different molecular orbital contributions to HHG spectra [Chu 16, Wang 17].

Grid-based basis sets have demonstrated to be very accurate to describe nonlinear optical phenomena. However, the computational cost can be very high and strategies involving multi-level parallelization schemes have had to be developed [Andrade 15].

Another recurrent basis, in the context of ultrafast electron dynamics, is composed by B-splines, defined as piecewise polynomial functions with compact support [de Boor 78]. They were first introduced in atomic calculations by Shore [Shore 73] and later extensively used to treat ionized and excited states [Fischer 89, Fischer 90]. B-splines have proved to be a very powerful tool to describe multiphoton ionization processes in atoms and molecules in the frameworks of TDDFT and wave-function methods [Martín 99, Bachau 01, Cormier 97, Stener 07]. The success of B-splines is due to a remarkable feature: B-splines are able to reproduce accurately both bound and continuum states. This numerical property is directly related to their effective completeness [Argenti 09]. Nowdays atomic packages based on B-splines are available [Fischer 11, Nikolopoulos 03, Nepstad 10] and recent studies show their ability to reproduce HHG and ATI spectra of molecules under the action of a strong laser field [Fetic 17]. However, new algorithms have to be developed in order to increase the computational efficiency of complex calculations with B-splines.

More recently, Gaussian-type orbital functions (abbreviated as Gaussian functions in the following), in the framework of the time-dependent configuration-interaction (TDCI) method, have been used to calculate HHG spectra in atoms and molecules [Coccia 16b, Luppi 13, White 16, Coccia 16a, Luppi 12]. The importance of the cardinal number (related to the maximal angular momentum) of the basis set and the number of diffuse basis functions was investigated [Coccia 16b, Luppi 12]. Two strategies to improve continuum states have been studied: multi-centered basis functions [White 16, Coccia 16a] and, alternatively, Gaussian functions with exponents specially optimized to improve the continuum [Coccia 16b, Coccia 17]. This latter strategy proved to be more efficient than using multi-centered basis functions and it has also lower computational cost, however it remains to be tested on molecular systems. These works permitted us to identify the best basis sets to be used in order to capture the features of HHG spectra.

Finally, to overcome some of the limitations of the grid, B-spline, and Gaussian basis, hybrid approaches have been proposed in the last years. For example, Gaussian functions were used together with grid-based functions to reproduce electron dynamics in molecular systems [Yip 14], and also Gaussian functions have been combined with B-splines for studying ionization in H and He atoms [Marante 14, Marante 17].

The aim of the present work is to compare the performance of the three families of basis, briefly reviewed above, i.e. grid, B-splines, and Gaussians, for the calculation of HHG and ATI spectra of the molecular ion H_2^+. This system has been chosen because it has the advantage of having only one electron, which allows us not to bias our investigation with possible effects due to electron correlation. Indeed, with this simple case, we can focus on the effectiveness of the representation of the continuum states for the electron dynamics and the computational advantages of each basis. Moreover, the presence of two nuclei in H_2^+ offers the opportunity to observe intricate physical features, such as quantum interferences in the HHG process [Wörner 10, Picón 11, Lein 02].

This article is organized as follows. In Section 5.2 we present the 1D theoretical model to solve the electronic time-dependent Schrödinger equation (TDSE) with grid, B-spline, and Gaussian bases. In Section 5.3 we present and discuss the results for the 1D approach. In Section 5.4 we present the 3D theoretical model to solve the electronic TDSE with grid and Gaussian basis. In Section 5.5 we present and discuss the results for the 3D approach. We compare the bound and the continuum energy spectra of H_2^+, as well as HHG and ATI spectra for grid, B-spline, and Gaussian bases, emphasizing the advantages and disadvantages of each representation. In particular, for HHG spectra, we investigate the capability of the different basis to reproduce specific quantum features, such as the hyper-Raman [Millack 93] and the the two-center interference phenomena [Wörner 10, Picón 11, Lein 02]. Finally, Section 5.6 contains our conclusions.

5.2 1D THEORETICAL MODEL OF H_2^+

The electronic TDSE for a 1D model of H_2^+ is given by, in atomic units (au),

$$i\frac{\partial}{\partial t}\psi(x,t) = \left[\hat{H}_0(x) + \hat{H}_{\text{int}}(x,t)\right]\psi(x,t), \tag{5.1}$$

where $\psi(x,t)$ is the time-dependent electron wave function. Here, $\hat{H}_0(x)$ is the field-free Hamiltonian,

$$\hat{H}_0(x) = -\frac{1}{2}\frac{\mathrm{d}^2}{\mathrm{d}x^2} + \hat{V}(x), \tag{5.2}$$

with a soft Coulomb electron-nuclei interaction given by

$$\hat{V}(x) = -\frac{1}{\sqrt{\left(x - \frac{R}{2}\right)^2 + \alpha}} - \frac{1}{\sqrt{\left(x + \frac{R}{2}\right)^2 + \alpha}}, \tag{5.3}$$

where R is the interatomic distance and α is a parameter chosen to reproduce the exact ionization energy I_p (taken as -1.11 Ha for all the three bases employed here) of the real H_2^+ molecule at a given value of R ($\alpha = 1.44$ at $R = 2.0$ au) [Lein 02].

The interaction between the electron and the laser electric field $E(t)$ is taken into account by the time-dependent interaction potential, which is given in the length gauge by

$$\hat{H}_\mathrm{int}(x,t) = \hat{x}E(t), \tag{5.4}$$

where $E(t)$ is the laser electric field and $\hat{x}$ is the electron position operator. The laser electric field is chosen as $E(t) = E_0 f(t)\sin(\omega_0 t)$ where E_0 is the maximum amplitude of the pulse, ω_0 is the carrier frequency, and $f(t)$ is a trapezoidal envelope

$$f(t) = \begin{cases} t/T_0, & 0 \leq t < T_0 \\ 1, & T_0 \leq t < T_0 \\ 10 - t/T_0 & 9T_0 \leq t < 10T_0 \end{cases}, \tag{5.5}$$

with $T_0 = 2\pi/\omega_0$. The duration of the pulse is thus $\tau = 10T_0$ (i.e., 10 optical cycles).

5.2.1 HHG and ATI spectra

A HHG spectrum, experimentally accessible by measuring the emission spectrum in the presence of an intense laser field, can be calculated as the acceleration power spectrum over the duration of the laser pulse τ [Burnett 92]

$$P_\mathrm{a}(\omega) = \left| \int_0^\tau \left\langle \psi(t) \right| - \nabla\hat{V} - E(t) \left| \psi(t) \right\rangle W(t) e^{-i\omega t} \mathrm{d}t \right|^2, \tag{5.6}$$

where $-\nabla\hat{V} - E(t)$ is the electron acceleration operator, as defined by the Ehrenfest theorem, and $W(t)$ is an apodisation function that we chose to be of the sine-square window form. An alternative way to obtain the HHG spectrum is to calculate the dipole power spectrum as

$$P_\mathrm{x}(\omega) = \left| \int_0^\tau \langle \psi(t) | \hat{x} | \psi(t) \rangle W(t) e^{-i\omega t} \mathrm{d}t \right|^2, \tag{5.7}$$

It can be shown that the two forms are related [Burnett 92, Bandrauk 09, Han 10, Coccia 16b], $\omega^4 P_{\mathrm{x}}(\omega) \approx P_{\mathrm{a}}(\omega)$, under reasonable conditions (see appendix in Ref. [Coccia 16b]). The function $W(t)$ is a sin-square window function chosen empirically to minimise the noise, and especially to remove the artefacts arising from the discrete Fourier transform due to the fact that we integrate only over a limited time duration and not from $-\infty$ to $+\infty$.

An ATI spectrum, which is experimentally accessible by measuring the photoelectron spectrum of the molecule, can be calculated by spectrally analyzing the system wave function $\psi(\tau)$ at the time τ corresponding to the end of the laser pulse. Specifically, using the window operator method, one calculates the probability $P(E, n, \gamma)$ to find the electron in the energy interval $[E-\gamma, E+\gamma]$ as [Schafer 91][1]

$$P(E, n, \gamma) = \left\langle \psi(\tau) \left| \frac{\gamma^{2^n}}{(\hat{H}_0 - E)^{2^n} + \gamma^{2^n}} \right| \psi(\tau) \right\rangle, \tag{5.8}$$

where γ and n are parameters chosen to allow flexibility in the resolution and accuracy of the energy analysis. In our case we chose $n = 2$ and $\gamma = 2 \times 10^{-3}$ au.

5.2.2 Representation of the time-dependent wave function

5.2.2.1 Real-space grid

The time-dependent wave function is discretized on a real-space grid of N points x_i separated by a constant step $\Delta x = x_{i+1} - x_i$, in the interval $[x_1 = -(N-1)\Delta x/2, x_N = (N-1)\Delta x/2]$. It is thus represented by the vector

$$\psi(x, t) \equiv (\psi(x_1, t), \ldots, \psi(x_i, t), \ldots, \psi(x_N, t)), \tag{5.9}$$

where $x_i = (i - 1 - (N-1)/2)\Delta x$.

The Laplacian operator is computed with the second-order central difference formula which gives rise to a tridiagonal matrix representation of the Hamiltonian $\hat{H}_0$ [Krause 92]. The TDSE (Eq. (5.1)) is solved by means of the Crank-Nicholson

---

[1] For the grid and B-spline basis sets, the ATI signal was evaluated following the approach explicitly given in Ref. [Schafer 91]. We compute $P(E, n = 2, \gamma) = \langle \psi(\tau) | \gamma^4 / [(\hat{H}_0 - E)^4 + \gamma^4] | \psi(\tau) \rangle = gamma^4 \langle \chi | \chi \rangle$, where $|\chi\rangle$ is defined in Eq. (2) of Ref. [Schafer 91]: $(\hat{H}_0 - E + \sqrt{i}\gamma)(\hat{H}_0 - E - \sqrt{i}\gamma)|\chi\rangle = |\psi(\tau)\rangle$. Then $P(E, n = 2, \gamma) = \gamma^4 \langle \chi | \chi \rangle$ is directly obtained from the norm of $|\chi\rangle$. For the Gaussian basis sets, the wave function is expressed in a orbital basis for which the window operator of Eq. (5.8) is diagonal. We thus simply evaluate $P(E, n = 2, \gamma) = \sum_j |c_j|^2 \gamma^4 / [(E_j - E)^4 + \gamma^4]$, where j runs over the (discrete) states from the quantum chemistry calculation.

propagation algorithm [Crank 47]. The H_2^+ ground state, computed by inverse iteration [Press 07], is taken as the initial state for the propagation. In addition, to avoid unphysical reflections at the boundaries of the simulation grid, a mask-type absorber function [Krause 92] was implemented with a spatial extension of 50 au.

For ATI spectra, converged results were obtained with $N = 200001$ and $\Delta x = 0.02$ au, and with a time step $\Delta t = 8.41 \times 10^{-4}$ au. For HHG spectra, we obtained converged results with $N = 160001$, $\Delta x = 0.01$ au, and $\Delta t = 1.35 \times 10^{-2}$ au.

5.2.2.2 B-spline basis set

The time-dependent wave function with the B-spline basis set is represented as

$$\psi(x,t) = \sum_{i=1}^{M} c_i(t) B_i^k(x), \tag{5.10}$$

where $c_i(t)$ are time-dependent coefficients and $\{B_i^k(x)\}$ are a set of B-spline functions of order k and dimension M. To completely define B-spline functions a sequence of knots $\mathbf{t} = \{t_i\}_{i=1,M+k}$ must be given. Each function $B_i^k(x)$ is defined on a supporting interval $[t_i, t_{i+k}]$ which contains $k+1$ consecutive knots, and the function $B_i^k(x)$ vanishes outside this interval. We have chosen the first and the last knots to be k-fold degenerate, $t_1 = t_2 = \cdots = t_k = R_{\text{min}}$ and $t_{M+1} = t_{M+2} = \cdots = t_{M+k} = R_{\text{max}}$, while the multiplicity of the other knots is unity. The width of an interval is $t_{i+1} - t_i = R_{\text{max}}/(M - k + 1)$ [Bachau 01]. In our calculations we used $k = 8$, $M = 15008$, $R_{\text{min}} = 0$, and $R_{\text{max}} = 8000$ au. The system was placed at the center of the box at $x = 4000$ au.

ATI and HHG spectra were obtained by solving the TDSE (Eq. (5.1)) within the Cranck-Nicholson propagation algorithm [Crank 47] using a time step of $\Delta t = 1.35 \times 10^{-2}$ au. The H_2^+ ground state was computed by inverse iteration [Press 07] and taken as the initial state for the propagation. We did not need to use any absorber during the propagation because of the very large size of the simulation box.

5.2.2.3 Gaussian basis set

For the Gaussian basis set we followed the TDCI procedure developed in our previous work [Coccia 16b], and adapted it to the present 1D H_2^+ model. The time-dependent wave function is represented here as

$$\psi(x,t) = \sum_{k\geq 0} c_k(t)\phi_k(x), \tag{5.11}$$

where $\phi_k(x)$ are the eigenstates of the field-free Hamiltonian $\hat{H}_0$, composed by the ground state ($k = 0$) and all the excited states ($k > 0$). The $\phi_k(x)$ are expanded on the Gaussian basis set. In this work, we use uncontracted Gaussians localized on each nucleus and two "angular momenta" (l), corresponding to odd and even functions. The basis functions are thus of the form $(x \pm R/2)^l e^{-\alpha(x\pm R/2)^2}$, where $l = 0$ or 1. The Gaussian exponents α are of two different types. The first type of exponents are optimized to describe the bound part of the wave function. We used the uncontracted STO-3G basis set, i.e. three uncontracted Gaussians whose exponents are taken from the STO-3G basis set with Slater exponent $\zeta = 1$. We take the same exponents for $l = 0$ and $l = 1$. The second type of exponents are optimized for the representation of the continuum [Coccia 16b]. They are computed with the procedure developed by Kaufmann [Kaufmann 89] adapted to the 1D model, i.e. by optimizing the overlap between a 1D Slater type function $N_n^{(S)}(\zeta)x^n e^{-\zeta|x|}$ with $\zeta = 1$ and a Gaussian function $N_l^{(G)}(\alpha_{n,l})x^l e^{-\alpha_{n,l}x^2}$, where $N_n^{(S)}$ and $N_l^{(G)}$ are normalization factors. Note that, in this case, the exponents used for the $l = 0$ shell and for the $l = 1$ shell are different. In the following, we will denote these Gaussian functions optimized for the continuum as K functions. To sum up, we use 3 functions with STO-3G exponents and 4 K functions for each angular momentum, localized on each nucleus, which makes a total of $(3 + 4) \times 4 = 28$ uncontracted Gaussian basis functions. However when we orthonormalize this basis set, we find linear dependencies that needs to be removed. For this we define a cutoff $\epsilon = 10^{-8}$ under which the eigenvalues of the overlap matrix are considered to be zero, and their corresponding eigenvectors are removed from the space. We get an orthonormalized basis set of 24 basis functions. The basis-set exponents are collected in Table S1 of Supporting Information, see for instance Ref. [Labeye 18]. To solve the TDSE (Eq. (5.1)) we used the split-operator propagator with $\Delta t = 1.35 \times 10^{-2}$ au.

In order to compensate for the unphysical absence of ionization, we used the double-d heuristic lifetime model proposed in Ref. [Coccia 16b]. This model requires two parameters: d_0 and d_1 which represent different electron escape lengths after ionization. We have chosen these parameters on the basis of the rescattering model [Corkum 93, Lewenstein 94] where an electron is ionized by a strong laser field, accelerated in the continuum, and then brought back close to its parent ion where it can recombine or scatter. From this model, d_0 is equal to the maximum electron excursion after ionization which is $x_{\max} = \sqrt{2E_0/\omega_0^4}$, while $d_1 < d_0$. In our calculations we always used $d_1 = 20$ au. Moreover d_0 affects all the continuum states below the cutoff energy $E_{\text{cutoff}} = I_{\text{p}} + 3.17U_{\text{p}}$ [Corkum 93, Lewenstein 94] ($U_{\text{p}} = E_0^2/(4\omega_0^2)$ is the ponderomotive energy of the electron) while d_1 handles the ionization for those continuum energy states above E_{cutoff}. This allows to better retain the contribution of continuum states for the recombination step of the HHG process. Table 5.1 collects the values of d_0 used in this work.

Table 5.1: d_0 values, taken as $x_{\max}$, used in the double-d heuristic lifetime model for the laser intensities employed in this work.

I (W/cm^2)	d_0 (au)
5×10^{13}	23
10^{14}	33
2×10^{14}	46
3×10^{14}	57
4×10^{14}	66
5×10^{14}	74
7×10^{14}	87

There is a fundamental difference between this approach and the grid and B-spline ones. Indeed, the TDSE with the Gaussian basis set is solved in the energy space. This fact permits to have a more direct and intuitive interpretation of the role of bound and continuum states in HHG and ATI spectroscopies. In addition, the use of Gaussians reduces considerably the computational time required in time propagation. This makes it a more promising tool for the modelisation of larger molecules.

5.3 1D RESULTS AND DISCUSSION

5.3.1 Spectrum of the field-free Hamiltonian

The spectrum of $\hat{H}_0$ should be strictly independent on the choice of the basis set in the limit of a complete basis set. However, because our basis sets are not complete, differences in the eigenstates and eigenvalues from grid, B-spline, and Gaussian basis sets can arise, especially at high-energy values. In order to investigate the behavior of the three basis sets, the spectrum of $\hat{H}_0$ is analyzed in this section.

In Figure 5.1 the ground-state wave function is shown. The three basis sets reproduce exactly alike the ground state of the 1D H_2^+ model, at the equilibrium internuclear distance of $R = 2.0$ au. The panel (a) of Figure 5.2 shows the eigenvalues given by each basis set up to the 30th energy state, and in panel (b) of Figure 5.2 one finds the inverse of the density of continuum states which is defined as $\rho(E_j) = 1/(E_{j+1} - E_j)$ where E_j is a positive eigenvalue. In order to compare the three bases, the density of the states has been normalized to the length of the simulation box in the case of the grid and B-splines and to a constant in the case of the Gaussians. This constant was chosen to force the first Gaussian continuum eigenvalue to match the first continuum eigenvalue of the grid and B-splines, which are identical. For all the three basis sets, the continuum part of the spectrum is represented as a finite number of eigenstates as, in numerical calculations, the basis set is always incomplete. However, the discreteness of the Gaussians is much larger than that of the grid and B-splines. The spectrum obtained with the Gaussians starts to diverge from the grid and B-spline ones already at around the 13th state. This issue is a direct consequence of the relatively small size of the Gaussian basis set compared to the number of grid points or B-spline functions used. Indeed, the STO-3G+4K basis contains only 24 Gaussian basis functions whereas we used 400001 grid points and 15000 B-splines. In principle, we could increase the number of Gaussians but this will quickly lead to the linear dependency problem. This problem prevents us to use more than a few tens of optimized Gaussian functions. This fact, as we will see in the following sections, can have important consequences on the calculation of HHG and, in particular, of ATI spectra.

To investigate the accuracy of the grid, B-spline, and Gaussian bases in the description of continuum wave functions, we have chosen two different continuum energies, both representative of two different continuum energy regions: low energy ($E = 0.06$ Ha) and high energy ($E = 1.97$ Ha). For each of these energies, we reported in Figure 5.3 the corresponding wave functions $\varphi_E(x)$. For the grid, the continuum wave functions were obtained by propagating the TDSE at the chosen positive energy E with a fourth-order Runge-Kutta algorithm [Press 07], and then

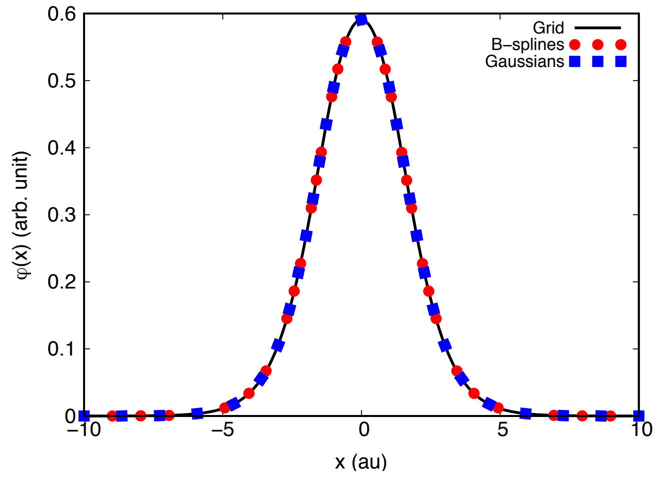

Figure 5.1: Ground-state wave function of H_2^+ (at the equilibrium internuclear distance of $R = 2.0$ au) calculated using grid, B-spline, and Gaussian basis.

normalized with the Strömgren procedure [Seaton 62][2]. Instead, for B-splines and Gaussians, the wave functions were obtained from a direct diagonalisation of $\hat{H}_0$. In this case, the resulting continuum states were renormalized using the procedure proposed by Macías *et al.* [Macías 88][3]. We verified that the Strömgren and Macías procedures are equivalent. The continuum wave functions computed with both grid and B-spline basis sets reproduce the same oscillations in the low- and high-energy regions of the continuum. On the other hand, Gaussians can reproduce just a few of the oscillations. We already observed this behavior in the case of the hydrogen atom in a 3D calculation [Coccia 16b] where the crucial role of the K functions was pointed out in order to obtain these oscillations (in that case a much larger basis set was employed). Here, we want to draw the attention on the fact that Gaussians can still be reasonable in the low-energy continuum, but become unsuitable to reproduce oscillations for high-energy continuum states. The probability of propagating an electron in one of the two regions depends on the laser parameters used in the simulation. This fact can have important implications in the description of HHG and ATI spectra as we will see in the following sections.

---

[2] The Strömgren procedure consists in fitting the asymptotic form of the numerical solution of the Schrödinger equation with the exact solution calculated when $\hat{V}(x) = 0$. This implies that for a specific energy E in the continuum: $\psi(x) = \sin(\theta(x))/\sqrt{2\pi k(x)}$, where $k(x)$ is the electron momentum which is proportional to $\sqrt{2E}$ and it is related to $\theta(x)$ as $k(x) = d\theta(x)/dx$.

[3] The Macías procedure permits to normalise L^2-norm continuum states. In this method, for a specific energy E in the continuum, we have: $\psi(x) = \psi_{L^2}(x)\sqrt{\rho(E)/2}$, where ψ_{L^2} is the L^2-norm normalized state and $\rho(E)$ is the density of states evaluated numerically as the number of states per energy unit as $\rho(E_j) = 2/(E_{j+1} - E_{j-1})$.

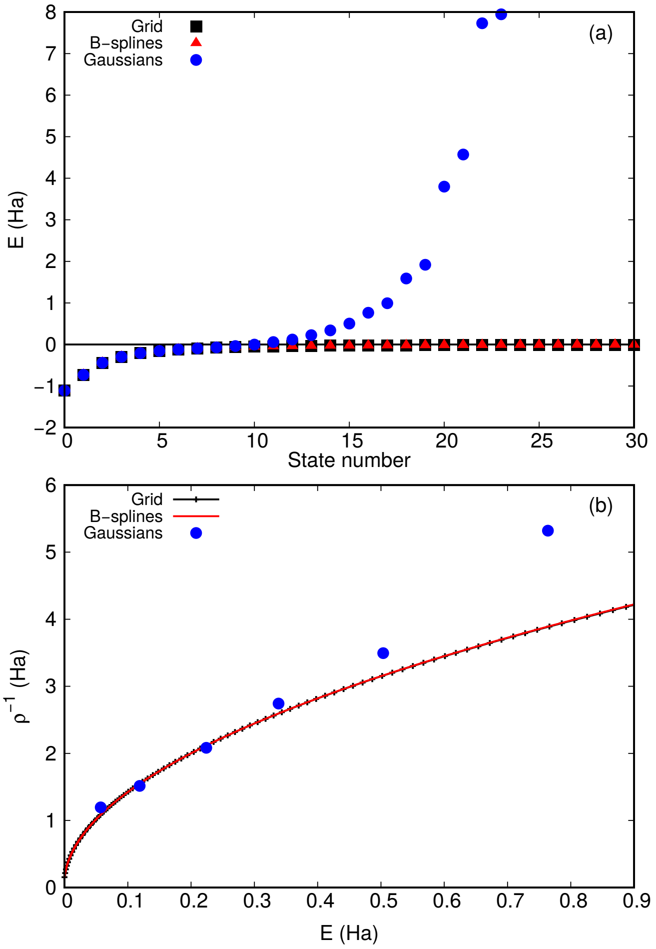

Figure 5.2: (a) Eigenvalues of H_2^+ up to the 30th eigenstate. (b) Inverse of the normalized density of continuum states.

5.3.2 HHG

HHG spectra have been calculated in the dipole and the acceleration forms for H_2^+ at different internuclear distances: $R = 1.8$, $R = 2.0$ (equilibrium distance), and $R = 2.2$ au for a Ti:Sapphire laser pulse with a carrier frequency $\omega_0 = 0.057$ Ha (1.55 eV, 800 nm) and different intensities: $I = 5 \times 10^{13}$, $I = 1 \times 10^{14}$, $I = 2 \times 10^{14}$, $I = 5 \times 10^{14}$, and $I = 7 \times 10^{14}$ W/cm^2.

In Figure 5.4 we show the dipole form of the HHG spectra at $R = 2.0$ au for three different laser intensities. All the three basis sets reproduce the general expected features of an HHG spectrum: the intensity of the low-order harmonics decreases rapidly, then a plateau region follows where the intensity remains nearly constant, and at high frequencies the harmonic intensity decreases again. As H_2^+ has a center-of-inversion symmetry, only odd harmonics are presented in the spectrum. We estimated the cutoff energies by calculating $E_{\mathrm{cutoff}} = I_{\mathrm{p}} + 3.17 U_{\mathrm{p}}$, as given in the semiclassical

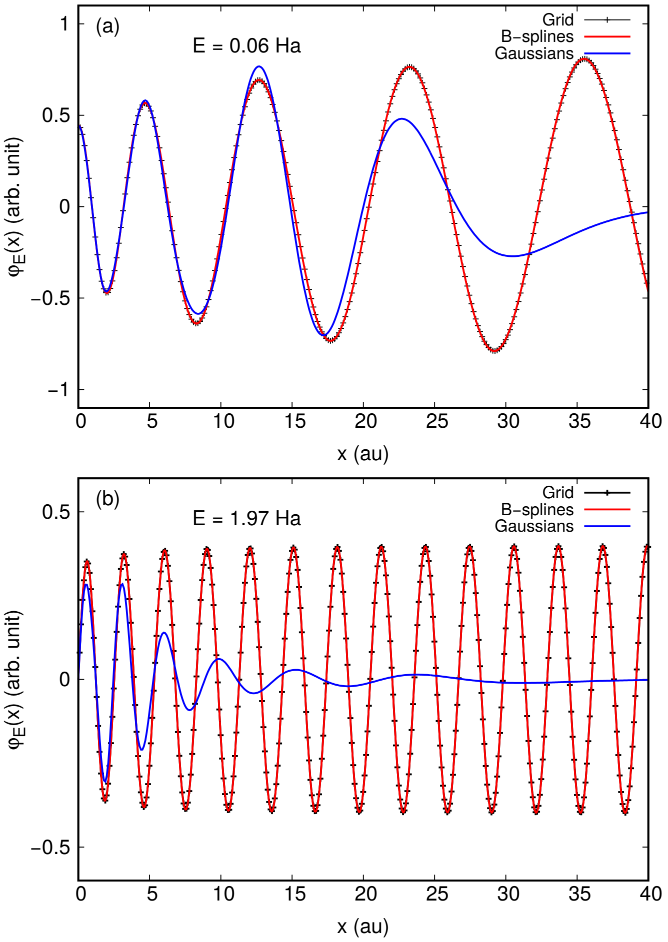

Figure 5.3: (a) Spatial dependence of the even wave function $\varphi_E(x)$ corresponding to $E = 0.06$ Ha. (b) Spatial dependence of the odd wave function $\varphi_E(x)$ corresponding to $E = 1.97$ Ha.

rescattering model [Corkum 93, Lewenstein 94].

We observe that the grid and B-spline HHG spectra are indistinguishable for all the laser intensities. This fact is consistent with the analysis reported above on the spectrum of $\hat{H}_0$ (see Section 5.3.1). On the other hand, the agreement between the spectra obtained with the Gaussian basis and those obtained with the grid or B-splines deteriorates when the laser intensity increases. This is clearly observed for the plateau region for the intensity $I = 5 \times 10^{14}$ W/cm^2, but also detected for the plateau and cutoff regions for the intensity $I = 7 \times 10^{14}$ W/cm^2 (see Supplementary Information). Most of these observations are also valid when using the acceleration form of the HHG spectrum. The only exception we found was with the Gaussian basis set and laser intensities $I = 5 \times 10^{14}$ W/cm^2, as shown in Figure 5.5, and $I = 7 \times 10^{14}$ W/cm^2 (see Supplementary Information [Labeye 18]). For these largest intensities, the spectrum extracted from the acceleration seems to largely underestimate the position of the cutoff but to much better reproduce the harmonics of the plateau.

To analyse in more details the fine structure of the HHG peaks, in Figure 5.6 HHG spectra only up to the 15th harmonics. The B-spline and the grid spectra are almost identical except for some very small differences when the laser intensity is very high. Gaussian spectra reproduces the features of the B-spline and grid ones, but when the laser intensity increases the Gaussian spectrum becomes much more noisy.

From panel (a) of Figure 5.6 it is also possible to identify another series of peaks besides those corresponding to the harmonics. These peaks corresponds to hyper-Raman lines with position given by $\tilde{\omega} \pm 2k\omega_0$ [Gauthey 95], where k is an integer and $\tilde{\omega} = 6.69\omega_0$ is the resonance with the first excited state. We observe that the three basis sets describe with the same accuracy the hyper-Raman lines. Moreover, at sufficiently large laser intensity, the HHG process dominates, and the hyper-Raman lines are not observed anymore (panel (b) of Figure 5.6).

The accuracy of the grid, B-spline, and Gaussian calculations was also investigated through their ability to reproduce the two-center interference in the HHG spectrum. This interference was predicted by Lein *et al.* [Lein 02] for diatomic molecules such as H_2^+. In this model, the electron that recombines with the ionic core can interact with either of the two nuclei. The two atomic centers can therefore be interpreted as coherent point sources and the whole system can be seen as a microscopic analog of Young's two-slit experiment. The light emitted by each nucleus will interfere either constructively or destructively depending on its frequency and the interference pattern will superimpose to the HHG spectrum. Since Lein's model has been proposed, a great number of numerical analyses came forth pointing out the role of the internuclear distance, molecular orientation, recombination to excited states, and laser intensity [Madsen 07, Wörner 10, Han 13, Suárez 17, Chirila 06, Chen 08, Itatani 04, Vozzi 05, Lagmago Kamta 09, Smirnova 09].

According to Lein's model, the position of the minimum in the spectrum is independent from the laser intensity and can be extracted from the analysis of the recombination dipole $d_{\mathrm{rec}}(E) = \langle \varphi_0 | \hat{x} | \varphi_E \rangle$ where φ_0 is the ground state and φ_E is a continuum state at energy E of $\hat{H}_0$. This quantity is plotted in panel (a) of Figure 5.7 for $R = 1.8$ au and in panel (a) of Figure 5.8 for $R = 2.2$ au. For $R = 2.0$ au, we report the recombination dipole in the Supplementary Information [Labeye 18]. The minimum described in the two-center interference corresponds to the energy which makes the recombination dipole vanishing. We found that the corresponding frequency is

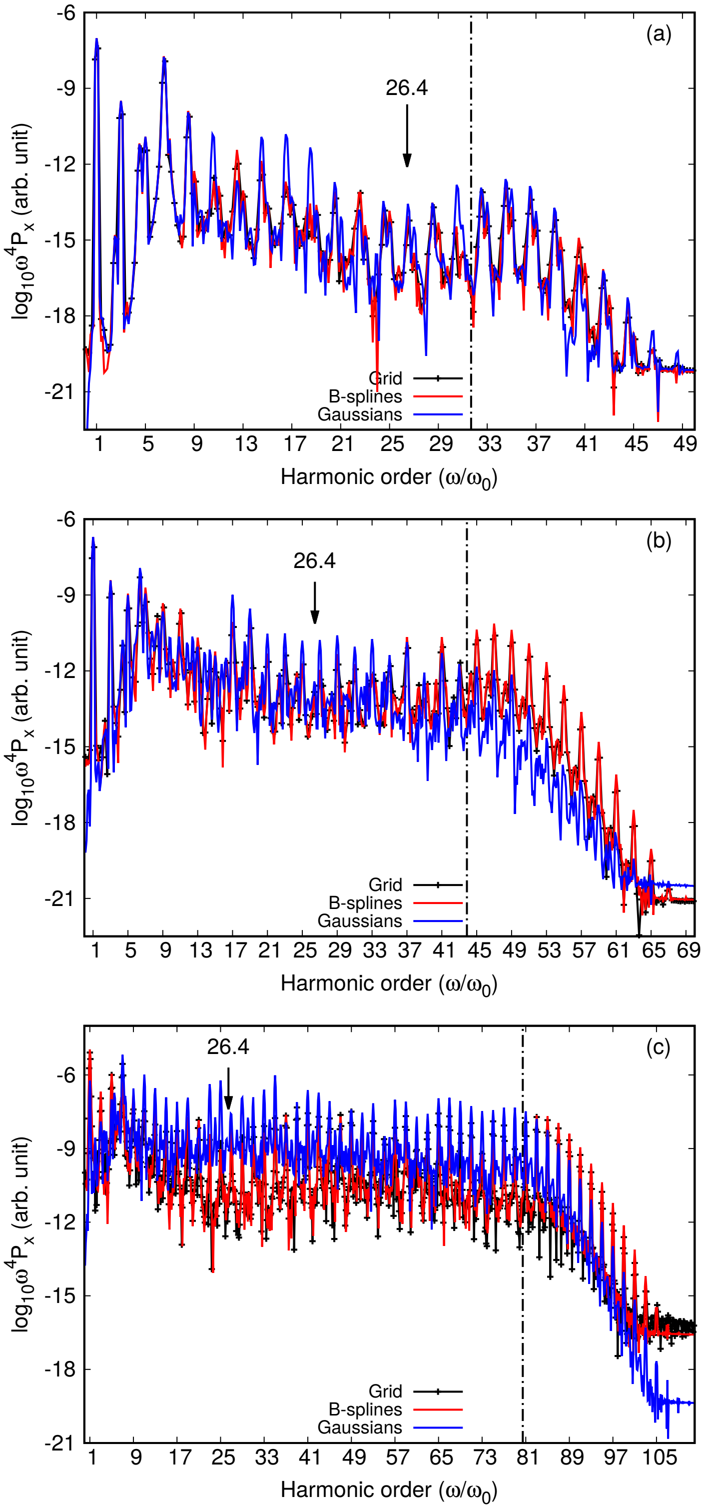

Figure 5.4: HHG spectra calculated from the electron dipole at the equilibrium internuclear distance $R = 2.0$ au with laser intensities: (a) $I = 10^{14}$ W/cm^2, (b) $I = 2 \times 10^{14}$ W/cm^2, and (c) $I = 5 \times 10^{14}$ W/cm^2. Intensities $I = 5 \times 10^{13}$ and 7×10^{14} W/cm^2 are reported in the Supplementary Information [Labeye 18]. For each HHG spectrum, the dot-dashed lines indicate the cutoff energies, which are given by the rescattering model as $E_{\text{cutoff}} = I_{\text{p}} + 3.17U_{\text{p}}$, see Ref. [Corkum 93, Lewenstein 94]: (a) $E_{\text{cutoff}} = 31.7\omega_0$, (b) $E_{\text{cutoff}} = 43.9\omega_0$, and (c) $E_{\text{cutoff}} = 80.5\omega_0$. The arrow points to the expected position of the two-center interference minimum extracted from the recombination dipole.

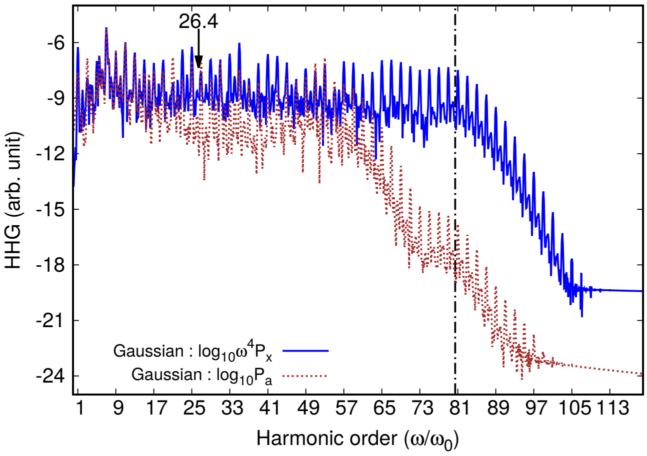

Figure 5.5: HHG spectra calculated from the electron dipole and the electron acceleration at the equilibrium internuclear distance of $R = 2.0$ au with a laser intensity of $I = 5 \times 10^{14}$ W/cm^2 using Gaussian basis sets. The dot-dashed line is the cutoff energy $E_{\text{cutoff}} = 80.5\omega_0$ and the arrow points to the expected position of the two-center interference minimum, extracted from the recombination dipole which is identical to the one extracted from the recombination acceleration.

$\omega = 34.0\omega_0$ for $R = 1.8$ au, $\omega = 26.4\omega_0$ for $R = 2.0$ au, and $\omega = 20.8\omega_0$ for $R = 2.2$ au. We note that the extraction of the minimum from the recombination dipole is straightforward for the grid and B-spline basis sets, while in the case of the Gaussian basis only a rough estimate can be given. Lein's model predicts the position of the minimum at $\omega = \pi^2/(2R^2\omega_0)$ which gives $\omega = 26.7\omega_0$ for $R = 1.8$ au, $\omega = 21.6\omega_0$ for $R = 2.0$ au, and $\omega = 17.9\omega_0$ for $R = 2.2$ au. The underestimation of the minimum position by Lein's model has already been pointed out [Chirila 06]. The main reasons must be searched in the different description of the ground state and the continuum between our 1D theoretical model and Lein's model.

We report in panel (b) of Figure 5.7 and in panel (b) of Figure 5.8 the HHG spectra for $R = 1.8$ au and for $R = 2.2$ au with $I = 2 \times 10^{14}$ W/cm^2 and we observe that all the basis sets reproduce the position of the minimum of the two-center interference. Also the minimum for $R = 2.0$ au is very well reproduced as can be seen in Figure 5.4. Another observation is that the sharpness of the minimum depends on the laser intensity and on the internuclear distance. We confirm the fact that the minimum is more visible for smaller internuclear distances [Risoud 17]. We did the same investigation considering the recombination acceleration $a_{\text{rec}}(E) = \langle\varphi_0| - \nabla\hat{V}|\varphi_E\rangle$ and the HHG spectrum from the acceleration. We obtained the same results (see Supplementary Information [Labeye 18]) explained before. From these studies we deduce that all the basis sets are capable to accurately reproduce

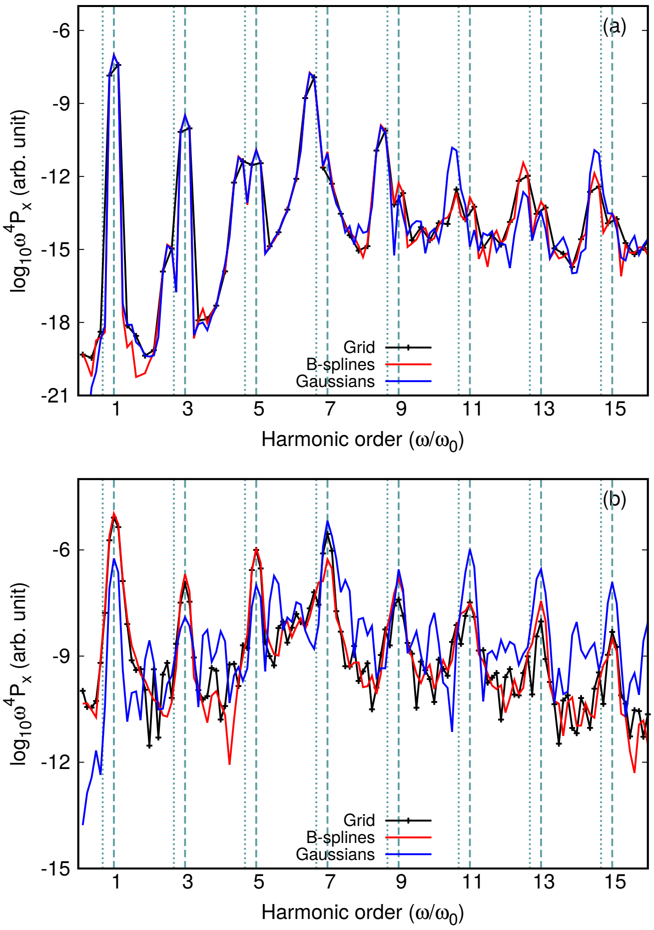

Figure 5.6: HHG spectra calculated from the electron dipole at the equilibrium internuclear distance $R = 2.0$ au up to the 15th harmonic with laser intensities: (a) $I = 10^{14}$ W/cm^2 and (b) $I = 5 \times 10^{14}$ W/cm^2. The dashed lines indicate the position of the harmonics while the dotted lines indicate the hyper-Raman lines at position $\tilde{\omega} \pm 2k\omega_0$ [Gauthey 95] where k is an integer and $\tilde{\omega} = 6.69\omega_0$ is the resonance with the first excited state.

the two-center interference [Lein 02]. However, in the case of the Gaussian basis, the acceleration seems to better reproduce the minimum for $I = 5 \times 10^{14}$ W/cm^2 (panel (c) of Figure 5.5) and $I = 7 \times 10^{14}$ W/cm^2 (see Supplementary Information [Labeye 18]).

From the detailed analysis of HHG spectra presented in this section, we conclude that for a good performance of the Gaussian basis the laser intensity cannot be "very large". For example, for intensity lower than $I = 5 \times 10^{14}$ W/cm^2 we obtain correct HHG spectra while for higher intensities only the harmonic peaks in the low-energy part of the plateau are correct. A strategy to improve the Gaussian basis set could be to modify the cutoff ϵ below which the eigenvalues of the overlap matrix are set to zero. This will change the number of kept eigenvectors. In Figure 5.9 we compare an HHG spectrum for $I = 5 \times 10^{13}$ W/cm^2 calculated with the grid and with the Gaussian basis while changing the linear-dependency threshold ϵ: $\epsilon = 10^{-4}$ (17 basis

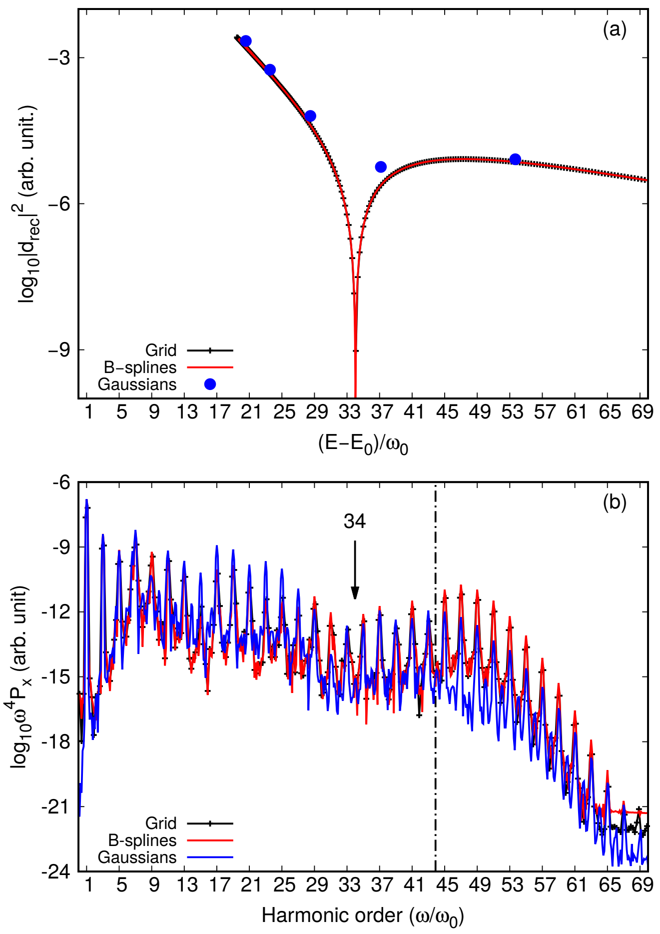

Figure 5.7: Two-center interference at $R = 1.8$ au: (a) recombination dipole and (b) HHG spectrum at $I = 2 \times 10^{14}$ W/cm^2. The arrow points to the expected position of the two-center interference minimum extracted from the recombination dipole. The dot-dashed line is the cutoff energy $E_{\text{cutoff}} = 43.8\omega_0$. E_0 is the ground-state energy.

functions), $\epsilon = 10^{-8}$ (24 basis functions, which is the standard choice throughout the article), and $\epsilon = 10^{-10}$ (26 basis functions). This analysis shows that for a "low" intensity ($I = 5 \times 10^{13}$ W/cm^2) the quality of the HHG spectrum in the plateau and cutoff regions is not affected by the specific choice of the threshold of eigenvalues.

5.3.3 ATI

We calculated ATI spectra with intensities $I = 5 \times 10^{13}$, 1×10^{14}, and 5×10^{14} W/cm^2. In panel (a) of Figure 5.10 we show the ATI spectrum with laser intensity $I = 10^{14}$ W/cm^2, while the spectra for intensities $I = 5 \times 10^{13}$ and 5×10^{14} W/cm^2 are reported in the Supplementary Information [Labeye 18].

The ATI spectrum of Figure 5.10 has positive energy peaks (bound-continuum transitions) corresponding to the electron density ionized during the propagation, i.e. the photoelectron spectrum, while the peaks in the negative region (bound-bound

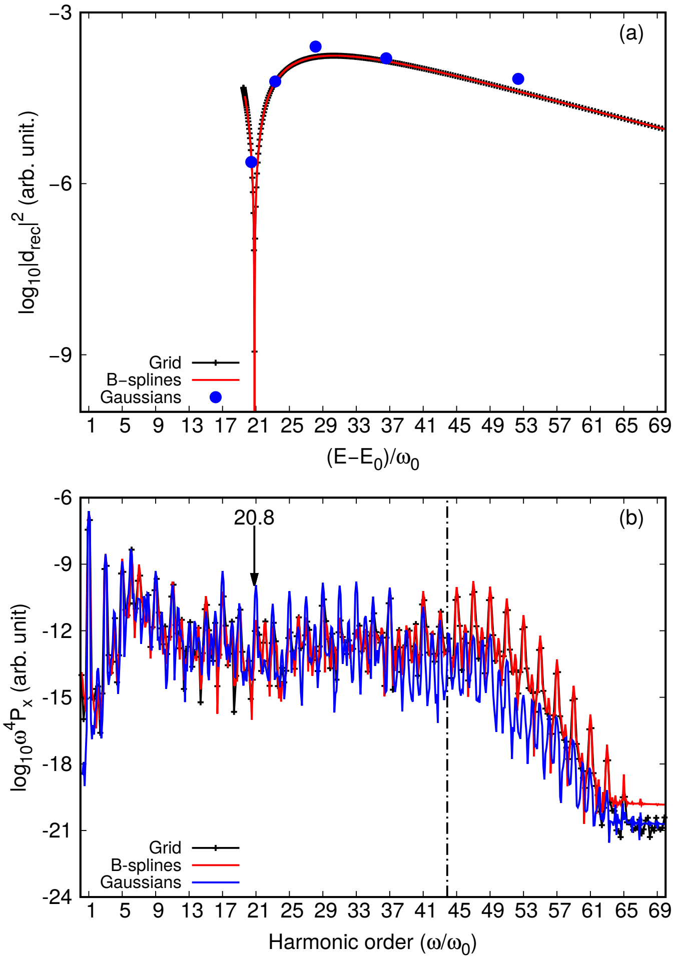

Figure 5.8: Two-center interference at $R = 2.2$ au: (a) recombination dipole and (b) HHG spectrum at $I = 2 \times 10^{14}$ W/cm^2. The arrow points to the expected position of the two-center interference minimum extracted from the recombination dipole. The dot-dashed line is the cutoff energy $E_{\text{cutoff}} = 43.8\omega_0$. E_0 is the ground-state energy.

transitions) represent the electron density remaining in the ground state and that has been transferred to excited states. We remind that only the positive energy region of an ATI spectrum is experimentally measurable.

As already seen for the HHG spectra, the grid and B-spline basis sets describe with the same accuracy both bound-bound and bound-continuum transitions. Their ATI spectra coincide and correctly reproduce the expected features of an ATI spectrum: the distance between two consecutive ATI peaks (in the positive energy region) is constant and equal to the energy of a photon, i.e. 0.057 Ha.

The Gaussian basis is only able to reproduce bound-bound transitions. The negative energy part of the spectrum is quite close to the one obtained with the grid and B-splines, while bound-continuum transitions are out of reach for the Gaussian basis set. This limitation is due to the low density of states in the continuum. Indeed, with the basis-set parameters used here, only six continuum states are reproduced in the

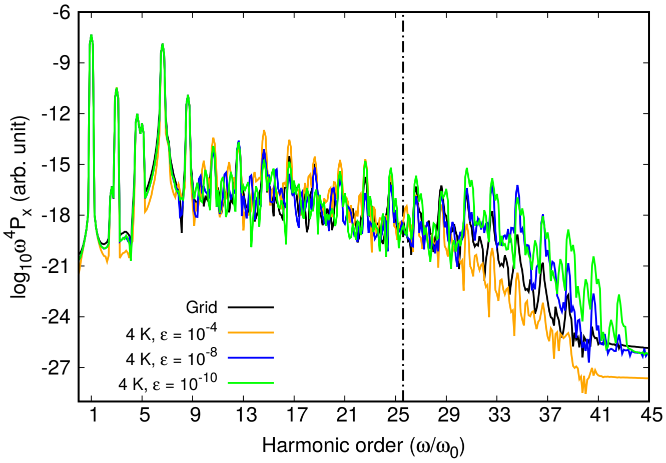

Figure 5.9: HHG spectra from the dipole at the equilibrium internuclear distance $R = 2.0$ au with $I = 5 \times 10^{13}$ W/cm^2 obtained with the grid and with the Gaussian basis sets with linear-dependency thresholds $\epsilon = 10^{-4}$, $\epsilon = 10^{-8}$, and $\epsilon = 10^{-10}$.

energy region between 0 and 1 Ha, as we can see in the bottom panel of Figure 5.2. This low density of states is far from reproducing the correct ATI energy distribution and explains why no more than six peaks are observed in the positive energy region of the spectrum. The energies of the six ATI peaks correspond to the energies of the six continuum states reported in Figure 5.2. To detail more on this feature, we plot in panel (b) of Figure 5.10 the photoelectron spectrum, computed with the Gaussian basis, after absorption of one photon and for three different photon energies $\omega_0 =$ 1.34 Ha, $\omega_0 = 1.47$ Ha, and $\omega_0 = 1.61$ Ha. Together, we also plot the energy position of the ground state and of the first continuum energies corresponding to symmetry-allowed transitions. One clearly sees that if the photon energy matches the energy of a transition from the ground state to one of the continuum states then we get a photoelectron peak. However, if the photon energy does not match any transition then no ionization is observed. This crucial feature forbids the computation of a correct photoelectron or ATI spectrum with the Gaussians basis set used here. We believe that larger Gaussian basis sets can in principle describe ATI. Indeed, in 3D calculations [Coccia 16b], one can easily produce tens of low-energy (<1 Ha) continuum states, leading to a possible improvement of the ATI spectrum.

5.4 3D THEORETICAL MODEL OF H$_2^+$

The electronic TDSE for a 3D model of H$_2^+$ is given by, in atomic units (au),

$$i\frac{\partial}{\partial t}\psi(\mathbf{r},t) = \left[\hat{H}_0(\mathbf{r}) + \hat{H}_{\text{int}}(\mathbf{r},t)\right]\psi(\mathbf{r},t), \tag{5.12}$$

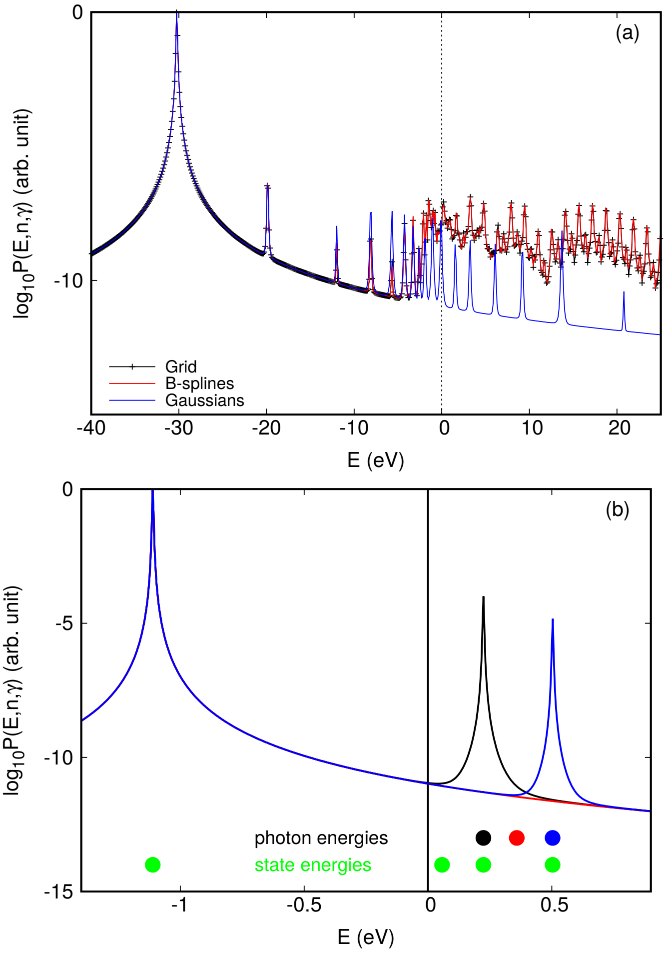

Figure 5.10: (a) ATI spectrum calculated at the equilibrium interatomic distance $R = 2.0$ au with intensity $I = 1 \times 10^{14}$ W/cm^2. (b) Photoelectron spectrum calculated with the Gaussian basis at the equilibrium distance $R = 2.0$ au with intensity $I = 1 \times 10^{14}$ W/cm^2 and three photon energies $\omega_0 = 1.34$ Ha (black), $\omega_0 = 1.47$ Ha (red), and $\omega_0 = 1.61$ Ha (blue). The ground-state energy (-1.11 Ha) and the continuum-state energies (0.06 Ha, 0.22 Ha, and 0.50 Ha) which correspond to transitions allowed by symmetry are displayed (magenta dots).

where $\psi(\mathbf{r}, t)$ is the time-dependent electron wave function. Here, $\hat{H}_0(\mathbf{r})$ is the field-free Hamiltonian,

$$\hat{H}_0(\mathbf{r}) = -\frac{1}{2}\nabla^2 + \hat{V}(\mathbf{r}), \tag{5.13}$$

with $\hat{V}(\mathbf{r})$ the Coulomb electron-nuclei interaction.

The interaction between the electron and the laser electric field $E(t)$ is taken into account by the time-dependent interaction potential, which is given in the length gauge by

$$\hat{H}_{\text{int}}(\mathbf{r}, t) = \hat{z}E(t), \tag{5.14}$$

where $E(t)$ is the laser electric field polarized along the z axis, corresponding to the H_2^+ internuclear axis, and $\hat{z}$ is the electron position operator along this axis. We have chosen the same type of laser as in the 1D model (see Section 5.2) except that the duration of the pulse is $\tau = 6T_0$ (i.e., 6 optical cycles). We calculated HHG spectra from the dipole as in Eq. (5.7).

5.4.1 Representation of the time-dependent wave function

5.4.1.1 Real-space grid

Concerning the 3D calculations on a grid, we used the Octopus code which is a software package for TDDFT calculations [Andrade 15]. For our calculations we have chosen the "independent particle" option which permits to get the numerically exact solution for the TDSE in the case of one electron. We have chosen as simulation box a cylinder with radius 50 au and height 100 au with a grid space $\Delta r = 0.435$ au. The TDSE of Eq. (5.12) is solved by means of the Crank-Nicholson propagation algorithm [Crank 47, Press 07] with a time step $\Delta t = 5 \times 10^{-2}$ au. Also in this case to avoid unphysical reflections at the boundaries of the simulation box, a mask-type absorber function was used with a spatial extension of 22 au.

5.4.1.2 Gaussian basis set

In this case, we used the approach we developed and detailed in Ref. [Coccia 16b, Luppi 13] which consists in solving the TDSE using the TDCI approach. For the Gaussian calculations, we used a development version of the MOLPRO software package [Werner 15] and the external code LIGHT [Luppi 13] to perform the time propagation using also in this case a time step $\Delta t = 5 \times 10^{-2}$ au. As Gaussian basis set we used a 6-aug-cc-pVTZ with 5 K functions, which we denote as 6-aug-cc-pVTZ+5K, which is the largest basis without linear dependencies. The basis-set exponents and contraction coefficients are collected in Table S2 of Supporting Information [Labeye 18]. To treat ionization we used a double-d heuristic model where the parameters d_1 and d_0 have been chosen as in the 1D model. The value of I_p is in this case -1.10 Ha.

5.5 3D RESULTS AND DISCUSSION

5.5.1 HHG

We calculated HHG spectra in the dipole form for H_2^+ at internuclear distance $R = 2.0$ au (equilibrium) for a Ti:Sapphire laser with a carrier frequency $\omega_0 = 0.057$ Ha and intensities $I = 5 \times 10^{13}$, 1×10^{14}, 2×10^{14}, 3×10^{14}, 4×10^{14}, and 5×10^{14} W/cm^2.

In Figure 5.11 we show the HHG spectra for three laser intensities (the spectra for the other intensities are reported in the Supplementary Information). Both the Gaussian and grid basis sets reproduce well the expected features of an HHG spectrum, regardless of the applied field intensity, as already pointed out for the 1D case. However, starting from intensity $I = 3 \times 10^{14}$ W/cm^2, the quality of the spectrum obtained with the Gaussian basis set tends to diminish, especially in the cutoff region. For 3D calculations, obtaining a good HHG spectrum with optimized Gaussians seems to be more difficult than for 1D calculations, due to the computational complexity.

However, it is interesting to note that the low-energy harmonics are still well described when compared to the grid calculations. We show this behavior by analysing the fine structures of the peaks as shown in Figure 5.12. Here, we plot the HHG spectra up to the 13th harmonic for different intensities. For the grid calculations (panel (a)) with $I = 5 \times 10^{13}$ W/cm^2 only the first and the third harmonic peaks are clearly visible together with a strong and large peak at around $7.65\omega_0$, due to the emission from the first excited state. Also in this case we observe hyper-Raman lines at position $\tilde{\omega} \pm 2k\omega_0$ [Gauthey 95] where k is an integer and $\tilde{\omega} = 7.65\omega_0$ is the resonance with the first excited state. Observing the evolution of the harmonics and the resonant peaks as a function of the laser intensity (from $I = 5 \times 10^{13}$ W/cm^2 to $I = 5 \times 10^{14}$ W/cm^2), the harmonics become more and more intense while the hyper-Raman lines almost disappear. The same behaviour was already observed in the 1D model. The spectra obtained with the Gaussian basis set show exactly the same trend as shown in panel (b) of Figure 5.12.

5.6 CONCLUSIONS

We explicitly solved the 1D and 3D TDSE for H_2^+ in the presence of an intense electric field and we explored the numerical performance of using a real-space grid, a B-spline basis, or a Gaussian basis optimized for the continuum. We analyzed the performance of the three basis sets for calculating HHG and ATI spectra. In particular, for HHG, the capability of the basis set to reproduce the two-center interference and the hyper-

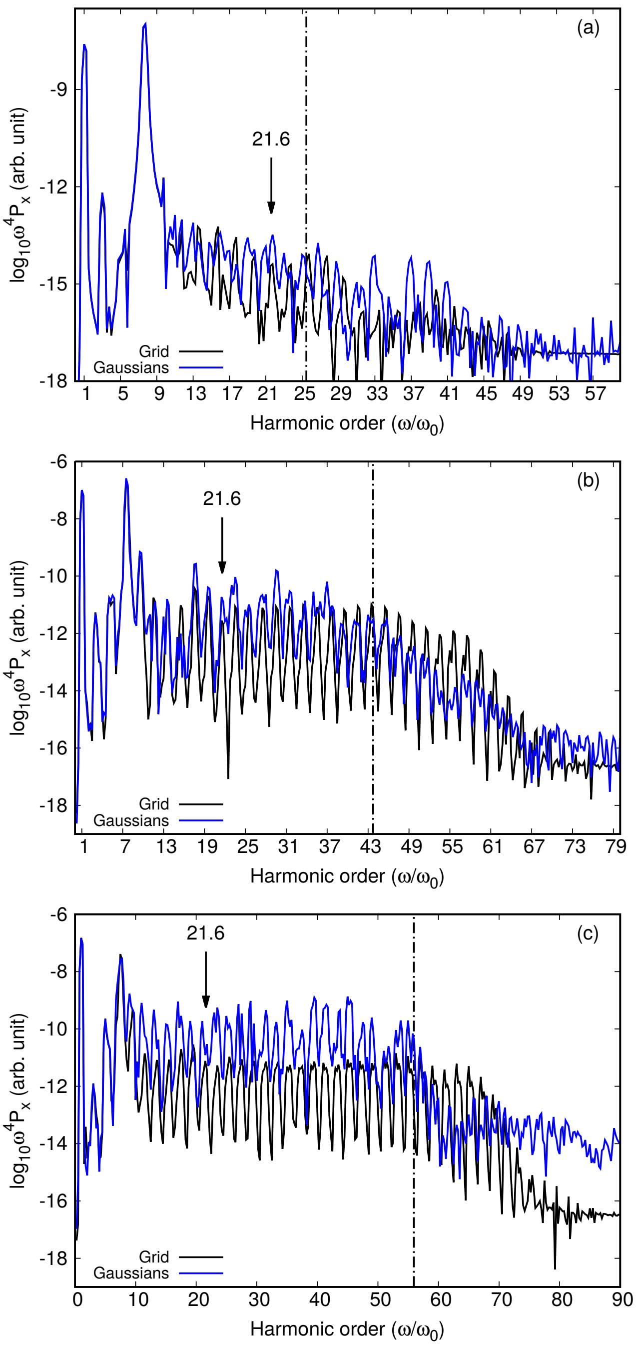

Figure 5.11: HHG spectra in the dipole form at the equilibrium internuclear distance $R = 2.0$ au with laser intensities: (a) $I = 5 \times 10^{13}$ W/cm^2, (b) $I = 2 \times 10^{14}$ W/cm^2, and (c) $I = 3 \times 10^{14}$ W/cm^2. For each HHG spectrum, the dot-dashed line gives the cutoff energy $E_{\text{cutoff}} = I_{\text{p}} + 3.17U_{\text{p}}$ given by the rescattering model [Corkum 93, Lewenstein 94] which is (a) $E_{\text{cutoff}} = 25.4\omega_0$, (b) $E_{\text{cutoff}} = 43.7\omega_0$, and (c) $E_{\text{cutoff}} = 55.9\omega_0$. The arrow points to the expected position of the two-center interference minimum extracted from the recombination dipole.

Raman lines was investigated. We showed that the grid and B-spline representations of the time-dependent wave function give the same results for both HHG and ATI. On the contrary, the performance of the Gaussian basis is more mixed and depends on the intensity of the laser. It is possible to optimize Gaussian functions to describe

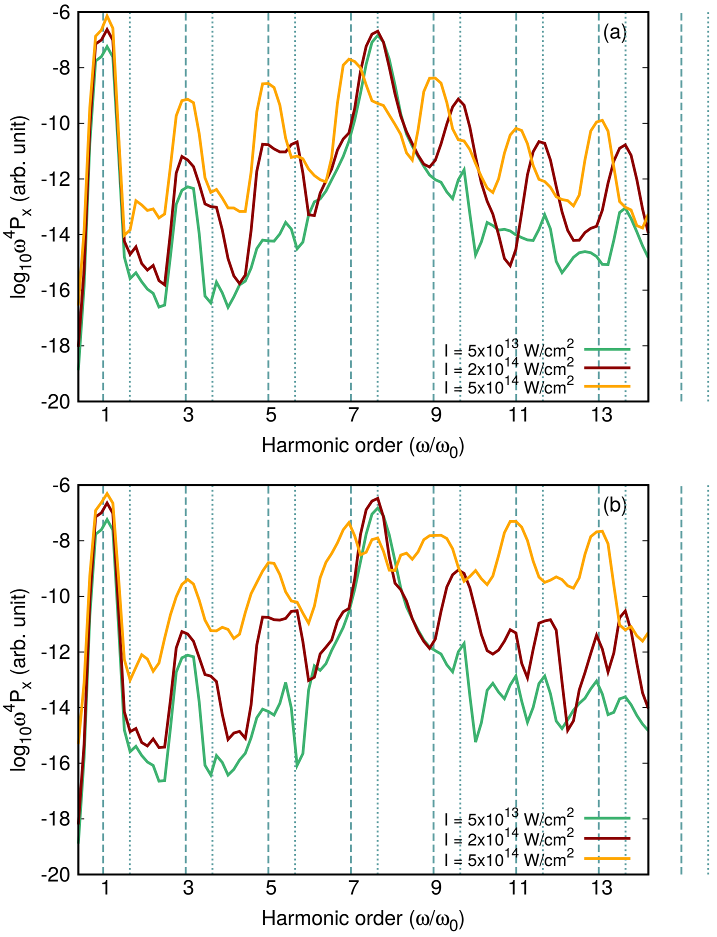

Figure 5.12: HHG spectra in the dipole form at the equilibrium internuclear distance of $R = 2.0$ au up to the 13th harmonic with laser intensities : $I = 5 \times 10^{13}$ W/cm^2, $I = 2 \times 10^{14}$ W/cm^2, and $I = 5 \times 10^{14}$ W/cm^2 for (a) grid and (b) Gaussian basis sets. For each HHG spectrum, the dashed line indicates the position of the harmonics and the dotted line indicates the hyper-Raman lines at position $\tilde{\omega} \pm 2k\omega_0$ [Gauthey 95] where k is an integer and $\tilde{\omega} = 7.65\omega_0$ is the resonance of the first excited state.

the low-energy part of the continuum. However, this optimization is limited by the issue of linear dependencies among Gaussian functions. This implies that for HHG the Gaussian basis can perform well up to the laser intensity $I = 5 \times 10^{14}$ W/cm^2 for 1D and up to $I = 2 \times 10^{14}$ W/cm^2 for 3D. For higher intensities we have found that only low-energy harmonics are still correct. Moreover, for 3D calculations, obtaining a good HHG spectrum with optimized Gaussian functions seems to be more difficult than in 1D calculations. Despite their limitations, Gaussian basis sets can reproduce intricate features of the HHG spectrum at low energy. Instead, in the case of ATI, Gaussian basis sets make impossible the description of a correct spectrum.

As a conclusion, from our investigation, we noticed that the grid and B-spline basis sets have very similar behavior and computational cost. These basis sets are very accurate to describe the continuum and phenomena such as HHG and ATI.

Gaussian basis sets are less efficient to describe the continuum. The effect on ATI and HHG spectra is however different: on one hand, ATI spectrum is not reproduced by Gaussian basis functions, on the other hand the most important features and fine structures (minimum/resonances) at low energy of the HHG spectrum are correctly described. A clear advantage of Gaussian functions with respect the other basis sets is their computational cost which continues to make them interesting for many-electron systems.

CHAPTER 6

Conclusion

In the present manuscript, attention has been focused on the computation of single and multiphoton processes on atoms and molecules. Due to the complex nature of this subject, different physical approximations, together with an ensemble of diverse numerical methods, have been developed, implemented, and used in order to obtain new insights on such matter-radiation processes.

Concretely, within the framework proposed by linear-response range-separated density-functional theory, we have explored photoexcitation and photoionization in one- and two-electron atoms. Thanks to the technique of B-splines, it was possible to correctly describe the continuum states of the investigated atomic systems. Therefore, the effects of the range-separation parameter on continuum states could be studied. At this point, we are now able to carry on our investigations on atoms with more than two electrons. This work opens the possibility of simulating core-electron transitions from inner shells to excited or continuum states. In addition, range-separation effects may be examined on multiphoton above-threshold ionization in N-electron atoms. A starting point will be, for example, the study of two-photon transitions.

Once again, B-splines have been shown to be a powerful numerical tool. However, when complex systems, such as molecules, have to be investigated, B-splines methods become very expensive from a computational point of view. For this reason, we have explored the possibility of using Gaussian-type orbitals (GTO) specially designed to describe the continuum. Multiphoton ionization processes, such as ATI and HHG, have been investigated on the one-dimensional molecular hydrogen ion H_2^+ using B-splines, GTO, and grid methods in order to compare their numerical accuracy. ATI spectra cannot be computed with the proposed GTO basis set. Linear dependencies limits our aspirations and the *incompleteness* of the GTO basis is an expensive price to pay when using such functions. Nevertheless, we observed that HHG spectra, obtained with moderate laser intensities, can be reproduced with the GTO basis. This opens the possibility of studying complex molecules within the TD-CIS framework used here. In the future, more systematic studies with ghost-atom basis functions shall be carried out in order to obtain a better measurement of their numerical performance and their effects on multiphoton ionization processes.

APPENDIX A

The Wigner 3-j Symbol

The Wigner 3-j symbol, also known as Clebsch-Gordon coefficient, is an algebraic function of six arguments that is defined as follows:

$$\begin{aligned} \begin{pmatrix} j_1 & j_2 & j_3 \\ m_1 & m_2 & m_3 \end{pmatrix} &= \delta_{m_1+m_2+m_3,0}(-1)^{j_1+j_2-m_3} \\ &\times \left[\frac{(j_1+j_2-j_3)!(j_1-j_2+j_3)!(-j_1+j_2+j_3)!}{(j_1+j_2+j_3+1)!}\right]^{1/2} \\ &\times \left[\frac{(j_1-m_1)!(j_1+m_1)!(j_2-m_2)!(j_2+m_2)!(j_3-m_3)!(j_3+m_3)!}{(j_1+j_2+j_3+1)!}\right]^{1/2} \\ &\times \sum_t \frac{(-1)^t}{t!(j_1+j_2+j_3-t)!(j_1-m_1-t)!(j_2+m_2-t)!(j_3-j_2+m_1+t)!(j_2-j_1-m_2+t)!} \end{aligned} \tag{A.1}$$

with $t \in [\max(0, j_2 - j_3 - m_1, j_1 - j_3 + m_2), \min(j_1 + j_2 - j_3, j_1 - m_1, j_2 + m_2)]$.

Eq. (A.1) is zero unless the following conditions (also known as selection rules) are satisfied:

(1) $m_1 \in \{-|j_1|, ..., |j_1|\}$, $m_2 \in \{-|j_2|, ..., |j_2|\}$ and $m_3 \in \{-|j_3|, ..., |j_3|\}$.

(2) $m_1 + m_2 + m_3 = 0$.

(3) $|j_1 - j_3| \leq j_2 \leq |j_1 + j_3|$.

(4) For the special case $m_1 = m_2 = m_3 = 0$, the sum $j_1 + j_2 + j_3 = 2s$ must be an even integer number.

Symmetry properties: the Wigner 3-j symbol satisfies the following symmetry permutations,

$$\begin{pmatrix} j_2 & j_1 & j_3 \\ m_2 & m_1 & m_3 \end{pmatrix} = \begin{pmatrix} j_1 & j_3 & j_2 \\ m_1 & m_3 & m_2 \end{pmatrix} = (-1)^{j_1+j_2+j_3} \begin{pmatrix} j_1 & j_2 & j_3 \\ m_1 & m_2 & m_3 \end{pmatrix}, \tag{A.2}$$

as well as this, it can be also seen that

$$\begin{pmatrix} j_1 & j_2 & j_3 \\ -m_1 & -m_2 & -m_3 \end{pmatrix} = (-1)^{j_1+j_2+j_3} \begin{pmatrix} j_1 & j_2 & j_3 \\ m_1 & m_2 & m_3 \end{pmatrix}. \tag{A.3}$$

Orthogonality and sum rules:

$$\sum_{j_3}\sum_{m_3}(2j_3+1)\begin{pmatrix} j_1 & j_2 & j_3 \\ m_1 & m_2 & m_3 \end{pmatrix}\begin{pmatrix} j_1 & j_2 & j_3 \\ m_1' & m_2' & m_3 \end{pmatrix} = \delta_{m_1,m_1'}\,\delta_{m_2,m_2'}. \tag{A.4}$$

$$\sum_{m_1}\sum_{m_2}(2j_3+1)\begin{pmatrix} j_1 & j_2 & j_3 \\ m_1 & m_2 & m_3 \end{pmatrix}\begin{pmatrix} j_1 & j_2 & j_3' \\ m_1 & m_2 & m_3' \end{pmatrix} = \delta_{j_3,j_3'}\,\delta_{m_3,m_3'}. \tag{A.5}$$

$$\sum_{m}(-1)^{j-m}\begin{pmatrix} j & j & j_3 \\ m & -m & 0 \end{pmatrix} = \sqrt{(2j+1)}\,\delta_{j_3,0} \tag{A.6}$$

Special values:

$$\begin{pmatrix} j_1 & j_2 & j_3 \\ 0 & 0 & 0 \end{pmatrix} = (-1)^s\left[\frac{(2s-2j_1)!(2s-2j_2)!(2s-2j_3)!}{(2s+1)!}\right]^{1/2} \times\frac{s!}{(s-j_1)!(s-j_2)!(s-j_3)!}, \tag{A.7}$$

where $2s = j_1 + j_2 + j_3$ must be an even integer, otherwise Eq. (A.7) is zero.

APPENDIX B

Spherical harmonics

Throughout the present manuscript we have made use of a different number of relations involving spherical harmonics. In this appendix, definitions and useful formula are collected. Proofs of them can be found in standard mathematical textbooks.

B.1 Legendre polynomials $P_l(x)$

The Legendre polynomials of degree l are defined by Rodrigues' formula:

$$P_l(x) = \frac{1}{2^l l!} \frac{\mathrm{d}^l (x^2-1)^l}{\mathrm{d}x^l}, \tag{B.1}$$

where $x \in [-1,1]$. Additionally, one has $P_l(-x) = (-1)^l P_l(x)$.

The Legendre polynomials satisfy the orthogonality relation

$$\int_{-1}^{1} P_k(x) P_l(x) \mathrm{d}x = \frac{2}{2k+1}\, \delta_{k,l}. \tag{B.2}$$

Moreover, it can be shown that a product of two polynomials can be expanded in a series in terms of the Wigner 3-j symbol such as

$$P_k(x) P_l(x) = \sum_{j=|k-l|}^{|k+l|} (2j+1) \begin{pmatrix} k & l & j \\ 0 & 0 & 0 \end{pmatrix}^2 P_j(x). \tag{B.3}$$

The integral of a product of three Legendre polynomials can be written as

$$\begin{aligned} \int_{-1}^{1} P_k(x) P_l(x) P_j(x) \mathrm{d}x &= \sum_{q=|k-l|}^{|k+l|} (2q+1) \begin{pmatrix} k & l & q \\ 0 & 0 & 0 \end{pmatrix}^2 \int_{-1}^{1} P_q(x) P_j(x) \mathrm{d}x \\ &= \sum_{q=|k-l|}^{|k+l|} (2q+1) \begin{pmatrix} k & l & q \\ 0 & 0 & 0 \end{pmatrix}^2 \frac{2}{(2q+1)}\, \delta_{q,j} \\ &= 2 \begin{pmatrix} k & l & j \\ 0 & 0 & 0 \end{pmatrix}^2 . \end{aligned} \tag{B.4}$$

Finally, it is interesting to see that any function $f(x)$ with $x \in [-1,1]$ can be expanded in terms of the Legendre polynomials such as

$$f(x) = \sum_{l=0}^{+\infty} f_l \; P_l(x), \tag{B.5}$$

where $f_l = [(2l+1)/2] \; \int_{-1}^{1} f(x)P_l(x)\mathrm{d}x$.

In particular, the Legendre polynomials are associated with the following generating function

$$\frac{1}{(1+t^2-2xt)^{1/2}} = \sum_{l=0}^{+\infty} t^l \; P_l(x), \tag{B.6}$$

for $|t| \leq 1$. Thus, it can be demonstrated that the inverse of the distance between two points can be expressed in terms of Legendre polynomials in spherical polar coordinates as

$$\begin{aligned} \frac{1}{|\mathbf{r}_1 - \mathbf{r}_2|} &= \frac{1}{(|\mathbf{r}_1|^2 + |\mathbf{r}_2|^2 - 2|\mathbf{r}_1||\mathbf{r}_2|\cos\gamma}\Big)^{1/2} \\ &= \frac{1}{r_> \left(1 + \left(\frac{r_<}{r_>}\right)^2 - 2\left(\frac{r_<}{r_>}\right)\cos\gamma\right)^{1/2}} && \text{(B.7)} \\ &= \sum_{l=0}^{+\infty} \left[\frac{r_<^l}{r_>^{l+1}}\right] P_l(\cos\gamma), && \text{(B.8)} \end{aligned}$$

where γ is the angle between $\mathbf{r}_1$ and $\mathbf{r}_2$, $r_< = \min(r_1, r_2)$ and $r_> = \max(r_1, r_2)$.

B.2 Associated Legendre polynomials $P_l^m(x)$

For a positive integer m, the unnormalized associated Legendre polynomials $P_l^m(x)$ are defined as

$$P_l^m(x) = (1-x^2)^{m/2} \frac{\mathrm{d}^m}{\mathrm{d}x^m} P_l(x), \tag{B.9}$$

where $P_l(x)$ are the Legendre polynomials. For negative integers $(m < 0)$ one has

$$P_l^{-m}(x) = (-1)^m \frac{(l-m)!}{(l+m)!} P_l^m(x), \tag{B.10}$$

and the orthogonality relation is defined as

$$\int_{-1}^{1} P_l^m(x) P_k^m(x) \mathrm{d}x = \frac{2}{(2l+1)} \frac{(l+m)!}{(l-m)!} \, \delta_{l,k}. \tag{B.11}$$

As a consequence, one can define the normalized associated Legendre polynomial functions as

$$\Theta_l^m(x) = \sqrt{\frac{(2l+1)}{2}\frac{(l-m)!}{(l+1)!}}\; P_l^m(x). \tag{B.12}$$

Finally, two important recurrence relations, involving the computation of the dipole transition matrix elements, are presented here for $x = \cos\theta$:

$$\begin{aligned} \cos\theta\;\Theta_l^m &= a_{l+1,m}\;\Theta_{l+1}^m + a_{l-1,m}\;\Theta_{l-1}^m, & \text{(B.13)}\\ \sin\theta\frac{\mathrm{d}}{\mathrm{d}\theta}\;\Theta_l^m &= l\times a_{l+1,m}\;\Theta_{l+1}^m + (l+1)\times a_{l-1,m}\;\Theta_{l-1}^m, & \text{(B.14)} \end{aligned}$$

where the relation coefficients are given by

$$\begin{aligned} a_{l+1,m} &= \left[\frac{(l-m+1)(l+m+1)}{(2l+1)(2l+3)}\right]^{1/2}, & \text{(B.15)}\\ a_{l-1,m} &= \left[\frac{(l-m)(l+m)}{(2l+1)(2l-1)}\right]^{1/2}. & \text{(B.16)} \end{aligned}$$

B.3 Spherical harmonics $Y_l^m(\Omega)$

For $m \geq 0$, spherical harmonics $Y_l^m(\Omega) \equiv Y_l^m(\theta,\phi)$ are defined by

$$Y_l^m(\theta,\phi) = \Theta_l^m(\cos\theta)\frac{e^{im\phi}}{\sqrt{2\pi}}, \tag{B.17}$$

where $\Theta_l^m(\theta)$ are the normalized associated Legendre polynomials. For negative integers ($m < 0$) one finds the following relation

$$Y_l^m(\Omega) = (-1)^m \left(Y_l^{-m}(\Omega)\right)^*. \tag{B.18}$$

Spherical harmonics are orthonormal functions, so we have that

$$\int (Y_l^m(\Omega))^* Y_{l'}^{m'}(\Omega)\mathrm{d}\Omega = \int_0^{2\pi}\int_0^{\pi} (Y_l^m(\theta,\phi))^* Y_{l'}^{m'}(\theta,\phi)\mathrm{d}\phi\sin\theta\mathrm{d}\theta = \delta_{l,l'}\;\delta_{m,m'}. \tag{B.19}$$

In addition, we recall the sum rule

$$\sum_{m=-l}^{l} |Y_l^m(\theta,\phi)|^2 = \frac{2l+1}{4\pi}. \tag{B.20}$$

The recurrence relations involving spherical harmonics are deduced directly from the associated Legendre polynomials by multiplying Eq. (B.13) and Eq. (B.14) by $e^{im\phi}/\sqrt{2\pi}$,

$$\begin{aligned} \cos\theta\, Y_l^m &= a_{l+1,m}\, Y_{l+1}^m + a_{l-1,m}\, Y_{l-1}^m, && \text{(B.21)} \\ \sin\theta \frac{\mathrm{d}}{\mathrm{d}\theta} Y_l^m &= l \times a_{l+1,m}\, Y_{l+1}^m + (l+1) \times a_{l-1,m}\, Y_{l-1}^m, && \text{(B.22)} \end{aligned}$$

where the relation coefficients $a_{l+1,m}$ and $a_{l-1,m}$ are given by Eq. (B.15) and Eq. (B.16).

In the calculation of electronic structures, it is convenient to define the renormalized spherical harmonics,

$$C_q^k(\Omega) \equiv C_q^k(\theta,\phi) = \left(\frac{4\pi}{2k+1}\right)^{1/2} Y_k^q(\theta,\phi). \tag{B.23}$$

Note the index inversion in $C_q^k(\Omega)$ with respect to $Y_k^q(\Omega)$.

Afterwards, important angular integrals are given by a product of three spherical harmonics, which can be easily determined with the help of the Wigner 3-j symbols,

$$\begin{aligned} \langle l'm'|C_q^k|lm\rangle &= \left(\frac{4\pi}{2k+1}\right)^{1/2} \int (Y_{l'}^{m'}(\Omega))^* Y_k^q(\Omega) Y_l^m(\Omega) \mathrm{d}\Omega \\ & (-1)^{-m'} \sqrt{(2l'+1)(2l+1)} \begin{pmatrix} l' & k & l \\ 0 & 0 & 0 \end{pmatrix} \begin{pmatrix} l' & k & l \\ -m' & m'-m & m \end{pmatrix} \\ &= \delta_{q,m'-m}\, c^k(l'm',lm), && \text{(B.24)} \end{aligned}$$

where $c^k(l'm',lm)$ are the Gaunt coefficients and the delta function rises from the 3-j symbol selection rules. The Gaunt coefficients present some interesting properties coming also from the 3-j symbol relations. Here, we list some of the useful ones:

(1) $c^k(l'm',lm) = (-1)^{m-m'} c^k(lm,l'm')$.

(2) $c^0(lm,lm) = 1$.

(3) $\sum_m c^k(lm,lm) = (2l+1)\,\delta_{k,0}$.

(4) $\sum_m [c^k(lm,l'm')]^2 = (2l'+1) \begin{pmatrix} l & k & l' \\ 0 & 0 & 0 \end{pmatrix}^2$.

The spherical harmonic addition theorem is stated as

$$\begin{aligned} P_l(\cos\gamma) &= \frac{4\pi}{(2l+1)} \sum_{m=-l}^{l} (-1)^m Y_l^{-m}(\theta_1, \phi_1) Y_l^m(\theta_2, \phi_2) \\ &= \frac{4\pi}{(2l+1)} \sum_{m=-l}^{l} (Y_l^m(\theta_1, \phi_1))^* Y_l^m(\theta_2, \phi_2), \end{aligned} \tag{B.25}$$

where γ is the angle between the two vectors $\hat{\mathbf{r}}_1 = (\theta_1, \phi_1)$ and $\hat{\mathbf{r}}_2 = (\theta_2, \phi_2)$ such as

$$\cos\gamma = \cos\theta_1 \cos\theta_2 + \sin\theta_1 \sin\theta_2 \cos(\phi_1 - \phi_2) = \hat{\mathbf{r}}_1 \cdot \hat{\mathbf{r}}_2. \tag{B.26}$$

This theorem can be rewritten in terms of the renormalized spherical harmonics as follows

$$P_l(\cos\gamma) = \sum_{m=-l}^{l} (-1)^m C_{-m}^l(\Omega_1) C_m^l(\Omega_2). \tag{B.27}$$

Finally, we can show that the inverse of a distance between two points is given by

$$\frac{1}{|\mathbf{r}_1 - \mathbf{r}_2|} = \sum_{l=0}^{+\infty} \left[\frac{r_<^l}{r_>^{l+1}} \right] \sum_{m=-l}^{l} (-1)^m C_{-m}^l(\Omega_1) C_m^l(\Omega_2). \tag{B.28}$$

APPENDIX C

Gauss-Legendre Quadrature

This appendix has been written following the book *"Numerical Recipes 3rd Edition: The Art of Scientific Computing"* [Press 07].

Gaussian quadrature techniques are numerical integration methods based on the following approximation

$$\int_a^b W(x) f(x) \mathrm{d}x \approx \sum_{j=1}^{N} w_j f(x_j), \tag{C.1}$$

where $W(x)$ is a known function and $f(x)$ can be approximated with a polynomial, and the weights w_j and the quadrature positions x_j depend on the choice of $W(x)$.

In Gauss-Legendre quadrature, one has $W(x) = 1$. In addition, the weights are computed using the following expression

$$w_j = \frac{2}{(1 - x_j^2)[P'_N(x_j)]^2}, \tag{C.2}$$

where $P'_N(x_j)$ is the derivative of the Legendre polynomial at its zero x_j. Thus, the quadrature positions x_j, also known as abscissas, are the N zeros of the Legendre polynomial $P_N(x)$ defined in the interval $[-1, 1]$.

Assuming that $f(x)$ is a polynomial function of order $2N - 1$, Eq. (C.1) can be evaluated exactly as follows

$$\int_a^b W(x) f(x) \mathrm{d}x = \frac{b-a}{2} \sum_{j=1}^{N} w_j f\left(\frac{b+a}{2} - \frac{b-a}{2} x_j\right). \tag{C.3}$$

REFERENCES

[Agostini 79] P. Agostini, F. Fabre, G. Mainfray, G. Petite and N. K. Rahman. *Free-Free Transitions Following Six-Photon Ionization of Xenon Atoms*. Phys. Rev. Lett., vol. 42, pages 1127–1130, 1979.

[Al-Sharif 98] A. I. Al-Sharif, R. Resta and C. J. Umrigar. *Evidence of physical reality in the Kohn-Sham potential: The case of atomic Ne*. Phys. Rev. A, vol. 57, pages 2466–2469, 1998.

[Anderson 99] E. Anderson, Z. Bai, C. Bischof, S. Blackford, J. Demmel, J. Dongarra, J. Du Croz, A. Greenbaum, S. Hammarling, A. McKenney and D. Sorensen. LAPACK Users' Guide. Society for Industrial and Applied Mathematics, Philadelphia, third edition, 1999.

[Andrade 15] X. Andrade, D. Strubbe, U. De Giovannini, A. H. Larsen, M. J. T. Oliveira, J. Alberdi-Rodriguez, A. Varas, I. Theophilou, N. Helbig, M. J. Verstraete, L. Stella, F. Nogueira, A. Aspuru-Guzik, A. Castro, M. A. L. Marques and A. Rubio. *Real-space grids and the Octopus code as tools for the development of new simulation approaches for electronic systems*. Phys. Chem. Chem. Phys., vol. 17, page 31371, 2015.

[Ángyán 05] J. G. Ángyán, I. C. Gerber, A. Savin and J. Toulouse. *van der Waals forces in density functional theory: Perturbational long-range electron-interaction corrections*. Phys. Rev. A, vol. 72, page 012510, 2005.

[Ángyán 06] J. G. Ángyán, I. Gerber and M. Marsman. *Spherical harmonic expansion of short-range screened Coulomb interactions.* J-Phys. A: Phys. Math. Gen. , vol. 39, no. 27, pages 8613–8630, 2006.

[Argenti 09] L. Argenti and R. Colle. *On the B-splines effective completeness.* Comput. Phys. Commun., vol. 180, page 1442, 2009.

[Bachau 01] H. Bachau, E. Cormier, P. Decleva, J. E. Hansen and F. Martí-n. *Applications of B-splines in atomic and molecular physics.* Rep. Prog. Phys., vol. 64, no. 12, pages 1815–1943, 2001.

[Baer 10] R. Baer, E. Livshits and U. Salzner. *Tuned Range-Separated Hybrids in Density Functional Theory.* Annual Rev. Phys. Chem., vol. 61, no. 1, pages 85–109, 2010.

[Bandrauk 09] A. D. Bandrauk, S. Chelkowski, D. J. Diestler, J. Manz and K. J. Yuan. *Quantum simulation of high-order harmonic spectra of the hydrogen atom.* Phys. Rev. A: At., Mol., Opt. Phys., vol. 79, page 023403, 2009.

[Becke 88] A. D. Becke and R. M. Dickson. *Numerical solution of Poisson's equation in polyatomic molecules.* J. Chem. Phys., vol. 89, no. 5, pages 2993–2997, 1988.

[Bergues 12] B. Bergues, M. Kübel, N. Johnson, B. Fischer, N. Camus, K. Betsch, O. Herrwerth, A. Senftleben, A. Sayler and T. Rathje. *Attosecond tracing of correlated electron-emission in non-sequential double ionization.* Nat. Commun., vol. 3, page 813, 2012.

[Bethe 57] H. A. Bethe and E. E. Salpeter. Quantum mechanics of one- and two-electron atoms. Springer, Berlin, 1957.

[Boys 50] S. F. Boys. *Electronic Wave Functions. I. A General Method of Calculation for the Stationary States of Any Molecular System.* Proceedings of the Royal Society of London. Series A, vol. 200, no. 1063, pages 542–554, 1950.

[Burnett 92] K. Burnett, V. C. Reed, J. Cooper and P. L. Knight. *Calculation of the background emitted during high-harmonic generation.* Phys. Rev. A: At., Mol., Opt. Phys., vol. 45, page 3347, 1992.

[Caillat 15] J. Caillat. Dynamiques des processus élémentaires dans les atomes et molécules. HDR, Sorbonne Université, 2015.

[Casida 95] M. E. Casida. Recents Advances in Density Functional Theory Methods, Part I. World Scientific, Singapore, 1995.

[Casida 98] M. E. Casida, C. Jamorski, Kim C. Casida and D. R. Salahub. *Molecular excitation energies to high-lying bound states from time-dependent density-functional response theory: Characterization and correction of the time-dependent local density approximation ionization threshold.* J. Chem. Phys., vol. 108, no. 11, pages 4439–4449, 1998.

[Casida 00] M. E. Casida and D. R. Salahub. *Asymptotic correction approach to improving approximate exchange correlation potentials: Time-dependent density-functional theory calculations of molecular excitation spectra.* J. Chem. Phys., vol. 113, no. 20, pages 8918–8935, 2000.

[Chen 08] Y. J. Chen and J. Liu. *High-order harmonic generation from diatomic molecules with large internuclear distance: The effect of two-center interference.* Phys. Rev. A: At., Mol., Opt. Phys., vol. 77, page 013410, 2008.

[Chini 14] M. Chini, K. Zhao and Z. Chang. *The generation, characterization and applications of broadband isolated attosecond pulses.* Nat. Photonics, vol. 8, page 178, 2014.

[Chirila 06] C. C. Chirila and M. Lein. *Strong-field approximation for harmonic generation in diatomic molecules.* Phys. Rev. A: At., Mol., Opt. Phys., vol. 73, page 023410, 2006.

[Chu 05] S. Chu. *Recent development of self-interaction-free time-dependent density-functional theory for nonperturbative treatment of atomic and molecular multiphoton processes in intense laser fields.* J. Chem. Phys., vol. 123, page 062207, 2005.

[Chu 16] X. Chu and G. C. Groenenboom. *Contributions of inner-valence molecular orbitals and multiphoton resonances to high-order-harmonic generation of N2: A time-dependent density-functional-theory study.* Phys. Rev. A: At., Mol., Opt. Phys., vol. 93, page 013422, 2016.

[Coccia 16a] E. Coccia and E. Luppi. *Optimal-continuum and multicentered Gaussian basis sets for high-harmonic generation spectroscopy.* Theor. Chem. Acc., vol. 135, page 43, 2016.

[Coccia 16b] E. Coccia, B. Mussard, M. Labeye, J. Caillat, R. Taïeb, J. Toulouse and E. Luppi. *Gaussian continuum basis functions for calculating high-harmonic generation spectra.* Int. J. Quantum Chem., vol. 116, page 1120, 2016.

[Coccia 17] E. Coccia, R. Assaraf, E. Luppi and J. Toulouse. *Ab initio lifetime correction to scattering states for time-dependent electronic-structure calculations with incomplete basis sets.* J. Chem. Phys., vol. 147, page 014106, 2017.

[Cohen-Tannoudji 97] C. Cohen-Tannoudji, B. Diu and F. Laloë. Mécanique quantique II. Hermann, 1997.

[Corkum 93] P. B. Corkum. *Plasma perspective on strong field multiphoton ionization.* Phys. Rev. Lett., vol. 71, page 1994, 1993.

[Cormier 94] E. Cormier. *Étude théorique de l'interaction entre un système à 1 ou 2 électrons actifs et un champ laser intense.* PhD thesis, Université de Bordeaux, 1994.

[Cormier 97] E. Cormier and P. Lambropoulos. *Above-threshold ionization spectrum of hydrogen using B-spline functions.* J. Phys. B: At., Mol. Opt. Phys., vol. 30, page 77, 1997.

[Cowan 81] R. D. Cowan. The theory of atomic structure and spectra. Los Alamos Series in Basic and Applied Sciences. University of California Press, Ltd., Berkeley, 1981.

[Crank 47] J. Crank, P. Nicolson and D. R. Hartree. *A practical method for numerical evaluation of solutions of partial differential equations of the heat-conduction type*. Math. Proc. Cambridge Philos. Soc., vol. 43, page 50, 1947.

[Damon 63] E. K. Damon and R. G. Tomlinson. *Observation of Ionization of Gases by a Ruby Laser*. Appl. Opt., vol. 2, no. 5, pages 546–547, 1963.

[de Boor 78] C. de Boor. A practical guide to splines. Springer-Verlag, New York, 1978.

[De Giovannini 12] U. De Giovannini, D. Varsano, M. A. L. Marques, H. Appel, E. K. U. Gross and A. Rubio. *Ab initio angle- and energy-resolved photoelectron spectroscopy with time-dependent density-functional theory*. Phys. Rev. A: At., Mol., Opt. Phys., vol. 85, page 062515, 2012.

[Dick 12] R. Dick. Advanced quantum mechanics - materials and photons. Springer, New York, 2012.

[Dreuw 03] Andreas Dreuw, Jennifer L. Weisman and Martin Head-Gordon. *Long-range charge-transfer excited states in time-dependent density functional theory require non-local exchange*. J. Chem. Phys., vol. 119, no. 6, pages 2943–2946, 2003.

[Einstein 05] A. Einstein. *Über einen die Erzeugung und Verwandlung des Lichtes betreffenden heuristischen Gesichtspunkt*. Annalen der Physik, vol. 322, no. 6, pages 132–148, 1905.

[Fernando 15] R. G. Fernando, M. C. Balhoff and K. Lopata. *X-ray Absorption in Insulators with Non-Hermitian Real-Time Time-Dependent Density Functional Theory*. J. Chem. Theor. Comp., vol. 11, no. 2, pages 646–654, 2015. PMID: 26579600.

[Fetic 17] B. Fetic and D. B. Milosevic. *Numerical solution of the time-dependent Schrödinger equation for H2+ ion with application to high-harmonic generation and above-threshold ionization.* Phys. Rev. E: Stat. Phys., Plasmas, Fluids, Relat. Interdiscip. Top., vol. 95, page 053309, 2017.

[Filippi 96] C. Filippi, C. J. Umrigar and X. Gonze. *Separation of the exchange-correlation potential into exchange plus correlation: An optimized effective potential approach.* Phys. Rev. A, vol. 54, pages 4810–4814, 1996.

[Fischer 89] C. F. Fischer and M. Idrees. *Spline algorithms for continuum functions.* Comput. Phys., vol. 3, page 53, 1989.

[Fischer 90] C. F. Fischer and M. Idrees. *Spline methods for resonances in photoionisation cross sections.* J. Phys. B: At., Mol. Opt. Phys., vol. 23, page 679, 1990.

[Fischer 08] C. F. Fischer. B-splines in variational atomic structure calculations. Advances In Atomic, Molecular, and Optical Physics. Academic Press, 2008.

[Fischer 11] C. F. A. Fischer. *B-spline Hartree-Fock program.* Comput. Phys. Commun., vol. 182, page 1315, 2011.

[Friedrich 98] H. Friedrich. Theoretical atomic physics, 2nd ed. Springer-Verlag, Berlin, Ltd., 1998.

[Fromager 13] E. Fromager, S. Knecht and H. J. A. Jensen. *Multi-configuration time-dependent density-functional theory based on range separation.* J. Chem. Phys., vol. 138, no. 8, page 084101, 2013.

[Gao 17] C.-Z. Gao, P. M. Dinh, P.-G. Reinhard and E. Suraud. *Towards the analysis of attosecond dynamics in complex systems.* Phys. Chem. Chem. Phys., vol. 19, page 19784, 2017.

[Gauthey 95] F. I. Gauthey, C. H. Keitel, P. L. Knight and A. Maquet. *Role of initial coherence in the generation of harmonics and* *sidebands from a strongly driven two-level atom.* Phys. Rev. A: At., Mol., Opt. Phys., vol. 52, page 525, 1995.

[Gerber 05] I. C. Gerber and J. G. Ángyán. *Hybrid functional with separated range.* Chem. Phys. Lett. , vol. 415, no. 1, pages 100 – 105, 2005.

[Gill 97] P. M.W. Gill. *A new expansion of the Coulomb interaction.* Chem. Phys. Lett. , vol. 270, no. 1, pages 193 – 195, 1997.

[Goll 06] E. Goll, H.-J. Werner, H. Stoll, T. Leininger, P. Gori-Giorgi and A. Savin. *A short-range gradient-corrected spin density functional in combination with long-range coupled-cluster methods: Application to alkali-metal rare-gas dimers.* Chem. Phys., vol. 329, no. 1, pages 276 – 282, 2006.

[Görling 94] A. Görling and M. Levy. *Exact Kohn-Sham scheme based on perturbation theory.* Phys. Rev. A, vol. 50, pages 196–204, 1994.

[Görling 98a] A. Görling. *Exact exchange-correlation kernel for dynamic response properties and excitation energies in density-functional theory.* Phys. Rev. A, vol. 57, pages 3433–3436, 1998.

[Görling 99] A. Görling. *New KS Method for Molecules Based on an Exchange Charge Density Generating the Exact Local KS Exchange Potential.* Phys. Rev. Lett., vol. 83, pages 5459–5462, 1999.

[Gross 85] E. K. U. Gross and Walter Kohn. *Local density-functional theory of frequency-dependent linear response.* Phys. Rev. Lett., vol. 55, pages 2850–2852, 1985.

[Görling 98b] A. Görling. *Exact exchange kernel for time-dependent density-functional theory.* Int. J. Quant. Chem., vol. 69, no. 3, pages 265–277, 1998.

[Görling 95] A. Görling and M. Levy. *DFT ionization formulas and a DFT perturbation theory for exchange and correlation, through adiabatic connection.* Int. J. Quant. Chem., vol. 56, no. S29, pages 93–108, 1995.

[Haessler 10] S. Haessler, J. Caillat, W. Boutu, C. Giovanetti-Teixeira, T. Ruchon, T. Auguste, Z. Diveki, P. Breger, A. Maquet, B. Carré, R. Taïeb and P. Salières. *Attosecond imaging molecular electronic wavepackets.* Nat. Phys., vol. 6, page 200, 2010.

[Han 10] Y.-C. Han and L. B. Madsen. *Comparison between length and velocity gauges in quantum simulations high-order harmonic generation.* Phys. Rev. A: At., Mol., Opt. Phys., vol. 81, page 063430, 2010.

[Han 13] Y.-C. Han and L. B. Madsen. *Internuclear-distance dependence of the role of excited states in high-order-harmonic generation of H2+.* Phys. Rev. A: At., Mol., Opt. Phys., vol. 87, page 043404, 2013.

[Hartree 57] D. R. Hartree. The calculation of atomic structures. John Wiley and Sons, New York, 1957.

[Hedegard 13] E. D. Hedegard, F. Heiden, S. Knecht, E. Fromager and H. J. A. Jensen. *Assessment of charge-transfer excitations with time-dependent, range-separated density functional theory based on long-range MP2 and multiconfigurational self-consistent field wave functions.* J. Chem. Phys., vol. 139, no. 18, page 184308, 2013.

[Helgaker 00] T. Helgaker, P. Jorgensen and J. Olsen. Molecular electronic structure theory. John Wiley and Sons, LTD, Chichester, 2000.

[Itatani 04] J. Itatani, J. Levesque, D. Zeidler, H. Niikura, H. Pépin, J. C. Kieffer, P. B. Corkum and D. M. Villeneuve. *Tomographic imaging molecular orbitals.* Nature, vol. 432, page 867, 2004.

[Ivanov 99] S. Ivanov, S. Hirata and R. J. Bartlett. *Exact Exchange Treatment for Molecules in Finite-Basis-Set Kohn-Sham Theory.* Phys. Rev. Lett., vol. 83, pages 5455–5458, Dec 1999.

[Joachain 11] C. J. Joachain, N. J. Kylstra and R. M. Potvliege. Atoms in Intense Laser Fields. Cambridge University Press, 2011.

[Kaufmann 89] K. Kaufmann, W. Baumeister and M. Jungen. *Universal Gaussian basis sets for an optimum representation Rydberg and continuum wavefunctions.* J. Phys. B: At., Mol. Opt. Phys., vol. 22, page 2223, 1989.

[Klinkusch 09] S. Klinkusch, P. Saalfrank and T. Klamroth. *Laser-induced electron dynamics including photoionization: A heuristic model within time-dependent configuration interaction theory.* J. Chem. Phys., vol. 131, no. 11, page 114304, 2009.

[Koch 01] W. Koch and M. C. Holthausen. A chemist's guide to density functional theory, second edition. Wiley-VCH Verlag GmbH, 2001.

[Kono 84] A. Kono and S. Hattori. *Accurate oscillator strengths for neutral helium.* Phys. Rev. A, vol. 29, pages 2981–2988, 1984.

[Krause 92] J. L. Krause, K. J. Schafer and K. C. Kulander. *Calculation of photoemission from atoms subject to intense laser fields.* Phys. Rev. A: At., Mol., Opt. Phys., vol. 45, page 4998, 1992.

[Krausz 14] F. Krausz and M. I. Stockman. *Attosecond metrology: from electron capture to future signal processing.* Nat. Photonics, vol. 8, page 205, 2014.

[Labeye 18] M. Labeye, F. Zapata, E. Coccia, V. Véniard, J. Toulouse, J. Caillat, R. Taïeb and E. Luppi. *Optimal Basis Set for Electron Dynamics in Strong Laser Fields: The case of Molecular Ion H2+.* J. Chem. Theor. Comp., vol. 14, no. 11, pages 5846–5858, 2018.

[Lagmago Kamta 09] G. Lagmago Kamta and A. D. Bandrauk. *Orbital symmetry and interference effects in molecular high-order harmonic generation*. Phys. Rev. A: At., Mol., Opt. Phys., vol. 80, page 041403, 2009.

[Landau 77] L. D. Landau and E. M. Lifshitz. Quantum mechanics (non-relativistic theory). Course of theoretical physics. Elsevier, 1977.

[Lee 08] Y.-M. Lee, J.-S. Wu, T.-F. Jiang and Y.-S. Chen. *Parallel solver for the three-dimensional Cartesian-grid-based time-dependent Schrödinger equation and its applications in laser H2+ interaction studies*. Phys. Rev. A: At., Mol., Opt. Phys., vol. 77, page 013414, 2008.

[Lein 02] M. Lein, N. Hay, R. Velotta, J. P. Marangos and P. L. Knight. *Interference effects in high-order harmonic generation with molecules*. Phys. Rev. A: At., Mol., Opt. Phys., vol. 66, page 023805, 2002.

[Levine 84] Z. H. Levine and P. Soven. *Time-dependent local-density theory of dielectric effects in small molecules*. Phys. Rev. A, vol. 29, pages 625–635, 1984.

[Lewenstein 94] M. Lewenstein, P. Balcou, M. Y. Ivanov, A. L?Huillier and P. B. Corkum. *Theory of high-harmonic generation by low-frequency laser fields*. Phys. Rev. A: At., Mol., Opt. Phys., vol. 49, page 2117, 1994.

[Limpanuparb 11] T. Limpanuparb and P. M. W. Gill. *Resolutions of the Coulomb Operator: V. The Long-Range Ewald Operator*. J. Chem. Theor. Comp., vol. 7, no. 8, pages 2353–2357, 2011.

[Liu 16] X. Liu, X. Zhu, L. Li, Y. Li, Q. Zhang, P. Lan and P. Lu. *Selection rules of high-order-harmonic generation: Symmetries of molecules and laser fields*. Phys. Rev. A: At., Mol., Opt. Phys., vol. 94, page 033410, 2016.

[Livshits 07] E. Livshits and R. Baer. *A well-tempered density functional theory of electrons in molecules.* Phys. Chem. Chem. Phys., vol. 9, pages 2932–2941, 2007.

[Lopata 13] K. Lopata and N. Govind. *Near and Above Ionization Electronic Excitations with Non-Hermitian Real-Time Time-Dependent Density Functional Theory.* J. Chem. Theor. Comp., vol. 9, no. 11, pages 4939–4946, 2013.

[Luppi 12] E. Luppi and M. Head-Gordon. *Computation high-harmonic generation spectra H2 and N2 in intense laser pulses using quantum chemistry methods and time-dependent density functional theory.* Mol. Phys., vol. 110, page 909, 2012.

[Luppi 13] E. Luppi and M. Head-Gordon. *Role of Rydberg and continuum levels in computing high harmonic generation spectra the hydrogen atom using time-dependent configuration interaction.* J. Chem. Phys., vol. 139, page 164121, 2013.

[Lépine 14] F. Lépine, M. Y. Ivanov and M. J. J. Vrakking. *Attosecond molecular dynamics: fact or fiction?* Nat. Photonics, vol. 8, page 195, 2014.

[Macías 88] A. Macías, F. Martín, A. Riera and M. Yáañez. *A practical solution to the unknown normalization problem.* Int. J. Quant. Chem., vol. 33, no. 4, pages 279–300, 1988.

[Madsen 07] C. B. Madsen and L. B. Madsen. *Theoretical studies of high-order harmonic generation: Effects of symmetry, degeneracy, and orientation.* Phys. Rev. A: At., Mol., Opt. Phys., vol. 76, page 043419, 2007.

[Mandel 95] L. Mandel and E. Wolf. Optical coherence and quantum optics. Cambridge University Press, 1995.

[Marante 14] C. Marante, L. Argenti and F. Martín. *Hybrid Gaussian-B-spline basis for the electronic continuum: Photoionization of* *atomic hydrogen*. Phys. Rev. A: At., Mol., Opt. Phys., vol. 90, page 012506, 2014.

[Marante 17] C. Marante, M. Klinker, I. Corral, J. González-Vázquez, L. Argenti and F. Martín. *Hybrid-Basis Close-Coupling Interface to Quantum Chemistry Packages for the Treatment of Ionization Problems*. J. Chem. Theory Comput., vol. 13, page 499, 2017.

[Marshall 02] S. L. Marshall. *Calculation of coulombic lattice potentials: II. Spherical harmonic expansion of the Green function*. J. Phys.: Con. Matt., vol. 14, no. 12, pages 3175–3198, 2002.

[Martín 99] F. Martín. *Ionization and dissociation using B-splines: photoionization of the hydrogen molecule*. J. Phys. B: At., Mol. Opt. Phys., vol. 32, page 197, 1999.

[Millack 93] T. Millack and A. Maquet. *Hyper-Raman Lines Produced During High Harmonic Generation*. J. Mod. Opt., vol. 40, page 2161, 1993.

[Mosert 16] V. Mosert and D. Bauer. *Photoelectron spectra with Qprop and t-SURFF*. Comput. Phys. Comm., vol. 207, pages 452 – 463, 2016.

[Nepstad 10] R. Nepstad, T. Birkeland and M. Forre. *Numerical study of two-photon ionization of helium using an ab initio numerical framework*. Phys. Rev. A: At., Mol., Opt. Phys., vol. 81, page 063402, 2010.

[Nikolopoulos 03] L. Nikolopoulos. *A package for the ab-initio calculation of one- and two-photon cross sections of two-electron atoms, using a CI B-splines method*. Comput. Phys. Commun., vol. 150, page 140, 2003.

[Nisoli 17] M. Nisoli, P. Decleva, F. Calegari, A. Palacios and F. Martín. *Attosecond Electron Dynamics in Molecules*. Chem. Rev., vol. 117, page 10760, 2017.

[Ossiander 17] M. Ossiander, F. Siegrist, V. Shirvanyan, R. Pazourek, A. Sommer, T. Latka, A. Guggenmos, S. Nagele, J. Feist, J. Burgdörfer, R. Kienberger and M. Schultze. *Attosecond correlation dynamics.* Nat. Phys., vol. 13, page 280, 2017.

[Pabst 16] S. Pabst, A. Sytcheva, O. Geffert and R. Santra. *Stability of the time-dependent configuration-interaction-singles method in the attosecond and strong-field regimes: A study of basis sets and absorption methods.* Phys. Rev. A: At., Mol., Opt. Phys., vol. 94, page 033421, 2016.

[Palacios 15] A. Palacios, J. L. Sanz-Vicario and F. Martín. *Theoretical methods for attosecond electron and nuclear dynamics: applications to the H2 molecule.* J. Phys. B: At., Mol. Opt. Phys., vol. 48, page 242001, 2015.

[Paziani 06] S. Paziani, S. Moroni, P. Gori-Giorgi and G. B. Bachelet. *Local-spin-density functional for multideterminant density functional theory.* Phys. Rev. B, vol. 73, page 155111, 2006.

[Peach 06] M. J. G. Peach, T. Helgaker, P. SaÅek, T. W. Keal, O. B. Lutnaes, D. J. Tozer and N. C. Handy. *Assessment of a Coulomb-attenuated exchangeâcorrelation energy functional.* Phys. Chem. Chem. Phys., vol. 8, pages 558–562, 2006.

[Petersilka 96] M. Petersilka, U. J. Gossmann and E. K. U. Gross. *Excitation Energies from Time-Dependent Density-Functional Theory.* Phys. Rev. Lett., vol. 76, pages 1212–1215, 1996.

[Picón 11] A. Picón, A. Bahabad, H. C. Kapteyn, M. M. Murnane and A. Becker. *Two-center interferences in photoionization of a dissociating H2+ molecule.* Phys. Rev. A: At., Mol., Opt. Phys., vol. 83, page 013414, 2011.

[Plaja 13] L. Plaja, R. Torres and A. Zaïr. Attosecond physics. Springer Books, 2013.

[Pople 78] J. A. Pople and W. J. Hehre. *Computation of electron repulsion integrals involving contracted Gaussian basis functions*. J. Comput. Phys., vol. 27, no. 2, pages 161 – 168, 1978.

[Press 07] W. H. Press, S. A. Teukolsky, W. T. Vetterling and B. P. Flannery. Numerical recipes 3rd edition: The art of scientific computing. Cambridge University Press, New York, NY, USA, 3 edition, 2007.

[Qiu 99] Y. Qiu and C. F. Fischer. *Integration by Cell Algorithm for Slater Integrals in a Spline Basis*. J. Comput. Phys., vol. 156, no. 2, pages 257 – 271, 1999.

[Rau 96] A. R. P. Rau. *The negative ion of hydrogen*. J. Astrophys. Astr., vol. 17, page 113, 1996.

[Rebolini 13] E. Rebolini, A. Savin and J. Toulouse. *Electronic excitations from a linear-response range-separated hybrid scheme*. Mol. Phys. , vol. 111, no. 9-11, pages 1219–1234, 2013.

[Rebolini 16] E. Rebolini and J. Toulouse. *Range-separated time-dependent density-functional theory with a frequency-dependent second-order Bethe-Salpeter correlation kernel*. J. Chem. Phys., vol. 144, no. 9, page 094107, 2016.

[Risoud 17] F. Risoud, C. Léveque, M. Labeye, J. Caillat, P. Salieres, R. Taïeb, T. Shaaran and A. Maquet. *Laser-induced blurring of molecular structure information in high harmonic spectroscopy*. Sci. Rep., vol. 7, page 17302, 2017.

[Ruiz 06] C. Ruiz, L. Plaja, R. Taïeb, V. Véniard and A. Maquet. *Quantum and semiclassical simulations in intense laser H2+ interactions*. Phys. Rev. A: At., Mol., Opt. Phys., vol. 73, page 063411, 2006.

[Runge 84] Erich Runge and E. K. U. Gross. *Density-Functional Theory for Time-Dependent Systems*. Phys. Rev. Lett., vol. 52, pages 997–1000, 1984.

[Sack 64] R. A. Sack. *Generalization of Laplace's Expansion to Arbitrary Powers and Functions of the Distance between Two Points*. J. Math. Phys., vol. 5, no. 2, pages 245–251, 1964.

[Sadeghpour 00] H. R. Sadeghpour, J. L. Bohn, M. J. Cavagnero, B. D. Esry, I. I. Fabrikant, J. H. Macek and A. R. P. Rau. *Collisions near threshold in atomic and molecular physics*. J. Phys. B: At. Mol. Opt. Phys., vol. 33, no. 5, pages 93–140, 2000.

[Sapirstein 96] J Sapirstein and W R Johnson. *The use of basis splines in theoretical atomic physics*. J. Phys. B: At. Mol. Opt. Phys., vol. 29, no. 22, pages 5213–5225, 1996.

[Savin 96] A. Savin. *On Degeneracy, Near Degeneracy and Density Functional Theory*. En J. M. Seminario, editor, Recent Developments of Modern Density Functional Theory, pages 327–357. Elsevier, Amsterdam, 1996.

[Sawada 16] R. Sawada, T. Sato and K. L. Ishikawa. *Implementation of the multiconfiguration time-dependent Hatree-Fock method for general molecules on a multiresolution Cartesian grid*. Phys. Rev. A: At., Mol., Opt. Phys., vol. 93, page 023434, 2016.

[Schafer 91] K. Schafer. *The energy analysis of time-dependent numerical wave functions*. Comput. Phys. Commun., vol. 63, page 427, 1991.

[Schatz 03] G. C. Schatz and M. A. Ratner. Quantum Mechanics in Chemistry. Dover Punlications, 2003.

[Schipper 00] P. R. T. Schipper, O. V. Gritsenko, S. J. A. van Gisbergen and E. J. Baerends. *Molecular calculations of excitation energies and (hyper)polarizabilities with a statistical average of orbital model exchange-correlation potentials*. J. Chem. Phys., vol. 112, no. 3, pages 1344–1352, 2000.

[Schoenberg 46] I. J. Schoenberg. *Contribution to the problem of approximation of equidistant data by analytic functions.* Quart. Appl. Math., vol. 4, pages 45–99, 1946.

[Schoenberg 64] I. J. Schoenberg. *Spline functions and the problem of graduation.* Proc. Nat. Acad. Sci., vol. 52, pages 947–950, 1964.

[Schoenberg 73] I. J. Schoenberg. Cardinal Spline interpolation. Philadelphia: Society of Industrial and Applied Mathematics, 1973.

[Seaton 62] M. J. Seaton and G. Peach. *The Determination of Phases of Wave Functions.* Proc. Phys. Soc., London, vol. 79, page 1296, 1962.

[Shao 15] Y. Shao and et al. *Advances in molecular quantum chemistry contained in the Q-Chem 4 program package.* Mol. Phys. , vol. 113, no. 2, pages 184–215, 2015.

[Shore 73] B. W. Shore. *Solving the radial Schrödinger equation by using cubic-spline basis functions.* J. Chem. Phys., vol. 58, page 3855, 1973.

[Sissay 16] A. Sissay, P. Abanador, F. Mauger, M. Gaarde, K. J. Schafer and K. Lopata. *Angle-dependent strong-field molecular ionization rates with tuned range-separated time-dependent density functional theory.* J. Chem. Phys., vol. 145, no. 9, page 094105, 2016.

[Smirnova 09] O. Smirnova, Y. Mairesse, S. Patchkovskii, N. Dudovich, D. Villeneuve, P. Corkum and M. Y. Ivanov. *High harmonic interferometry of multi-electron dynamics in molecules.* Nature, vol. 460, page 972, 2009.

[Stein 09a] T. Stein, L. Kronik and R. Baer. *Prediction of charge-transfer excitations in coumarin-based dyes using a range-separated functional tuned from first principles.* J. Chem. Phys., vol. 131, no. 24, page 244119, 2009.

[Stein 09b] T. Stein, L. Kronik and R. Baer. *Reliable Prediction of Charge Transfer Excitations in Molecular Complexes Using Time-Dependent Density Functional Theory.* Journal of the American Chemical Society, vol. 131, no. 8, pages 2818–2820, 2009.

[Stener 95] M. Stener, P. Decleva and A. Lisini. *Density functional-time-dependent local density approximation calculations of autoionization resonances in noble gases.* J. Phys. B: At. Mol. Opt. Phys., vol. 28, no. 23, pages 4973–4999, 1995.

[Stener 97] M. Stener, G. De Alti, G. Fronzoni and P. Decleva. *TDLDA calculations of photoionization cross-section and asymmetry parameter profiles of alkaline-earth atoms.* Chemical Physics, vol. 222, no. 2, pages 197 – 213, 1997.

[Stener 00] M. Stener and P. Decleva. *Time-dependent density functional calculations of molecular photoionization cross sections: N2 and PH3.* J. Chem. Phys., vol. 112, no. 24, pages 10871–10879, 2000.

[Stener 01] M. Stener, P. Decleva and A. Görling. *The role of exchange and correlation in time-dependent density-functional theory for photoionization.* J. Chem. Phys., vol. 114, no. 18, pages 7816–7829, 2001.

[Stener 05] M. Stener, G. Fronzoni and P. Decleva. *Time-dependent density-functional theory for molecular photoionization with noniterative algorithm and multicenter B-spline basis set: CS2 and C6H6 case studies.* J. Chem. Phys., vol. 122, no. 23, page 234301, 2005.

[Stener 06] M. Stener, D. Toffoli, G. Fronzoni and P. Decleva. *Time dependent density functional study of the photoionization dynamics of SF6.* J. Chem. Phys., vol. 124, no. 11, page 114306, 2006.

[Stener 07] M. Stener, D. Toffoli, G. Fronzoni and P. Decleva. *Recent advances in molecular photoionization by density functional* *theory based approaches.* Theoretical Chemistry Accounts, vol. 117, no. 5, pages 943–956, 2007.

[Suárez 17] N. Suárez, A. Chacón, J. A. Pérez-Hernández, J. Biegert, M. Lewenstein and M. F. Ciappina. *High-order-harmonic generation in atomic and molecular systems.* Phys. Rev. A: At., Mol., Opt. Phys., vol. 95, page 033415, 2017.

[Szabo 96] A. Szabo and N. S. Ostlund. Modern quantum chemistry. Dover Publications, Mineola, New York, 1996.

[Talman 76] J. D. Talman and W. F. Shadwick. *Optimized effective atomic central potential.* Phys. Rev. A, vol. 14, pages 36–40, 1976.

[Tao 09] L. Tao, W. Vanroose, B. Reps, T. N. Rescigno and C. W. McCurdy. *Long-time solution of the time-dependent Schrödinger equation for an atom in an electromagnetic field using complex coordinate contours.* Phys. Rev. A: At., Mol., Opt. Phys., vol. 80, page 063419, 2009.

[Tawada 04] Y. Tawada, T. Tsuneda, S. Yanagisawa, T. Yanai and K. Hirao. *A long-range-corrected time-dependent density functional theory.* J. Chem. Phys., vol. 120, no. 18, pages 8425–8433, 2004.

[Telnov 07] D. A. Telnov and S.-I. Chu. *Ab initio study of the orientation effects in multiphoton ionization and high-order harmonic generation from the ground and excited electronic states of H2+.* Phys. Rev. A: At., Mol., Opt. Phys., vol. 76, page 043412, 2007.

[Toffoli 06] D. Toffoli, M. Stener and P. Decleva. *Photoabsorption and photoionization dynamics study of silicon tetrafluoride in the framework of time-dependent density-functional theory.* Phys. Rev. A, vol. 73, page 042704, 2006.

[Toulouse 04] J. Toulouse, F. Colonna and A. Savin. *Long-range–short-range separation of the electron-electron interaction in density-functional theory.* Phys. Rev. A, vol. 70, page 062505, 2004.

[Toulouse 05] J. Toulouse, F. Colonna and A. Savin. *Short-range exchange and correlation energy density functionals: Beyond the local-density approximation.* J. Chem. Phys., vol. 122, no. 1, page 014110, 2005.

[Toulouse 06a] J. Toulouse, P. Gori-Giorgi and A. Savin. *Scaling relations, virial theorem, and energy densities for long-range and short-range density functionals.* Int. J. Quant. Chem., vol. 106, no. 9, pages 2026–2034, 2006.

[Toulouse 06b] J. Toulouse and A. Savin. *Local density approximation for long-range or for short-range energy functionals?* J. Mol. Struc., vol. 762, no. 1, pages 147–150, 2006.

[Toulouse 13] J. Toulouse, E. Rebolini, T. Gould, J. F. Dobson, P. Seal and J. G. Ángyán. *Assessment of range-separated time-dependent density-functional theory for calculating C6 dispersion coefficients.* J. Chem. Phys., vol. 138, no. 19, page 194106, 2013.

[Tozer 98] D. J. Tozer and N. C. Handy. *Improving virtual Kohno-Sham orbitals and eigenvalues: Application to excitation energies and static polarizabilities.* J. Chem. Phys., vol. 109, no. 23, pages 10180–10189, 1998.

[Tsuneda 10] T. Tsuneda, J. W. Song, S. Suzuki and K. Hirao. *On Koopmansâ theorem in density functional theory.* J. Chem. Phys., vol. 133, no. 17, page 174101, 2010.

[Ulusoy 11] I. S. Ulusoy and M. Nest. *Correlated Electron Dynamics: How Aromaticity Can Be Controlled.* J. Am. Chem. Soc., vol. 133, page 20230, 2011.

[Umrigar 98] C.J. Umrigar, A. Savin and X. Gonze. *Are Unoccupied Kohn-Sham Eigenvalues Related to Excitation Energies?* En J. F.

Dobson, G. Vignale and M. P. Das, editores, Electronic Density Functional Theory, pages 167–176. Springer US, 1998.

[Unser 99] M. Unser. *Splines: A Perfect Fit for Signal/Image Processing.* IEEE SIGNAL PROCESSING MAGAZINE, vol. 16, pages 22–38, 1999.

[van Faassen 06] M. van Faassen and K. Burke. *The quantum defect: The true measure of time-dependent density-functional results for atoms.* J. Chem. Phys., vol. 124, no. 9, page 094102, 2006.

[van Faassen 09] M. van Faassen and K. Burke. *Time-dependent density functional theory of high excitations: to infinity, and beyond.* Phys. Chem. Chem. Phys., vol. 11, pages 4437–4450, 2009.

[van Leeuwen 94] R. van Leeuwen and E. J. Baerends. *Exchange-correlation potential with correct asymptotic behavior.* Phys. Rev. A, vol. 49, pages 2421–2431, 1994.

[Čertík 12] O. Čertík. *Physics in Screening Environments.* PhD thesis, University of Nevada, Reno, 2012.

[Venuti 96] M. Venuti, P. Decleva and L. Lisini. *Accurate multichannel continuum states by a general configuration interaction expansion in aB-spline basis: application to He photoionization.* J. Phys. B: At. Mol. Opt. Phys., vol. 29, no. 22, pages 5315–5342, 1996.

[Vozzi 05] C. Vozzi, F. Calegari, E. Benedetti, J.-P. Caumes, G. Sansone, S. Stagira, M. Nisoli, R. Torres, E. Heesel, N. Kajumba, J. P. Marangos, C. Altucci and R. Velotta. *Controlling Two-Center Interference in Molecular High Harmonic Generation.* Phys. Rev. Lett., vol. 95, page 153902, 2005.

[Wang 17] D. Wang, X. Zhu, X. Liu, L. Li, X. Zhang, P. Lan and P. Lu. *High harmonic generation from axial chiral molecules.* Opt. Express, vol. 25, page 23502, 2017.

[Wassaf 03] J. Wassaf, V. Véniard, R. Taïeb and A. Maquet. *Strong Field Atomic Ionization: Origin of High-Energy Structures in Photoelectron Spectra.* Phys. Rev. Lett., vol. 90, page 013003, 2003.

[Wasserman 03] A. Wasserman, N. T. Maitra and K. Burke. *Accurate Rydberg Excitations from the Local Density Approximation.* Phys. Rev. Lett., vol. 91, page 263001, 2003.

[Wasserman 05] A. Wasserman and K. Burke. *Rydberg Transition Frequencies from the Local Density Approximation.* Phys. Rev. Lett., vol. 95, page 163006, 2005.

[Watson 22] G. N. Watson. A treatise on the theory of bessel functions. Cambridge University Press, Cambridge, 1922.

[Werner 15] H.-J. Werner, P. J. Knowles, G. Knizia, F. R. Manby, M. Schütz, P. Celani, W. Györffy, D. Kats, T. Korona, R. Lindh, A. Mitrushenkov, G. Rauhut, K. R. Shamasundar, T. B. Adler, R. D. Amos, A. Bernhardsson, A. Berning, D. L. Cooper, M. J. O. Deegan, A. J. Dobbyn, F. Eckert, E. Goll, C. Hampel, A. Hesselmann, G. Hetzer, T. Hrenar, G. Jansen, C. Köppl, Y. Liu, A. W. Lloyd, R. A. Mata, A. J. May, S. J. McNicholas, W. Meyer, M. E. Mura, A. Nicklass, D. P. O'Neill, P. Palmieri, D. Peng, K. Pflüger, R. Pitzer, M. Reiher, T. Shiozaki, H. Stoll, A. J. Stone, R. Tarroni, T. Thorsteinsson and M. Wang. *MOLPRO, version 2015.1, a package of ab initio programs*, 2015. see http://www.molpro.net.

[White 16] A. White, C. J. Heide, P. Saalfrank, M. Head-Gordon and E. Luppi. *Computation of high-harmonic generation spectra of the hydrogen molecule using time-dependent configuration-interaction.* Mol. Phys., vol. 114, page 947, 2016.

[Wigner 48] E. P. Wigner. *On the Behavior of Cross Sections Near Thresholds.* Phys. Rev., vol. 73, pages 1002–1009, May 1948.

[Wörner 10] H. J. Wörner, J. B. Bertrand, P. Hockett, P. B. Corkum and D. M. Villeneuve. *Controlling the Interference of Multiple Molecular Orbitals in High-Harmonic Generation*. Phys. Rev. Lett., vol. 104, page 233904, 2010.

[Yanai 04] T. Yanai, D. P. Tew and N. C Handy. *A new hybrid exchange correlation functional using the Coulomb-attenuating method (CAM-B3LYP)*. Chem. Phys. Lett. , vol. 393, no. 1, pages 51 – 57, 2004.

[Yang 09] Z. Yang, M. van Faassen and K. Burke. *Must Kohn-Sham oscillator strengths be accurate at threshold?* J. Chem. Phys., vol. 131, no. 11, page 114308, 2009.

[Yip 14] F. L. Yip, C. W. McCurdy and T. N. Rescigno. *Hybrid Gaussian discrete-variable representation for one- and two-active-electron continuum calculations in molecules*. Phys. Rev. A: At., Mol., Opt. Phys., vol. 90, page 063421, 2014.

[Zangwill 80] A. Zangwill and P. Soven. *Density-functional approach to local-field effects in finite systems: Photoabsorption in the rare gases*. Phys. Rev. A, vol. 21, pages 1561–1572, 1980.

[Zapata 19] F. Zapata, E. Luppi and J. Toulouse. *Linear-response range-separated density-functional theory for atomic photoexcitation and photoionization spectra*. J. Chem. Phys., vol. 150, no. 23, page 234104, 2019.

[Zhou 09] Z. Zhou and S. Chu. *Time-dependent localized Hartree-Fock density-functional linear response approach for photoionization of atomic excited states*. Phys. Rev. A, vol. 79, page 053412, 2009.